Tailoring Magnetic and Electronic Phenomena in $Fe_{1-x}Sn_xBi_2Se_4$ and $FeSb_{2-x}Bi_xSe_4$ Ferromagnetic Semiconductors

by

Juan Lopez

A dissertation submitted in partial fulfillment
of the requirements for the degree of
Doctor of Philosophy
(Materials Science and Engineering)
in the University of Michigan
2019

Doctoral Committee:

Associate Professor Pierre Ferdinand Poudeu-Poudeu, Chair
Associate Professor Emmanouil Kioupakis
Professor Joanna M. Millunchick
Professor Ctirad Uher

Juan Lopez

jslopez@umich.edu

ORCID iD: 0000-0002-7352-3350

Dedication

To my Imilla, K'aspikunka, and Yasa Siki. Your sacrifice brought to me Michigan, your love helped me graduate.

To my Segunda Familia, Los Figueroas, that kept me fed and helped me during tough times; Victoria, Ismael, Rickley, Giovanni, and Ashley.

Lastly, to all my wonderful friends who I got to know and supported me throughout this journey.

Without you all, this may have never happened.

Acknowledgements

First and foremost, I would like to thank my advisor, Prof. Pierre Ferdinand Poudeu P., for his incredible perspective, depth of knowledge, insight, and guidance which has been indispensable in completing and navigating the journey that was my doctoral study. Prof. Poudeu has inspired and enabled me to research a novel area of study, with the utmost patience and support. Prof. Poudeu warmly accepted me into his lab early in the summer and has continued to foster a collaborative atmosphere that produces incredible work and better scientists. Through his approach to science and engineering, he has helped me conduct impactful and fulfilling research that offer important insight to the academic community.

I would also like to sincerely thank Prof. Joanna M. Millunchick, Prof. Emmanouil Kioupakis, and Prof. Ctirad Uher for their support, professional expertise, and collaborative mentorship in completing my studies as part of my doctoral committee. Another thank you to Prof. Kioupakis and his group, particularly, Dr. Logan Williams, for his help in understanding the underlying magnetic interactions in the ferromagnetic semiconducting compounds. Another special thanks to Prof. Uher and his group, Dr. Alex Page and Trevor Bailey for their outstanding collaboration on many of the projects we worked on. A special thanks to Trevor Bailey for going above and beyond as a collaborator and friend.

I would like to thank my friends, past and present, in the Poudeu group for their support and friendship, Dr. Honore Djieutedjeu, Dr. Pranati Sahoo, Dr. Yuanfeng Liu, Dr. Nicholas Moroz, Dr. Erica Chen, Dr. Alan Olvera, Ruiming Lu, Brandon Buchanan, Yiqao Huang,

Yixuan Chen, Joseph Casamento, Tyler Del Rose, Alex Escobar, Siri Yarlagadda, and Adam Gaboury.

To my friends in the Materials Science and Engineering Department at the University of Michigan for all their help; Timothy Chambers, Ying Qi, Keith McIntyre, Chris Christian, Kevin Worth, Patti Vogel, Shelley Fellers, and Todd Richardson. A very special thank you to Renee Hilgendorf for all her support and guidance during my entire doctoral journey. Thank you for all you do.

To Kim Elliott, Andria Rose, Shira Washington, and Tiffany Porties for help during my time at Michigan.

A very special thank you to my cohort of 2013. We started the doctorate journey together and their support and camaraderie have been greatly appreciated.

A warm thank you to Elizabeth Kwamboka Gichana for your friendship and support during the thesis writing process.

Lastly, I would like to thank my family; my mamá Maria "Imilla", my papá Miguel "K'aspikunka", and my brother Juanvi "Yasa Siki" for their love and support throughout my entire journey at the University of Michigan.

Table of Contents

List of Figures

List of Tables

Abstract

Spintronics is a growing field that can significantly impact the future of microelectronics. This is due to the added functionality, which promises to increase the speed and power efficiency of future devices. The core of this functionality arises from magnetism. Spintronic devices not only use the charge of an electron to modulate current, but it also uses the spin of electrons to help shuttle and gate currents within a device. In order for this technology to become commercialized, there remain a number of issues which must be addressed. Understanding the fundamental physics of tunneling currents and how to control them is a central theme within this field. Another practical issue which must be addressed is the material platform. A material will need to shuttle polarized carriers throughout a device, and in order to maintain the spin-polarized current throughout the device, a magnetic material is required. The versatility of semiconductors is also useful because there fine dependence of electrical resistivity and dopant concentrations are what allow us to create practical devices in the first place. A semiconductor is necessary if the next generation of spin polarized diodes and spin field effect transistors are going to become a reality. A magnetic semiconductor is necessary if we want to usher in a new era of microelectronics. A hiccup towards progress, however, is that most semiconductors are not magnetic. Most magnetic materials are either insulating or metallic, neither of which allows tunable control over resistivity. So, a new class of material is being developed and prototyped. The dilute magnetic semiconductor (DMS) is the result of a top down approach taken to creating a magnetic semiconductor. The idea being, a non-magnetic semiconductor is doped with magnetic elements to introduce a magnetic interaction such that the material becomes ferromagnetic. This approach

has been fruitful creating a number of candidate materials. One issue, however, is that this approach tends to create DMS's with interdependent magnetic ion and carrier concentrations. The magnetic dopant also acts as an electronic dopant. This creates a problem since we want to understand the full impact of both the magnetic ion and carrier concentration. When you increase magnetic ion concentration, the carrier concentration is also changed. This complicates things since the Curie Temperature (T_c) is dependent upon both of these material properties. Since changing one affects the other, elucidating the roles they each play becomes more difficult. If these dynamics are to be well understood, the codependence must be decoupled.

To tackle this issue, we developed a different type of magnetic semiconductor with the general formula MPn_2Se_4 (M = Mn, Fe ; Pn = Sb,Bi). This new magnetic semiconductor separates the magnetic ion centers and electronic doping sites spatially. This allows significantly more control over the magnetic ordering and carrier concentrations. As a result, we have decided to probe the effect of reducing the magnetic ion concentration while keeping the carrier concentration relatively constant in $Fe_{1-x}Sn_xBi_2Se_4$. We observe a drastic reduction in Curie Temperature, ΔT_C ~ 125 K as a result in increasing the average distance between Fe^{2+} in the crystal structure.

The second project is involves the creation of a solid solution between a p-type magnetic semiconductor and an n-type magnetic semiconductor to determine the origin of magnetism in $FeSb_{2-x}Bi_xSe_4$ and related phases. This experiment is expected to deepen our understanding of the role itinerant carriers play in magnetic ordering within this magnetic semiconductor. Single

crystal diffraction is used to probe the atomic distribution of the various elements within the

crystal. This will is correlated with SQUID measurements and Seebeck measurements to

determine the point of bipolar crossover. This has allowed us to resolve the different magnetic

contributions and the role carriers have in stabilizing and enhancing magnetic phases.

Overall, this thesis contributes new templated material systems, which are used to provide new

insight into the design of magnetic semiconducting system

Chapter 1

Introduction

1.1 Preface

A thorough discussion on the recent advances contributing to the understanding of magnetic ordering and its origins is presented. This includes topics of profound interest, specifically the electronic band structure of dilute magnetic semiconductors (DMS) and its contribution to mediating magnetism using carriers.
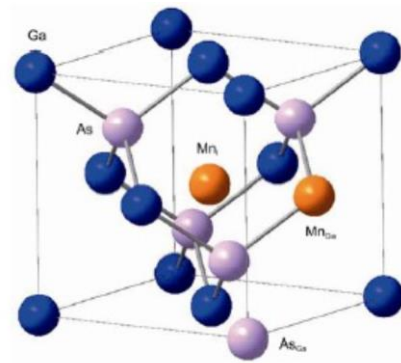
Figure 1.1 (Ga,Mn)As crystal structure with defects. Taken from *Zhao et al* [12]

New considerations for the science are also discussed and morphologies and fabrication techniques can have significant effect on the final state of the material. There have been great strides towards understanding magnetism in the carrier mediated ferromagnetism of (Ga,Mn)As. Dopant distributions and their effect on physical properties have finally achieved the spotlight, successful engineering of new metastable morphologies have been successfully created adding to the rich library of magnetic phases, and unambiguous data that finally reveals the true electronic structure of (Ga,Mn)As have finally been presented.

1.2 Motivation

Spintronic devices have the potential to decrease power consumption, reduce parasitic heat dissipation, enable more compact nanoelectronic architectures, and spur the realization of quantum computing. This is done by exploiting the charge and spin of electrons to yield novel functionalities. For such a phenomena to exist, a material that combines the logic capabilities of semiconductors with the storage capacities of magnetic compounds[1] with a high Curie transition temperature must be discovered. Past efforts in the field of spintronics have used a top-down approach and placed great emphasis on the dilution of semiconductors (GaAs) with magnetically active dopants (Mn). In 1996, (Ga,Mn)As, (pictured in Figure 1.) became the leading candidate for prototyping studies when ferromagnetic ordering was demonstrated with a Curie temperature of 110K by H. Ohno's group[2]. This concept of dilution, however, depends on the doping of active contributors to the band structure. Taking the (Ga,Mn)As system for example, the Mn atoms act as magnetic impurities and acceptors which introduce holes into the system by the substitution of Ga atoms in the crystal structure. As such, this approach would only allow for p-type materials making it difficult to use in real spin systems as one one need an n-type analogue. The culmination of all the diluted magnetic semiconductors have only been able to yield a Curie temperature of 190K[1]. This is still significantly lower than room temperature, 300K, which is needed for these systems to work. There have been some systems reported above room temperature, but they were anomalous and irreproducible[4]. While other systems have demonstrated room temperature ferromagnetism, the stability of their magnetic phases remain unexplained. The origin of ferromagnetism in magnetic semiconductors is also somewhat disputed in the theoretical realm. While the contribution of the effective magnetic atom concentration and the location of Fermi level have been shown to explain the Curie temperatures and that ferromagnetism is hole mediated in

the (Ga,Mn)As system[5], there remain a number of questions as to the effect of magnetic ordering, electronic transport, and chemical composition.

In order to address these issues, a new bottom-up approach must be developed in order to study the interplay between magnetism and semiconducting properties. Adapting old systems such as III-V and II-VI semiconductors and introducing magnetic atoms to spur a new class of magnetic semiconductors has indeed allowed great strides in the field, but dilution can only go so far before thermodynamics and crystal field physics complicate the problem. For this reason, a new class of material must be developed that can tackle the problem differently. One of the issues with the dilution approach is that the magnetic atoms are not inherent to the chemical identity of the semiconductor. For example, the most popular group IV semiconductor ,Si, is inherently non-magnetic. Upon introduction of magnetic atoms in the Si crystal, you begin fighting an uphill battle against thermodynamics in which magnetic agglomerates would rather form within the crystal. Other issues that arise is the interatomic distance between magnetic atoms. Magnetic materials exhibit their properties because magnetic atoms like to couple together to form magnetic ordering, in other words, they like to talk to each other. One major issue affecting the coupling is the interatomic distance between any two magnetic atoms in the structure. The longer the distance, the more difficult coupling becomes. If you look at the distribution of interatomic distances of diluted systems, it is random. Magnetic incorporation is random within the crystal, as a result the magnetic coupling is not very robust. The pinnacle of electronics is the semiconductor, the reason why is because we have decent control over properties (carrier type, conductivity) and can tailor the material to respond to different stimuli (i.e. light as in photovoltaics, stress in piezoelectrics). Introducing magnetic atoms in non-magnetic semiconductors, inhibits this control because many

times the magnetic atoms also act as acceptors in the structure. In most cases, III-V and II-VI diluted magnetic semiconductors exhibit p-type conduction and is difficult to double dope such that the material becomes n-type. So, for these reasons, the field requires a class of material which semiconducting, has magnetic atoms inherent to its chemical composition, and can separate these two types of atoms in the crystal to allow independent control over the magnetic and semiconducting properties that arise. Such a class of material would be modular, in the sense that one can effectively dope and substitute atoms in the crystal structure to achieve novel multifunctional materials. This new class of material would be a Modular Magnetic Semiconductor.

III-V Family of DMS.

The most prototypical system in this family is the (Ga,Mn)As system. Other systems include (In,Mn)P, (In,Mn)As, (Ga,Cr)As, (Ga,Cr)N and many other combinations of III-V elements with transition metal elements to introduce magnetism. The main synthetic method for this family of compounds is Molecular Beam Epitaxy, and much research is underway on further improving the technique in order achieve greater concentrations of magnetic atoms over the solubility limit. Much of the quantitative study in the field is on (Ga,Mn)As. One important thing to note is the site at which the magnetic atom is incorporated into the crystal structure. Ideally, the magnetic atom would replace a Ga ion in the cation site. For the most part, this is what happens, and then crystal field splitting takes enabling the lone electrons in the d-shell which is characteristic of magnetism. Issues do arise in this family though, when magnetic atoms substitute for a Ga ion, a hole is introduced into the sample. Occasionally, magnetic atoms substitute for the anion in the structure creating an antisite defect which is detrimental for the magnetism. What's worse, is that magnetic atoms can also find their way into the interstitial sites and coupling anti-ferromagnetically to

substituted Mn and cancel out the overall magnetic moment. The highest Curie temperature achieved for this family is 190K as shown by Ohno. This is done simply by developing a new growth protocol which reduces the growth temperature in order to inhibit the growth of secondary magnetic phases such as MnAs. History, however, shows that greater magnetic incorporation does not simply increase the Curie Temperature. In many cases, the maximum Curie temperature was achieved at an intermediate Mn concentration and then decreased with further substitution concentrations.

II-VI Family of DMS

This family of compounds has been more promising in the sense that they have yielded magnetic semiconductors with significantly higher curie temperatures. This is because magnetic atom incorporation at the cation site is easier, due to the fact that Zn has similar chemistry and behavior to Mn, Fe, Cr. In this family of compounds, however, the issue that arises now is creating both n-type and p-type magnetic semiconductors.

Considering magnetic dopant distributions

Within the realm of magnetic semiconductors, Mn-Mn (magnetic ion - magnetic ion) distance and their relative coupling strength can have a significant effect on the magneto-transport properties. In the early 2000's, this effect was essentially ignored which significantly inhibited the science. *Sandratskii et al*[6] provides a much needed study of the Mn distribution statistics within the host GaAs lattice. This study is critical in order to understand the effect of Mn-Mn distance on magnetic coupling and physical properties. Specifically, they are interested in the effect of Mn concentration on the Mn Distribution and electronic structure. This is studied by analyzing the effect of Mn distance on the density of states. The result of which is shown in Figure 2. This study is done using

Photoemission Spectroscopy and supported with Density Functional Theory (DFT) and Coherent

Potential Approximation (CPA) calculations. First off, the group develops a much more affective

way of analyzing spectral data by normalizing both the On and Off resonant photoemission spectra which cleans up the background noise. In doing so, they were able to reduce the amount of shift due to this background noise. This process revealed that the main Mn 3d state, which is close to the valence band maximum (the most important state in terms of carrier mediated magnetism), is located at approximately
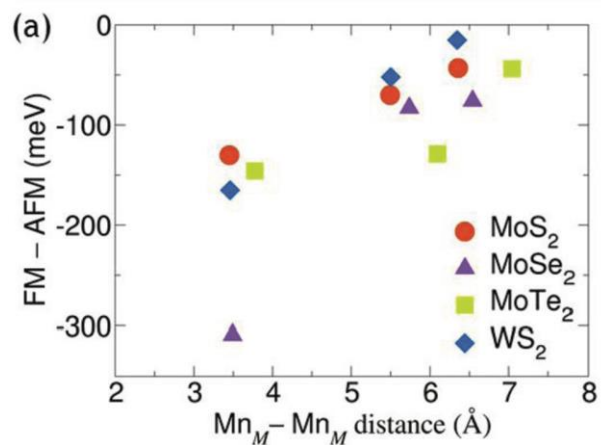
Figure 1.2. Energy change as a function of Mn-Mn distance between the ferromagnetic and antiferromagnetic phases. *Idrobo et al* [7]

3eV instead of the previously reported values of 4.5 eV. This finding was also backed up with a

CPA calculation which increase the likelihood of its validity. Applications of this study enlighten

the relation between the magnetic coupling strength and the level of Mn substitution which has

been shown to deviate significantly from the simple model. In support of their study, theoretical

studies by *Idrobo et al*[7] has shown that Mn-Mn separation within a lattice can significantly affect

the magnetic phases that arise, as shown in Figure 3.; a topic which is very critical to in the

engineering of spin polarization. This is done by simulating an ensemble of a two dimensional

chalcogenide doped with Mn atoms with varying distances. It was found that increasing the

distance destabilizes the super exchange interactions driving the system to lower Ferromagnetic

coupling.

Further establishing the presence of an impurity band induced ferromagnetism.

Dobrowolska et al[4] provided the first convincing evidence for the impurity band theory by mapping the Mn concentrations of substitutional and anti-site defects by using simultaneous channeling Rutherford backscattering and channeling particle-induced x-ray emission experiments in order to determine the effect of these defects on the magnetic states available for coupling. Her study sparked a heated discussion within the bipartisan DMS community as to the origin of ferromagnetism in these systems. More papers

Figure 1.3. Experimental band structure of (Ga,Mn)As achieved by SX-ARPES and concise diagram summarizing the finding. *Strocov et al* [11]

have been published since then, but *Strocov et al*[11] provides a systematic study on the band structure of (Ga,Mn)As proving the presence of an impurity band, sequentially providing a coherent model by which carrier polarization can be understood. In the past, experiments probing for the band structure of (Ga,Mn)As indicated a hybridized impurity state arising from Mn in the valence band of the full ensemble. Most of these experiments, however, failed to take into consideration the slight thermalization of Mn forming a paramagnetic phase, which then destabilizes the structure further forming MnAs clusters on the surface. These metallic impurities would naturally shift the impurity state toward the valence band maximum resulting in the merged valence band picture which so many scientists have argued for. Passivation of the (Ga,Mn)As layer by an amorphous As layer significantly improves the probing conditions and the soft x-ray angle

resolved photoemission spectroscopy (SX-ARPES) technique used further increases the probing depth allowing for a measurement which is more characteristic of the bulk states than just the surface states. Doing so allowed for the most unambiguous data proving the presence of an impurity band. As one can see in figure 4. the impurity band can be clearly seen above the heavy hole, light hole and split off fixtures. The diagram attached summarizes the findings as it highlights a split off Mn 3d derived impurity state in the band structure. One of the most complete works vying for the impurity band theory. The greatest significance of the study is that it unveils the fundamental physics which allow for the understanding of carrier mediated ferromagnetism in this system. This will allow for the engineering of similar systems for future spintronic application.

Advances in (Ga,Mn)As preparation.

Lee et al[8] advances the quality of deposition techniques of (Ga,Mn)As which allow for the precise reduction of interstitial, and anti-site defects. While their presence is physically important for the magnetic properties of (Ga,Mn)As, the level of control demonstrated is impressive. In (Ga,Mn)As, a long range magnetic order arises because of the substitutional defect. This is the end goal when forming the material, however, things are never that easy as interstitial defects of Mn in the host crystal can actually couple antiferromagnetically with the substitutional defect, essentially annihilating the net magnetic dipole and the ferromagnetic contribution all together. This is why Lee has achieved something of real significance, his group has managed to demonstrate a level of control over the Mn site distribution within the crystal. This level of control was achieved by growing the sample using Mn implantation and then sequentially annealing the sample using helium ion induced epitaxial crystallization annealing. The local structure is studied using high resolution transmission electron microscopy and double crystal x-ray diffraction. Interestingly, Lee and his group also report that they have managed to achieve room temperature ferromagnetism

by the presence of remnant magnetization which previously had never been seen before in the (Ga,Mn)As system. If that were the case this paper should actually be published in a journal with a much higher impact factor. I am a bit weary of this statement as it would be very technologically significant. In order to confirm such a property, ARPES measurements should be conducted and a matching of the moments arising from superconducting quantum interference device (SQUID) and x-ray magnetic circular dichroism (XMCD) compared to verify that the room temperature magnetism is not due to some metastable phase previously undiscovered due to the presence of strain in the lattice as a result of ion induced annealing. This is a significant advancement which allows for the possibility of reliable atomic engineering of the number of Mn sites within the host GaAs lattice; something that Dr. Dobrowolska has shown to be a significant next step on the road to MBE deposited room temperature magnetic semiconductors.

Advances in Magnetic Dopant Distributions

Another study by Dr. Dobrowolska[9] which exhibits advanced Mn distributions within host GaAs thin films allowing for both high impact research and enabling significant technological advancements. While the group has a working knowledge of the impact that Mn distributions can have on the magnetic properties, their aim is to demonstrate atomically engineered metastable Mn concentration gradients across the films. This is achieved using molecular beam epitaxy with an GaInAs buffer layer to initiate strain in the film, allowing for and reduce strain. The grading of the Mn concentration through the vertical length of the sample was achieved by stepping the temperature of the Mn source incrementally. The final structure resulted in a film which had eight layers of with progressively smaller concentrations of Mn throughout. Even though the group did not achieve quantitative control of the Mn concentration, this is a significant breakthrough in the engineering of magnetic properties for device applications. This paper has promising commercial

impact as it may be possible to increase the thermal stability and coercivity of DMS's. A new study of combating self-diffusion and self-annealing to produce new morphologies in solids has begun. While this paper is not as significant as Lee's paper[8], in terms of achieving the highest possible transition temperature, it is still technologically significant because it allows one to produce magnetization gradients within a structure so as to enable more efficient spin valves later on. There is also the scientific impact of creating a metastable concentration gradient which would normally be thermodynamically improbable.

Looking to the future: Achieving efficient interfacial exchange coupling in FM/DMS bilayers

Dr. Furdyna and Dr. Dobrowolska[10] have again created an insightful paper detailing the magnetic exchange interactions occurring between the hybrid Fe/(Ga,Mn)As bilayer through an extensive study utilizing SQUID, Polarized neutron reflectometry, X-ray absorption, X-ray magnetic circular dichroism, and x-ray specular reflectivity. Controlling interfacial coupling is of significant importance since it can lead to reliable control of spin polarized carriers. Initially, it was the discovery of spin dependent resistance of magnetic sandwich layers which spurred the field of spintronics. While they have gone on to be well understood, this knowledge has been slow to extend to more complex and more technologically viable nano-heterostructures. *Furdyna et al* manages to probe the interface and finds a layer of Mn is formed after annealing and seems the mediate the coupling between the strongly ferromagnetic Fe and weakly ferromagnetic (Ga,Mn)As layer. This is shown by the significant increase in the coercivity of (Ga,Mn)As as it seems to match that of the pure Fe layer. It is also shown, that the coupling is ferromagnetic rather than what was previously, antiferromagnetic coupling. While Dr. Furdyna's work seems a bit removed from the scope of enhancing material specific properties, we must look towards the future when such materials will be available and begin studying the exchange interactions across dissimilar films

and their resulting chemical stability. In order to prepare for a future of advanced heterostructures, we must be able to understand how the atoms drift when equilibrium is achieved and the resulting effect on the magnetic interactions. If spin valves and spin orbit/torque transistors are going to become the future, we must begin understanding these issues now.

Conclusion

Strocov and his group have finally managed to create the next breakthrough in establishing a coherent model by which carrier mediated magnetism can be understood in DMS systems that are scientifically important. They managed to perform ex-situ experiments which directly probe the electronic structure in a thermally and chemical passivated thin film with great probing depths. The presence of bound magnetic polaron and their contribution to the spin magnetization of the sample cannot be refuted. Now we can go use this information to systematically study various magnetic semiconductors and perform perturbation calculations in order to determine which systems might be technologically important. In this way, we can expedite the search for the most stable material for spintronics and confirm the results with experiments. This is by far the most important study to come out this year in magnetic semiconductors. Of second importance is the actual morphology and distribution of the magnetic dopants in the host material and their effect on the electronic structure. Idrobo and his group managed to establish the correlation between magnetic phase stability and coupling length. This is important because we can use this study to determine the optimal distance between magnetic centers in order to maximize the robustness of the magnetic phase. In this way, substitutional chemistry can be used to vary the lattice constant in such a way as to produce a solid solution which might contain the optimal distance for enhanced magnetic coupling. Sandratskii's efforts take a more direct approach by probing the differences in

electronic structure that arise using density functional theory and related approximations. Their findings are of importance because they vary the distance and observe the resulting effect on the density of states. This will tie in Strocov's work because they would essentially be writing the code which will be searching for other possible materials. By considering average distance between magnetic center, they may very find the material and optimize all in one experiment. Control over defects in (Ga,Mn)As is also of great importance considering the fact the Fermi level location within the impurity band seems to dictate the final magnetic transition temperature. Controlling the defects allows one to change the Fermi energy within the band structure, therefore once someone finds a way to incorporate more than 8% Mn into GaAs, atomic engineering may create a high throughput method for the fabrication of room temperature Tc (Ga,Mn)As. Lee and his group have managed to develop a new processing technique which allows for enhanced Mn distributions throughout the crystal by reducing the number of interstitial defects which both reduce the Fermi level and the carrier density. Advanced metastable morphologies have also been developed. Dr. Dobrowolska[9] managed to create a new technique allowing for the qualitative engineering of Mn concentration gradients across the thin film. This opens up a whole new field optimized nanoelectronic architectures which should lead to greater efficiencies and exotic properties which can be observed in magnetic heterostructure as shown by Dr. Furdyna and Dr. Dobrowolska[10]. 2014 was a very fruitful year for the study of (Ga,Mn)As, both physically (band structure and origin of magnetism) and structurally (new morphologies and atomm distributions). The highlight would have to be the work done by *Strocov et al* as they finally proved without a doubt that impurity band model is the mechanism through which long range magnetic order is achieved in (Ga,Mn)As.

1.3 References

[1]Editorial. More than just room temperature. *Nature Mater*. **2010**, *9*, 951.

[2] Ohno, H.; Shen, A.; Matsukura, F.; Oiwa, A.; Endo, A.; Katsumoto, S.; Iye, Y. (Ga,Mn)As: A new diluted magnetic semiconductor based on GaAs. *Appl. Phys. Lett.* **1996,** *69*, 363-365

[3] Hai, P.N.; Anh, L.D.; Tanaka, M. Electron effective mass in n-type electron-induced ferromagnetic semiconductor (In,Fe)As: Evidence of conduction band transport. *Appl. Phys. Lett.* **2012,** *101*, 252410

[4] Dobrowolska, M. Tivakornsasithron, K.; Liu, X.; Furdyna, J.K., Berciu, M.; Yu, K.M.; Walukiewicz. Controlling the Curie temperature in (Ga,Mn)As through the location of the Fermi level within the impurity band. *Nature Mater.* **2012**, *11*, 444-449

[5] Djieutedjeu. H.; Takas, N.J.; Makongo, J.P.A.; Rotaru, A.; Ranmohotti, K.; Anglin, C.; Spinu, L.; Wiley, J.B.; Poudeu, P.F.Structural-Distortion-Driven Cooperative Magnetic and Semiconductor-to-Insulator Transitions in Ferromagnetic FeSb$_2$Se$_4$. *Angew. Chem. Int. Ed.* **2010,** *49*, 9977-9981

[6] Ulfat, I.; Kanski, J.; Ilver, L.; Sadowski, J.; Karlsson, K.; Ernst, A.; Sandratskii, L. Effects of nonuniform Mn distribution in (Ga,Mn)As. Phys. Rev. B. **2014**, *89*, 045312

[7] Mishra, R.; Zhou, W.; Pennycook, S.J.; Pantelides, S. T.; Idrobo, J. C. Long-range ferromagnetic ordering in manganese-doped two-dimensional dichalcogenides. **2013**, *88*, 144409

[8] Chen, C.H.; Niu, H.; Yan, D.C.; Hsieh, H.H.; Huang, R.T.; Chi, C.C; Lee, C.P.; Local structure and magnetic properties of ferromagnetic GaMnAs made by helium ion induced epitaxial crystallization annealing. *Appl. Surf. Sci*. **2014**, *310*, 210-213

[9] Leiner, J.; Kirby, B.J.; Fitzsimmons, M.R.; Tivakornsasithorn, K.; Liu, X.; Furdyna, J.K.; Dobrowolska, M. Magnetic depth profile in GaMnAs layers with vertically graded Mn concentrations. *Jour. Mag. & Mag. Mater*. **2014**, *350*, 135-140

[10] Alsmadi, A.M.; Choi, Y.; Keavney, D.J.; Eid, K.F.; Kirby, B.J.; Liu, X.; Leiner, J.; Tivakornsasithorn, K.; Dobrowolska, M.; Furdyna, J.K. Interfacial exchange coupling in Fe/(Ga,Mn)As bilayers. *Phys. Rev. B.* **2014**, *89*, 224409

[11] Kobayashi, M.; Muneta, I.; Takeda, Y.; Harada, Y.; Fujimori, A.; Krempasky, J.; Schmitt, T.; Ohya, S.; Tanaka, M.; Oshima, M.; Strocov, V.N. Unveiling the impurity band induced ferromagnetism in the magnetic semiconductor (Ga,Mn)As. Phys. Rev. B. **2014**, *89*, 205204

[12] Wang, H.; Chen, l; Zhao, J. Enhancement of the Curie temperature of ferromagnetic semiconductor (Ga,Mn)As. Science China Physics,Mechanics & Astronomy, **2013**, *56(1)*, 99-110

Chapter 2

Experimental Techniques

2.1 Synthesis techniques

For all the materials in this thesis, only one synthetic technique was employed. Solid state synthesis was used and reacted at moderate temperatures.

2.1.1 Solid state synthesis

Single phase polycrystalline powders of $FeBi_2Se_4$, $Fe_{1-x}Sn_xBi_2Se_4$, $FeSb_{2-x}Bi_xSe_4$, and $Pb_6Bi_2Se_9$ were synthesized using solid state synthesis. High purity elements ($\geq99.9\%$) were weighed and mixed using an agate mortar and pestle and then sealed in evacuated quartz tubes (7mm ID x 9mm OD) down to pressures ~10-3 torr. The test tubes of unreacted material were then placed in tube furnaces and reacted using moderately low reaction profiles tailored to avoid explosive reactions with the selected reagents. The powders were reacted according to the following reaction profiles;

- $FeBi_2Se_4$:
  - Reaction
  - Heated to 573 K over 12hrs
  - Dwelled for 24hrs
  - Heated to 750 K over 12 hrs
  - Dwelled for 72 hrs
  - Cooled to RT over 24 hrs
  -
  - Annealing
  - Heated to 775K over 12 hrs
  - Dwelled for 120 hrs
  - Cooled to RT over 24 hrs
- $Fe_{1-x}Sn_xBi_2Se_4$:

- Reaction
- Heated to 573 K over 12hrs
- Dwelled for 24hrs

- Heated to 748 K over 12 hrs
- Dwelled for 72 hrs
- Cooled to RT over 12 hrs
-
- Annealing
- Heated to 913K over 12 hrs
- Dwelled for 120 hrs
- Cooled to RT over 24 hrs

- $FeSb_{2-x}Bi_xSe_4$:
  - Reaction
  - Heated to 573 K over 12hrs
  - Dwelled for 24hrs
  - Heated to 748 K over 12 hrs
  - Dwelled for 72 hrs
  - Cooled to RT over 12 hrs

- $Pb_6Bi_2Se_9$:
  - Heated to 773K over 12hrs
  - Dwelled for 120 hrs
  - Cooled to RT over 24hrs

Annealing was necessary for some materials in order to improve crystallinity. The resulting powders after reaction were dark grey polycrystalline powders that were stable at STP.

2.2 Characterisation techniques

Phase and structural identification, materials processing, electronic transport properties, and magnetic properties were all measured using the techniques listed in this section.

2.2.1 Powder X-ray diffraction (PXRD)

PXRD was used extensively in determining phase purity, crystal structure, and phase fractions. PXRD diffractograms were collected in atmosphere using graphite monochromated Cu-Kα (λ = 1.54056 Å) radiation on a Rigaku Miniflex 600 operating at 40 kV and 15 mA, a Rigaku Ultima with rotating arm anode operating at 40 kV and 100 mA, and a Rigaku SmartLab operating at 40kV and 44mA. All diffractometers were run in Bragg-Brentano reflection geometry. The

experimental patterns measured were then matched to theoretical patterns using single crystal structure data.

2.2.2 Single Crystal X-ray diffraction

Single crystals of targeted materials were collected from annealed batches, mounted onto thin glass wire mounts and examined by single crystal X-ray diffraction using a STOE IPDS-2T diffractometer using graphite-monochromated Mo Kα radiation ($\lambda = 0.71073$ Å) at 50 kV and 40 mA. The crystal structure was then solved using a full-matrix least-squares techniques using the SHELLX package (citation)

2.2.2.1 Structure refinement of FeBi$_2$Se$_4$

A needle-shaped single crystal of FeBi$_2$Se$_4$ with dimensions $0.05 \times 0.06 \times 0.15$ mm was used for X-ray data collection. Intensity data were recorded at 100, 300 and 400 K on a STOE Imaging Plate Diffraction System (IPDS-2T) equipped with a low temperature attachment (Cryostream-700 from Oxford Cryosystems). Intensity data were indexed in the monoclinic crystal system and the structure was solved by direct methods in the space group *C*2/*m* (#12) using the SHELTXL software package.[37] The structure solution revealed four crystallographically independent metal positions, M1 to M4, and four selenium positions Se1 to Se4 within the asymmetric unit cell. In the first refinement cycle, Bi atoms were assigned to the general positions M1(4*i*) and M2(4*i*) located in a square pyramidal and octahedral coordination, respectively, while Fe atoms were located in the octahedrally coordinated special positions M3(2*c*) and M4(2*a*). The refinement of this model using full-matrix least-squares techniques resulted in reasonable thermal parameters for all atoms except Fe(4), which displayed a smaller thermal parameter compared to those of the Bi atoms. This suggested Fe/Bi mixed occupancy at the Fe(4) position. The refinement of this model

resulted in more uniform thermal parameters for all atoms, and $R1$ dramatically dropped to 6%. However, the final composition showed excess positive charges. To search for a charge-balanced formula of the compound, Bi/Fe mixed occupancy at M1 and M2 positions were also considered. The refinement of this model resulted in an almost neutral composition with ~16% Fe, ~14% Fe and ~39 % Fe in M1, M2 and M4 sites, respectively, while the M3 position remained fully occupied by Fe. In the final refinement step, an electroneutrality restraint was included along with secondary extinction correction and anisotropic displacement parameters for all atoms. The occupancy factors at M1, M2 and M4 positions were refined to the final values of M1 = 85%Bi + 15%Fe, M2 = 85%Bi + 15%Fe, and M4 = 60%Bi + 40%Fe leading to a charge balanced formula of $FeBi_2Se_4$ assuming 2+, 3+, and 2− oxidation states for Fe, Bi and Se, respectively. A summary of crystallographic data for $FeBi_2Se_4$ at 100, 300 and 400 K are gathered in Table X. The atomic coordinates and isotropic displacement parameters of all atoms are given in Table X. Selected interatomic bond distances in $FeBi_2Se_4$ are compared in Table X. The software Diamond was utilized to create the graphic representation of the crystal structure with ellipsoid representations (98% probability level) for all atoms.[38] Changes in the lattice parameters of the $FeBi_2Se_4$ single crystal upon warming from 100 to 400 K are given in Table S1. Further details of the crystal structure investigation are given in CIF format as Supporting Information and can also be obtained from the Fachinformationszentrum Karlsruhe, 76344 Eggenstein- Leopoldshafen, Germany, (fax: +49 7247 808 666; e-mail: crysdata@fiz.karlsruhe.de) on quoting the depository numbers CSD_427627 for $FeBi_2Se_4$ at 100 K, CSD_427628 for $FeBi_2Se_4$ at 300 K and CSD_427629 for $FeBi_2Se_4$ at 400 K.

2.2.2.2 Structure refinement of $Fe_{1-x}Sn_xBi_2Se_4$

Single crystals of selected $Fe_{1-x}Sn_xBi_2Se_4$ ($0 < x < 0.5$) samples were obtained through annealing of the synthesized single phase polycrystalline powders at 913 K. The crystals were mounted on glass fibers using silicon paste and intensity data were collected at room temperature (300 K) on a STOE Imaging plate Diffraction System (IPDS-2T) using a graphite monochromatized MoKα radiation ($\lambda = 0.71073$ Å). Intensity data for all crystals were indexed in the monoclinic space group $C2/m$ (#12) and the structure, chemical composition as well as the distribution of metal atoms within the crystal lattice were determined through refinement using the atomic positions of $FeBi_2Se_4$ as the starting model in the SHELTXL software package. In the first refinement cycle, Bi atoms were located at the general positions M1(*4i*) and M2(*4i*) with octahedral and square pyramidal coordination, respectively, while the octahedrally coordinated special positions M3(*2c*) and M4(*2b*) were occupied by Fe atoms, regardless of the starting stoichiometry. The refinement of this model for all compositions generally yielded acceptable atomic displacement parameters for all metal atoms except the Fe atoms at the M4 site, which showed smaller thermal parameters compared to the Fe atom at the M3(*2c*) site. This suggests that the M4(2b) site is either occupied by a heavier elements or, at a minimum is mixed occupied by Fe atoms and a heavier element, such as Bi or Sn. Therefore, the remaining refinement steps focused on the optimization of the distribution of Fe, Bi and Sn at M1, M2 and M4 sites. Taking into account the preferential intermixing between Bi and Fe at the M1 and M2 sites, as well as the preferential occupancy of the M3(*2c*) site by an Fe atom observed in the structure of the parent compound, $FeBi_2Se_4$, we subsequently considered a structural model in which Bi and Fe are mixed at M1 and M2 sites, whereas Bi and Sn are mixed at the M4 site. While the refinement of this model yielded acceptable thermal parameters and agreement factors, the resulting chemical compositions showed a large excess of Bi atoms. Interestingly, the fraction of Sn atom within the M4 site at this stage of the refinement was generally within range of the nominal composition of the crystal. This observation greatly simplified the final refinement steps as it suggested that Sn atoms preferentially occupied the M4 sites. In the next refinement cycles, the fraction of Sn atoms within the M4 sites was fixed to the value obtained from the above-mentioned second refined model, and mixed occupancy between Bi and Fe was also considered for the remaining fraction of the M4 site, with to total occupancy fixed to unity. The refinement of this model, greatly optimized the distribution of Bi and Fe between the M1, M2 and M4 sites as reported in Table 2 and the final composition was

closer to the charge balanced nominal composition. Remarkably, attempts to optimize the refinement and achieve charge balance through incorporation of Sn at the M1 and M2 sites failed, which further confirmed the preferential occupancy of the M4 position by Sn atoms. Therefore, mixed occupancy of Sn, Bi and Fe was considered at the M4 site with the total occupancy factor fixed to unity. In addition, the sum of fraction of Bi atoms at M1, M2 and M4 sites was set to 2 per unit formula unit. The refinement of this model, including secondary extinction correction and anisotropic displacement parameters for all atoms, resulted in a charge balanced formula as well as the final distribution of Bi, Sn, and Fe at M1, M2 and M4 sites reported in Table 2. Summary of the crystallographic data are given in Table 1. The atomic coordinates, occupancy factors and isotropic displacement parameters of all atoms in the structures of selected $Fe_{1-x}Sn_xBi_2Se_4$ ($0 \leq x \leq 0.5$) samples are given in Table 2. Selected inter-atomic distances in all $Fe_{1-x}Sn_xBi_2Se_4$ ($0 \leq x \leq 0.5$) compounds are gathered in Table 3. The software Diamond [28] was utilized to create a graphic representation of the crystal structure with ellipsoid representations (98% probability level) for all atoms.

2.2.2.4 Differential Scanning Calorimetry (DSC)

DSC measurements were performed on finely ground powder of the synthesized materials in order to confirm the phase purity and also to determine the melting and crystallization temperatures. DSC data were recorded using approximately 10-20 mg of the synthesized material and an equivalent mass of alumina (Al_2O_3) as the reference. Both the sample and the reference, sealed in a small quartz tube under a residual pressure of 10^{-3} Torr, were placed on the sample and reference pans of a F401 DSC apparatus (NETZSCH). The sample and reference were simultaneously heated under flowing nitrogen gas to 1073 K at a rate of 20 K/min, isothermed for 2 min and then cooled to 300 K at a rate of 20 K/min. DSC data were recorded in two successive heating and cooling cycles. First heating and cooling DSC data are presented as they are most indicative of intrinsic thermal transitions.

2.2.2.5 Heat Capacity

Heat capacity was measured from 10 to 160 K under zero applied field using a PPMS system. C_p data were recorded using approximately 25 mg of the synthesized material. For accurate determination of the heat capacity, the addenda measurement, which records the heat capacity of the grease (used for thermal contact) and the platform, was subtracted from the heat capacity obtained from the measurement of sample, grease and platform.

2.3 Transport Properties Measurement

2.3.1 Low Temperature Resistivity, Seebeck

A number of different instruments were used to determine the electronic transport properties of the synthesized and densified materials.

Low temperature (2K – 300K) electronic transport measurements were performed on mirror polished prismatic samples under pressures below 10^{-6} torr in a custom built cryostat. These measurements were performed by our collaborators research group (Prof. Ctirad Uher). Electrical resistivity (ρ) was measured using the standard four-probe method in a Quantum Design Physical Property Measurement System (PPMS). The low temperature ρ measurements and S measurements for $FeSb_{2-x}Bi_xSe_4$ were performed under pressures of 10^{-3} torr using a PPMS equipped with the Thermal Transport Option (TTO).

High Temperature (300K - $\geq$500K) electronic transport measurements, ρ and S, were performed on prismatic samples of the select compositions in an ULVAC-RIKO ZEM-3. These measurements were performed on prismatic bars that were polished to a mirror finish. Both

material properties were measured simultaneously under a partial pressure of He. Instrument precision on the ZEM-3 is ±4%.

2.3.2 Hall Effect

Hall effect measurements were performed on the selected compositions from 5 K to 300 K for the low temperature scan using a Quantum Design MPMS system. Hall measurements between 280 K and 823 K for the high temperature scan were measured using a magnetic field of 1T in a custom-made apparatus consisting of a large Oxford air-bore superconducting magnet cryostat that accommodates a small tubular oven and a Hall insert. These measurements were performed on densified powders of select materials that were formed into prismatic bars. The instrument uncertainty on Hall coefficient data is ±5%. Carrier concentration and carrier mobility were subsequently extracted from the electrical resistivity and Hall coefficient data.

2.4 Magnetic Properties

Magnetic susceptibility data were collected using a Superconducting Quantum Interference Device (SQUID) magnetometer (Quantum Design MPMS XL- SQUID). All of the measurements were conducted on powders (40 mg – 70 mg) packed in gelatin capsules. For the low temperature scans, direct current (DC) Zero-Field-Cooled (ZFC) and Field-Cooled (FC) magnetic susceptibility measurements were performed over temperatures ranging from 2 K to 300 K under an applied field of 100 Oe. All samples were first cooled from room temperature to 2 K without an external field (ZFC), after which a 100 Oe external field was applied and the susceptibility recorded upon heating to 300 K. Next, the field was left on while the sample was cooled back down to 2 K. FC Susceptibility was measured upon reheating to 300 K. The high temperature scan was conducted in a similar fashion, except that no cooling was performed since the scan started at room temperature. Once the sample was placed inside the apparatus, the external field (100 Oe) was turned on and immediately the ZFC susceptibility was measured upon heating to 550 K. The external field was left on (100 Oe) and the sample was cooled back down to 300 K. The FC susceptibility was again measured upon heating up to 550 K. After the FC measurement was completed, the external field was turned off while the furnace was still at 550 K and the sample

was cooled down to 300 K under zero applied field. Thereafter, another ZFC susceptibility (ZFC-2) curve was taken upon reheating to 550 K under an external field of 100 Oe. Isothermal magnetization measurements were carried out at temperatures between 2K and 300K in DC magnetic fields varying from 0 to 30 kOe

2.5 X-ray Photoelectron Spectroscopy (XPS)

To assess the oxidation state of various metal atoms in the synthesized materials, XPS analysis was performed on selected compositions using hand pressed 3 mm diameter pellets. XPS spectra were collected for each pellet using a Kratos Axis Ultra XPS equipped with a monochromatic Al source (15 kV, 10 mA). Wide scans were acquired using an analyzer pass energy of 160 at 1 eV steps. Selected regions were scanned using a pass energy of 20 eV at 0.02 eV steps. Specimens were loaded into the transfer chamber and pumped for a 12 h period in order to reach pressures of less than 5×10^{-7} Torr. The analysis chamber was kept at approximately 10^{-9} Torr during the measurement. Post processing analysis was performed using Casa XPS.

Chapter 3

Coexistence of High Tc Ferromagnetism and n-type Electrical Conductivity in FeBi$_2$Se$_4$

3.1 Introduction

Semiconductors exhibiting ferromagnetism and high electrical conduction above 300 K are of tremendous importance for the fabrication of practical spintronic devices.[1] Although these properties are accessible in metallic ferromagnets such as iron, cobalt and nickel, the magnetic and conducting sublattices in such materials strongly interact making it difficult to decouple the magnetic and semiconducting functionalities. However, the ability to independently control and manipulate ferromagnetism or electrical conduction within the material using external stimuli (electrical or magnetic field) is necessary for applications, such as giant magnetoresistance memories, field sensors, spin transistors and quantum information processing.[2-5] Therefore, ferromagnetic semiconductors (FMSs) have attracted tremendous attention due to the ability to tune the electrical conductivity via substitution chemistry and doping. The most popular approach to create FMS consists of substituting non-magnetic atoms in conventional semiconductors by magnetic atoms in order to generate the so-called diluted magnetic semiconductors (DMSs).[6-11] Most studied DMSs are *p*-type III-V and II-VI semiconductors in which the III or II atoms are partially substituted by Mn. In these materials, Mn atoms serve both as acceptors (providing holes) and as the magnetically active species (providing localized magnetic moments) in the semiconducting hosts. Therefore, the insertion of Mn atoms in these systems simultaneously alters the density of free carriers (holes) responsible for the electrical

conduction and the concentration of localized spins (Mn^{2+}, 3d) responsible for the ferromagnetism. In addition, the Mn atoms in these systems are randomly distributed in the crystal lattice and occasionally enter into interstitial sites rather than occupying the crystallographic positions of the substituted atoms.[12-14] The inability to independently control (a) the effective concentration of Mn atoms, (b) the carrier density and (c) the Mn – Mn separation in Mn-doped III-V and II-V semiconductors has limited the Curie temperatures (T_c) of p-type DMSs to 185 K in $Ga_{1-x}Mn_xAs$, despite tremendous efforts to reach T_c above 300 K.[3,15,16] P-type DMSs obtained via Mn substitution in group IV semiconductors (Si, Ge, SiGe) have also been investigated. Considerably larger ordering temperatures up to 400 K have been observed for instance in $Ge_{1-x}Mn_x$ films.[2,17,18] In these systems, the incorporation of Mn induced the formation of small Mn-rich precipitates (2-6 nm in diameter) randomly dispersed within the Mn-doped group IV semiconducting matrix. These precipitates are believed to be responsible for the high ordering temperature of the resulting $Ge_{1-x}Mn_x$ films.

N-type ferromagnetic semiconductors (n-FMSs), compared with the large volume of work on p-type DMSs, are poorly studied. However, n-FMSs are particularly interesting for semiconductor spintronics due to the high mobility of electrons and their remarkably long spin lifetimes in conventional semiconductors such as Si, GaAs, etc. [19-21] N-type semiconducting behavior has been observed in FMSs such as $(In_{1-x}Fe_x)As$,[22] TiO_2,[23] $CdMnGeP_2$,[24] and $CdCr_2Se_4$.[25] These n-FMSs exhibit low Curie ordering temperatures with the highest ordering temperature, $T_c \sim 132$ K observed for the seleno-spinel $CdCr_2Se_4$.[25] Although $CdCr_2Se_4$ is not a conventional device material, its ability to epitaxially grow on conventional semiconductors such as GaAs to form $CdCr_2Se_4$/GaAs heterostructures has been demonstrated.[21] Furthermore, electrical injection of spin-polarized electrons from the n-FMS $CdCr_2Se_4$ into the GaAs-based device heterostructure was successfully realized.[21] This important result suggests that beyond Mn-doped

III-V, II-V and IV semiconductors, high-T_c n-type and p-type FMSs from other material systems that can be grown on conventional device substrates are very attractive for semiconductor spintronics.

Over the past five years, we have explored various strategies to rational design and discovery of new high-T_c ferromagnetic semiconducting structures encompassing ordered arrays of the magnetic atoms embedded within the semiconducting network of non-magnetic atoms. Our approach focuses on the crystal engineering of the atomic structure of low-symmetry semiconducting main group metal chalcogenides through chemical substitution of magnetic transition-metal atoms at targeted non-magnetic atomic positions. The structural and compositional flexibility of the resulting low-symmetry magnetic semiconducting transition metal chalcogenides (TMCs) enable access to a large variety of electronic and magnetic properties through careful solid solution and doping studies.[26-33] For example, we have recently identified the fascinating class of ternary magnetic semiconductors, MPn_2Se_4 (M = Fe, Mn; Pn = Sb, Bi).

The compounds are isostructural, crystallizing in the monoclinic space group *C*2/*m* (#12). The crystal structure (**Figure 3.1**) can be divided into two types of building units, denoted A and B, alternating along [001]. The unit A is built of paired rods of face-sharing monocapped trigonal prisms alternating along the *a*-axis with a $[M_nSe_{4n+2}]$ single-chain of edge-sharing octahedra running parallel to [010]. The building unit B is a NaCl-type layer separating adjacent units A. The distribution of M and Pn atoms in the crystal structure is so that the $[M_nSe_{4n+2}]$ single-chain within unit A is exclusively occupied by transition metal atoms (M = Mn or Fe), whereas various degrees of mixed occupancy between Pn and M atoms is observed in the remaining metal positions.
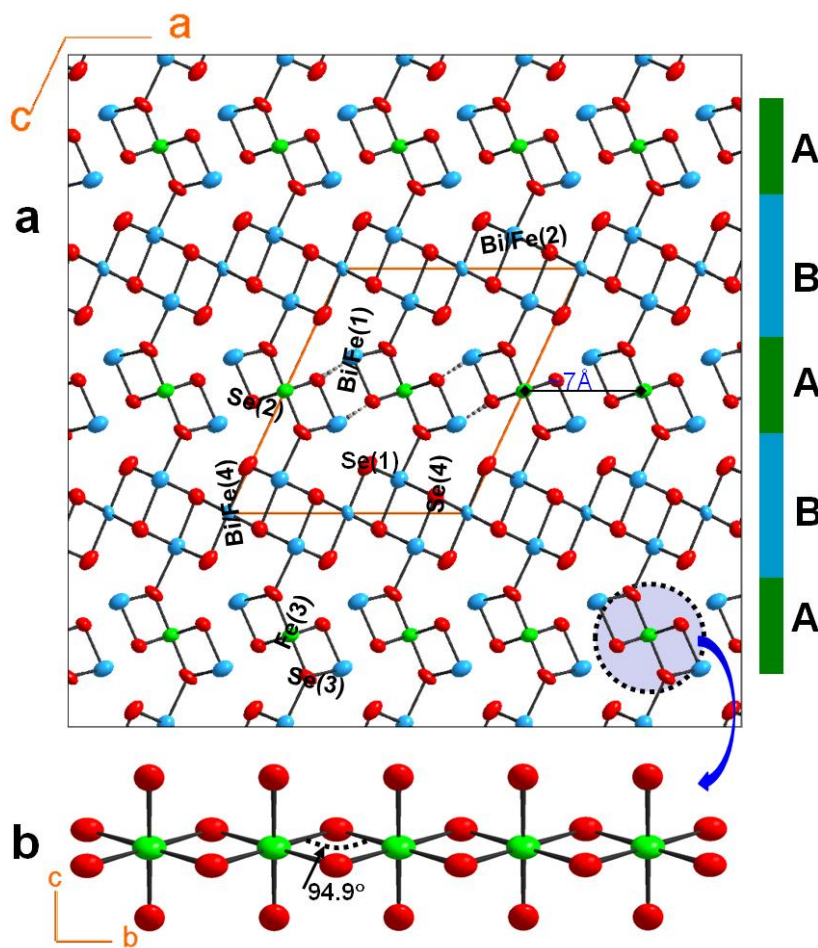
Figure 3. 1 Crystal structure of $FeBi_2Se_4$ at 300 K. a, Projection of the crystal structure along [010]. The building layers A and B alternating along the *c*-axis are highlighted. Ellipsoids are set at 98% probability for all atoms. Broken lines indicate (Bi/Fe) – Se interactions longer than 3.13 Å. b, Structure of the magnetic sublattice featuring the 1D $[Fe(3)]_nSe_{4n+2}$ straight chain of edge-sharing $FeSe_6$ octahedra.

Despite the close similarity between their crystal structure, the dominant magnetic ordering in various compositions strongly depends on the nature of the magnetic atom (Mn, Fe) within the $[M_nSe_{4n+2}]$ chains (*magnetic subunit*). For instance, antiferromagnetic (AFM) ordering was observed in $MnSb_2Se_4$,[28] whereas $FeSb_2Se_4$ showed ferromagnetic behavior with a Curie transition temperature above 300 K.[27] Interestingly, the dominant charge carrier type (electrons or holes) in MPn_2Se_4 can be manipulated by altering the nature of Pn atom within the network (*semiconducting subunit*) separating adjacent $[M_nSe_{4n+2}]$ chains. For example, *p*-type semiconducting behavior was observed in $MnSb_2Se_4$,[28] and $FeSb_2Se_4$,[27] whereas the bismuth analog $MnBi_2Se_4$ exhibits *n*-type semiconductivity.[33] This ability to independently control the dominant magnetic ordering and carrier type within the crystal lattice of MPn_2Se_4 through chemical manipulation of the composition of various structural subunits makes it possible to create both *n*-type and *p*-type MPn_2Se_4 FMSs. Here, we report high-T_c ferromagnetism and large *n*-type electrical conductivity in $FeBi_2Se_4$, the bismuth analog of the high-T_c *p*-type ferromagnet $FeSb_2Se_4$.[27] Magnetic susceptibility data from 2 K to 600 K confirm ferromagnetic ordering in $FeBi_2Se_4$, with a Curie temperature $T_c \sim 450$ K. Electronic charge transport (thermopower and electrical conductivity) and Hall-effect data indicate that $FeBi_2Se_4$ is an *n*-type degenerate semiconductor. Magnetoresistance data at 130 K reveal the presence of spin-polarized electrons suggesting that $FeBi_2Se_4$ is a promising candidate for spintronic applications.

3.2 Results and Discussion

3.2.1 Single Crystal

Polycrystalline powder of $FeBi_2Se_4$ was synthesized by solid state reaction of high purity elements at 750 K for 72 h. Single crystals, suitable for X-ray structure determination, were grown by annealing the as-synthesized polycrystalline powder of $FeBi_2Se_4$ at 915 K for 9 days. Careful analysis of single-crystal X-ray diffraction data at 300 K indicates that $FeBi_2Se_4$ (Table 1) is isostructural with $FeSb_2Se_4$,[27] crystallizing in the monoclinic space group $C2/m$ (# 12) with lattice parameters $a = 13.353(2)$ Å, $b = 4.1171(3)$ Å, $c = 15.069(3)$ Å, $\beta = 115.04(3)°$, and $V = 750.6(2)$ Å^3. It is interesting to note that despite the large difference ($\Delta R/R \sim 54\%$) in the effective ionic radii of Sb^{3+} (76 pm) and Bi^{3+} (117 pm) in octahedral coordination,[39] the complete substitution of antimony by bismuth in the structure of $FeSb_2Se_4$ maintains the overall symmetry of the original structure essentially unchanged with only marginal increase in the lattice parameters. This confirms the remarkable structural and compositional flexibility of the $FeSb_2Se_4$ structure type.

The structure of $FeBi_2Se_4$ can be divided into two types of layered units denoted as A and B parallel to ab planes and alternating along the c-axis (**Fig. 3.1**). Four crystallographically independent metal positions, two general positions M1($4i$) and M2($4i$) and two special positions M3($2c$) and M4($2a$) (Table 2) were found in the crystal structure. The M1($4i$) site is located in a [1+2+2] distorted square pyramidal geometry of Se atoms, whereas atoms at M2($4i$), M3($2c$) and M4($2a$) positions are octahedrally coordinated by Se atoms (Table 3). Within layer-A, the M1($4i$) position is mixed occupied by 85%Bi+15%Fe, whereas the M3 ($2c$) site is fully occupied by Fe. The flattened $Fe(3)Se_{[2+4]}$ octahedra (with two short axial bonds and four long equatorial bonds) share edges to form $[Fe(3)_nSe_{4n+2}]_\infty$ single-chains (1D) running along the b-axis (**Fig. 3.1b**). The intra-chain Fe – Fe distance is 4.128(1) Å. Likewise, adjacent $[Bi/Fe(1)]Se_5$ square pyramids also share edges to form a double-chain running along the b-axis and parallel to the $[Fe(3)_nSe_{4n+2}]_\infty$ single-chains. Therefore, layer-A can be described as consisting of a parallel arrangement of $[Fe(3)_nSe_{4n+2}]_\infty$

single-chains along the *a*-axis separated by a double-chain of edge-sharing [Bi/Fe(1)]Se$_5$ square pyramids. The distance between adjacent [Fe(3)$_n$Se$_{4n+2}$]$_\infty$ single-chains within layer-A is 6.996(1) Å suggesting that they are magnetically isolated from each other. The M2(4*i*) and M4(2*a*) positions within layer-B are mixed occupied by Bi and Fe atoms. While the M2 sites with distorted [2+1+1+2] octahedral coordination geometry contain 85%Bi+15%Fe, the M4 position with nearly perfect octahedral geometry (Table 3.3) is occupied by 60%Bi+40%Fe. Adjacent [M2]Se$_6$ and [M4]Se$_6$ octahedra share all edges to build a three-octahedra thick NaCl-type layer denoted by B. Adjacent layers A and B are connected to each other through M1 – Se3 – M2 linkage to form a three-dimensional (3D) structure. The chemical composition obtained from the refinement of the distribution of Fe and Bi atoms in various metal positions within the crystal structure of FeBi$_2$Se$_4$ suggests that Fe, Bi and Se exist in the 2+, 3+ and −2 oxidation states, respectively.

3.2.2 Magnetism

To evaluate the magnetic behavior of FeBi$_2$Se$_4$, temperature dependent magnetic susceptibility measurements were carried out from 2 K to 600 K under an applied field of 100 Oe using a superconducting quantum interference device (SQUID) magnetometer. The large room temperature value of the magnetic susceptibility, 5 emu/Oe.mole Fe^{2+}, indicates that FeBi$_2$Se$_4$ is ferromagnetic with $T_c > 300$ K. Low temperatures (T < 300 K) field-cooled (FC) and zero-field-cooled (ZFC) magnetic susceptibility (**Figure 3.2a**) overlap from ~125 to 300 K and gradually increase with decreasing temperature. A sharp drop in the susceptibility and a divergence of the ZFC and FC curves is observed with further cooling below 125 K. An anomalous increase in magnitude of the heat capacity (C_p) was also observed around the magnetic transition (**Figure 3.2b**). This suggests that the magnetic transition is of first-order and presumably results from a structural transition below 125 K. To further investigate the origin of such a transition, we analyzed

changes in the unit cell parameters and the crystal structure of $FeBi_2Se_4$ as the single crystal is cooled from 400 to 100 K. A plot of the relative change in the lattice parameters ($\Delta L/L$) as a function of temperature indicates a preferential contraction of a and b parameters, whereas contraction along the c-axis is marginal. This results in a small distortion of the $Fe(3)Se_{[2+4]}$ octahedra within layer A. At 100 K, the apical $Fe(3) -$ Se bonds expand by 0.16%, whereas the equatorial bonds contract by 0.54% (Supplementary Table 3). Such small alteration in the geometry of edge-sharing octahedra building the $[Fe(3)_nSe_{4n+2}]_\infty$ single magnetic chains changes the distribution of spins within the $3d^6$ orbital of Fe^{2+}, which in turn affect the magnetic susceptibility of $FeBi_2Se_4$ below 125 K. However, the compound remains ferromagnetic below 125 K. A similar magnetic transition was observed in the susceptibility curves of $FeSb_2Se_4$.[27] The magnetic susceptibility of $FeBi_2Se_4$ above 300 K gradually decreases with rising temperature up to 450 K, at which point a sharp drop in the susceptibility is observed (**Fig. 3.2c**). Thereafter, the susceptibility remains constant with further increase in the temperature. This indicates that $FeBi_2Se_4$ is a ferromagnetic compound with $T_c \sim 450$ K. Field dependent magnetization loops at 300 and 400 K (**Fig. 3.2d**) show the characteristic S-shape of a ferromagnet with a coercive field of 300 Oe and 110 Oe, respectively, while a very low coercive field is observed at 450 K and above. This is consistent with the FM ordering up to 450 K.

Interestingly, the magnetization does not reach saturation suggesting a large degree of spin disorder with a high magnetic anisotropy, which may arise from the 1D structure of the $[Fe(3)_nSe_{4n+2}]_\infty$ single magnetic chains. Taking into account the large intra-layer distance of ~ 7 Å and the inter-layer separation of ~ 15 Å between $[Fe(3)_nSe_{4n+2}]_\infty$ magnetic chains within the crystal structure of $FeBi_2Se_4$, we attribute the high-T_c FM behavior to a combination of weak FM interactions between adjacent Fe atoms within individual $[Fe(3)_nSe_{4n+2}]_\infty$ magnetic chain and long-range coupling of localized intra-chain moments via formation of overlapping bound magnetic polarons (BMPs) and/or carrier-mediated mechanisms.
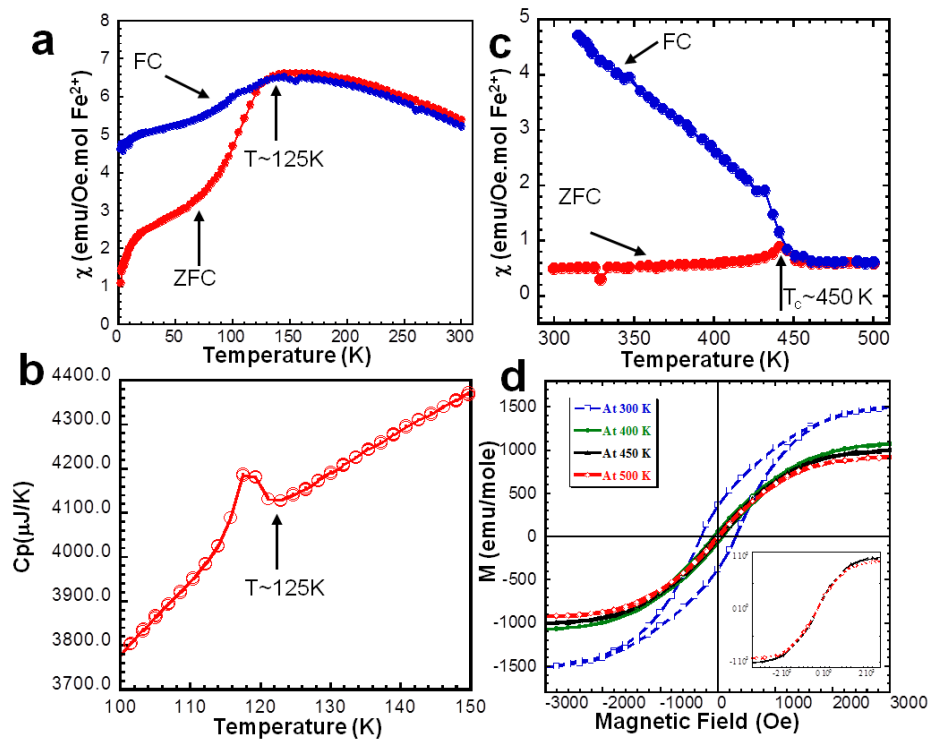
Figure 3. 2 Magnetic properties and heat capacity of $FeBi_2Se_4$. a, Low temperatures (T < 300 K) field-cooled (FC) and zero-field-cooled (ZFC) magnetic susceptibility measured under 100 Oe showing a magnetic transition at 125 K. b, Temperature dependent heat capacity highlighting an anomalous increase in magnitude around the magnetic transition temperature. c, High temperature FC and ZFC magnetic susceptibility measured under 100 Oe showing a Curie transition temperature at ~450

The flattened shape of the $[Fe(3)]Se_{2+4}$ octahedra within the magnetic chains, induces a high-spin distribution of $3d^6$ electrons leading to a total spin value of $S = 2$. The intra-chain magnetic

33

interaction between adjacent Fe atoms, 4.128 Å apart, is likely achieved by indirect exchange interaction through the bridging Se(2) atom (Fig.1b). The Fe(3) – Se(2) – Fe(3) bond angle of 94.9° suggests weak FM coupling of adjacent Fe atoms within $[Fe(3)_nSe_{4n+2}]_\infty$ single magnetic chains.[40-42] This implies a non-zero localized magnetic moment for individual $[Fe(3)_nSe_{4n+2}]_\infty$ chains. The remaining metal sites (M1, M2 and M4) in the crystal structure contain various amounts of Fe mixed with Bi atoms. Therefore, each Bi/Fe metal position within the semiconducting network separating adjacent $[Fe(3)_nSe_{4n+2}]_\infty$ chains is a potential site for the nucleation of BMPs due to the interaction of itinerant electrons and localized Fe $(3d^6)$ spins.[43,44] The interaction of BMPs with the localized moment of $[Fe(3)_nSe_{4n+2}]_\infty$ chains within their orbits enables FM coupling on neighboring $[Fe(3)_nSe_{4n+2}]_\infty$ chains falling within the orbit of the same BMP. Because of the short separation between Bi/Fe sites in the crystal structure, the formation of a high density of overlapping BMPs can be anticipated throughout the semiconducting network. Therefore, long-range FM ordering of localized $[Fe(3)_nSe_{4n+2}]_\infty$ moments in the crystal structure can be established. Evidence of a significant contribution of BMPs to the FM ordering in $FeBi_2Se_4$ is provided by the large values of magnetic susceptibility, as well as the S-shape of the magnetization loop above T_c.

3.2.3 Electronic Properties

The most interesting observation is the coexistence in $FeBi_2Se_4$ of high-T_c ferromagnetism with n-type conductivity. The electrical conductivity at zero-field (**Figure 3.3**) gradually decreases with rising

temperature, from ~1800 S/cm at 2 K to 900 S/cm at 550 K, which is typical behavior for heavily doped

semiconductors. The temperature dependent electrical conductivity data above 50 K are well fit by the power law $T^{-\alpha}$ as expected for acoustic phonon scattering of charge carriers.[45] Interestingly, the power exponent decreases from $\alpha \approx 0.54$ for electrical conductivity data at temperatures above 130 K to $\alpha \approx 0.26$ for data between 50 K and 130 K. A plot of the relative change in the electrical conductivity as a function of temperature also indicates an increase, around 130 K, of the rate of conductivity increase with decreasing temperature. The decrease in the power exponent is attributed to the above described anisotropic lattice contraction upon cooling below 130 K. Within this temperature regime ($T < 130$ K), the contraction of the Bi/Fe(1) − Se(2) bond below 3.13Å results in the connectivity of the crystal structure of $FeBi_2Se_4$ into a three-dimensional network.
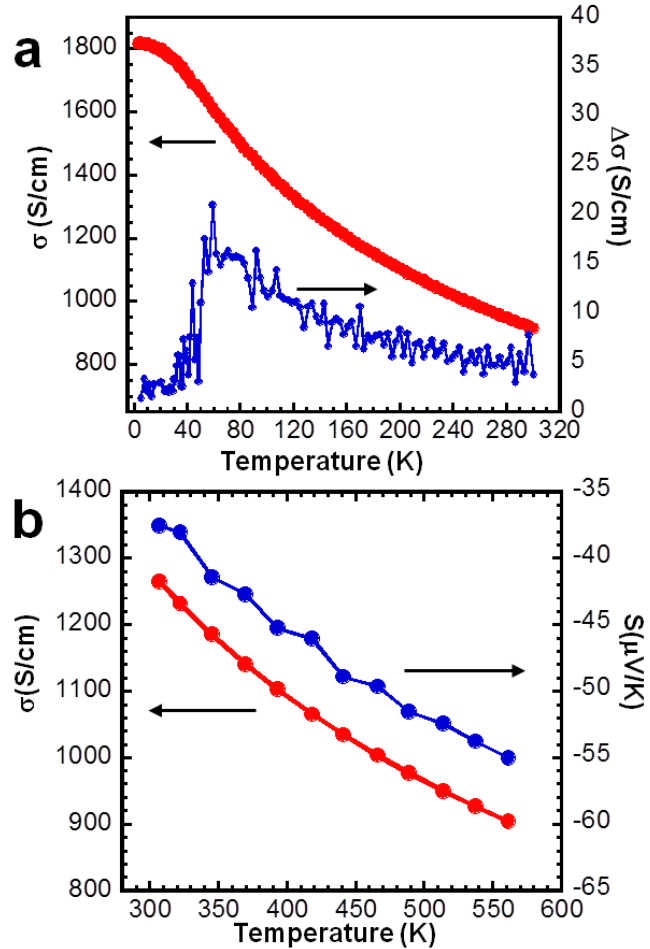
Figure 3. 3 Electrical properties of $FeBi_2Se_4$ as a function of temperature. a, Electrical conductivity (σ) and relative variation in electrical conductivity ($\Delta\sigma$) below 300 K. A sharp increase in the slope is observed around 130 K. b, Electrical conductivity and thermopower (S) above 300 K.

This induces an increase in the electrical conductivity due to a decrease in the electrical band gap.

Hall Effect measurement between 300 K and 823 K reveal a negative Hall coefficient (R_H), indicating electrons as the majority charge carrier (**Fig. 3.4a**). The *n*-type character of the electrical conduction in the high-T_c ferromagnet $FeBi_2Se_4$ is also supported by the negative values of the thermopower (**Fig. 3.3b**). The thermopower increases with rising temperature from -37μV/K at 300K to -55 μV/K at 575K. Carrier (electron) density extracted from the Hall effect measurement is 4×10^{19} cm^{-3} at 300 K and exponentially increases with rising temperature to 16×10^{19} cm^{-3} at 823 K (**Fig. 3.4b**). This trend is consistent with the thermally activated behavior expected in intrinsic semiconductors. Fitting of the high temperature ($T > 400$ K) data using the exponential function $n(T) \sim \exp(-E_g/2k_BT)$ yields an electrical band gap $E_g =$

0.24 eV. This confirms $FeBi_2Se_4$ as a narrow band gap n-type ferromagnetic semiconductor with $T_c > 400$ K.

Interestingly, high electron mobility, ~190 cm^2/V.s (**Fig. 3.4c**), is observed at 300 K, which is a reasonable number for a doped ferromagnetic semiconductor with carrier density of ~10^{19} cm^{-3}. Also, the mobility decreases with rising temperature accordingly to the power law $\mu \sim T^{-\alpha}$, with $\alpha = 1.42$, which is very close to the value of $\alpha = 1.5$ expected for carrier transport dominated by acoustic phonon
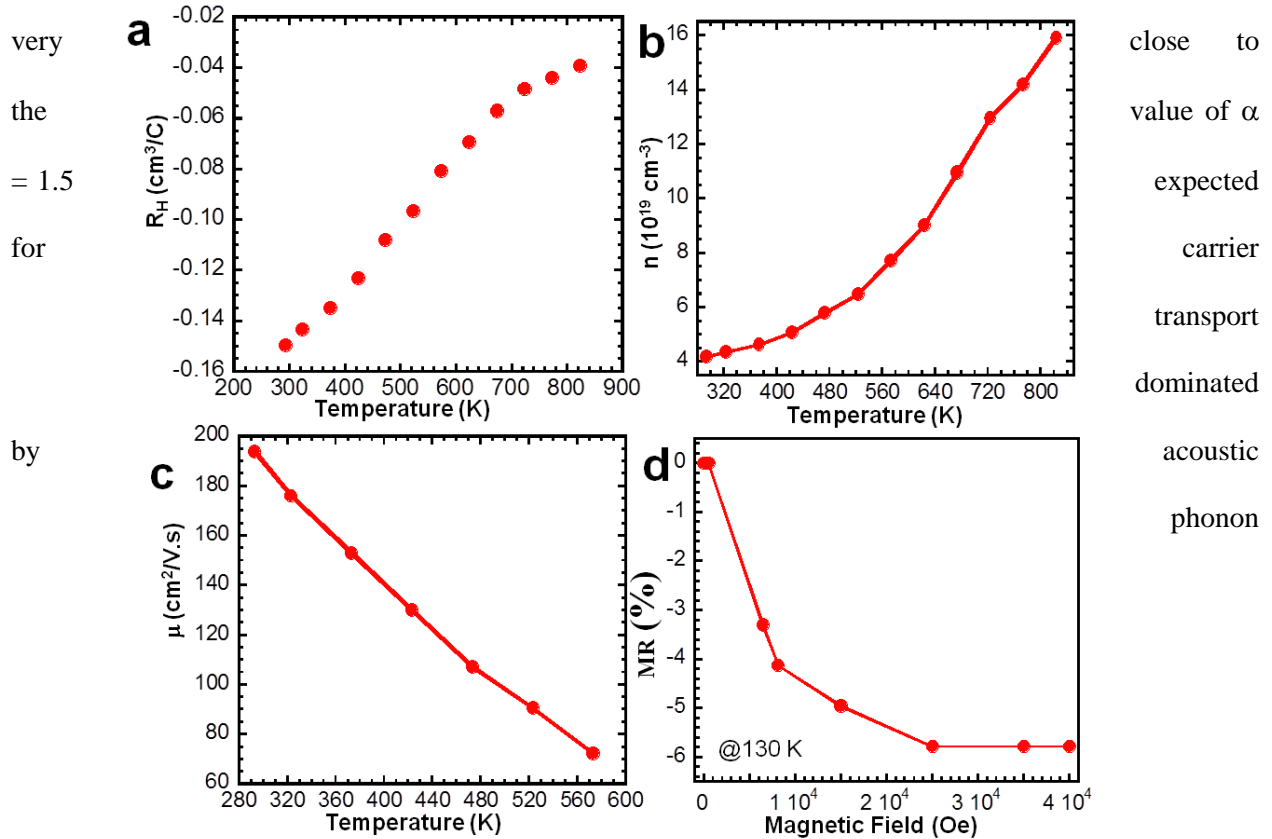
Figure 3. 4 High temperature electronic transport and magnetoresistance of $FeBi_2Se_4$. a, Hall coefficient. b, Carrier concentration. c, Carrier mobility. d, Magnetoresistance at 130 K.

scattering.[45] These results are comparable with carrier transport in non-magnetic semiconductors,

suggesting a weak electronic interaction, under zero-field, between free electrons in the semiconducting sublattice and localized spins in the magnetic sublattice of the $FeBi_2Se_4$ ferromagnet. However, the coexistence within the semiconducting sublattice of localized spins and a high density of free electrons with high mobility, arising from the intermixing of Bi and Fe at various metal positions, is favorable to the formation of spin-polarized itinerant electrons leading to overlapping BMPs, which are believed to be responsible for the large magnetic susceptibility and high-T_c observed in $FeBi_2Se_4$.

$FeBi_2Se_4$ shows negative magnetoresistance (MR = $[\rho(H)- \rho(0)]/\rho(0)$, where $\rho(H)$ and $\rho(0)$ are the resistivity at a magnetic field H and 0, respectively) values (**Fig. 3.4d**). This indicates a reduction in the scattering of free-electrons by localized spins due to the alignment of magnetic moments of Fe atoms and spins of free electrons parallel to the applied field (H). The MR at 130 K increases rapidly with rising field and reaches saturation at MR~ − 6% under an applied field of 25 kOe. The low value of the MR provides evidence for the presence of spin-polarized electrons within the semiconducting sublattice and their weak interaction with localized moments within the magnetic sublattice.

3.3 Concluding Remarks

In summary, we have demonstrated a new high-T_c (> 400 K) n-type ferromagnetic semiconductor with high carrier mobility and high electrical conductivity. The unique combination of these two functionalities in $FeBi_2Se_4$ arises from the low-symmetry crystal structure of MPn_2Se_4, which enables the atomic-scale integration of two crystallographically independent magnetic and semiconducting sublattices. This allows independent alteration of the magnetic and/or the semiconducting behavior through the manipulation of the chemical composition of each sublattice. Predominantly FM ordering is observed with M = Fe ($FePn_2Se_4$) ,[27] and the AFM ordering is observed with M = Mn ($MnPn_2Se_4$),[28,33] while p-type or n-type electrical

conductivity is obtained for Pn = Sb (MSb_2Se_4),[27] or Pn = Bi (MBi_2Se_4).[33] Therefore, by integrating Fe within the magnetic sublattice and Bi within the semiconducting lattice, we have successfully designed an *n*-type FMS with $T_c > 400$ K and large electrical conductivity. To the best of our knowledge this combination of a large *n*-type conductivity and high-T_c ferromagnetism achieved in $FeBi_2Se_4$ has never been observed in any other FMS. The importance of this result for the future of spintronic research is two-fold. First, it shows that by decoupling electronically and structurally the magnetic and semiconducting functionalities at the atomic-scale, one can achieve both an *n*-type and *p*-type FMS with high a T_c. This should pave the way for the design and fabrication of spin-based semiconducting devices such as light-emitting diodes and field-effect transistors. Second, the ability to independently manipulate the chemistry of the semiconducting sublattice in the MPn_2Se_4 structure via substitution and/or doping without altering the chemistry of the magnetic sublattice can be exploited to study longstanding fundamental questions related to the mechanism of carrier-mediated ferromagnetism in spintronic materials.

3.4 References

(1)   Wolf, S. A.; Awschalom, D. D.; Buhrman, R. A.; Daughton, J. M.; von Molnar, S.; Roukes, M. L.; Chtchelkanova, A. Y.; Treger, D. M. *Science* **2001**, *294*, 1488.

(2)   Jamet, M.; Barski, A.; Devillers, T.; Poydenot, V.; Dujardin, R.; Bayle-Guillemaud, P.; Rothman, J.; Bellet-Amalric, E.; Marty, A.; Cibert, J.; Mattana, R.; Tatarenko, S. *Nat Mater* **2006**, *5*, 653.

(3)   Macdonald, A. H.; Schiffer, P.; Samarth, N. *Nat Mater* **2005**, *4*, 195.

(4)   Zutic, I.; Fabian, J.; Erwin, S. C. *Ibm J Res Dev* **2006**, *50*, 121.

(5)   Zutic, I.; Fabian, J.; Das Sarma, S. *Rev Mod Phys* **2004**, *76*, 323.

(6)   Dobrowolska, M.; Tivakornsasithorn, K.; Liu, X.; Furdyna, J. K.; Berciu, M.; Yu, K. M.; Walukiewicz, W. *Nat Mater* **2012**, *11*, 444.

(7)   Richardella, A.; Roushan, P.; Mack, S.; Zhou, B.; Huse, D. A.; Awschalom, D. D.; Yazdani, A. *Science* **2010**, *327*, 665.

(8)   Sawicki, M.; Chiba, D.; Korbecka, A.; Nishitani, Y.; Majewski, J. A.; Matsukura, F.; Dietl, T.; Ohno, H. *Nat Phys* **2010**, *6*, 22.

(9)   Dietl, T.; Ohno, H.; Matsukura, F.; Cibert, J.; Ferrand, D. *Science* **2000**, *287*, 1019.

(10)   Dietl, T. *Semicond Sci Tech* **2002**, *17*, 377.

(11)   Dietl, T. *Nat Mater* **2010**, *9*, 965.

(12)   Edmonds, K. W.; Boguslawski, P.; Wang, K. Y.; Campion, R. P.; Novikov, S. N.; Farley, N. R. S.; Gallagher, B. L.; Foxon, C. T.; Sawicki, M.; Dietl, T.; Nardelli, M. B.; Bernholc, J. *Phys Rev Lett* **2004**, *92*.

(13)   Blinowski, J.; Kacman, P. *Phys Rev B* **2003**, *67*.

(14)   Yu, K. M.; Walukiewicz, W.; Wojtowicz, T.; Kuryliszyn, I.; Liu, X.; Sasaki, Y.; Furdyna, J. K. *Phys Rev B* **2002**, *65*.

(15)   Jungwirth, T.; Wang, K. Y.; Masek, J.; Edmonds, K. W.; Konig, J.; Sinova, J.; Polini, M.; Goncharuk, N. A.; MacDonald, A. H.; Sawicki, M.; Rushforth, A. W.; Campion, R. P.; Zhao, L. X.; Foxon, C. T.; Gallagher, B. L. *Phys Rev B* **2005**, *72*.

(16)   Wang, M.; Campion, R. P.; Rushforth, A. W.; Edmonds, K. W.; Foxon, C. T.; Gallagher, B. L. *Appl Phys Lett* **2008**, *93*.

(17)   Park, Y. D.; Hanbicki, A. T.; Erwin, S. C.; Hellberg, C. S.; Sullivan, J. M.; Mattson, J. E.; Ambrose, T. F.; Wilson, A.; Spanos, G.; Jonker, B. T. *Science* **2002**, *295*, 651.

(18)   Kang, J. S.; Kim, G.; Wi, S. C.; Lee, S. S.; Choi, S.; Cho, S.; Han, S. W.; Kim, K. H.; Song, H. J.; Shin, H. J.; Sekiyama, A.; Kasai, S.; Suga, S.; Min, B. I. *Phys Rev Lett* **2005**, *94*.

(19)   Oestreich, M. *Nature* **1999**, *402*, 735.

(20)   Kikkawa, J. M.; Awschalom, D. D. *Nature* **1999**, *397*, 139.

(21)   Kioseoglou, G.; Hanbicki, A. T.; Sullivan, J. M.; van 't Erve, O. M. J.; Li, C. H.; Erwin, S. C.; Mallory, R.; Yasar, M.; Petrou, A.; Jonker, B. T. *Nat Mater* **2004**, *3*, 799.

(22)   Hai, P. N.; Anh, L. D.; Tanaka, M. *Appl Phys Lett* **2012**, *101*.

(23)   Matsumoto, Y. *Science* **2001**, *294*, 1003.

(24)   Medvedkin, G. A.; Ishibashi, T.; Nishi, T.; Hayata, K.; Hasegawa, Y.; Sato, K. *Jpn J Appl Phys 2* **2000**, *39*, L949.

(25)   Sanford, N.; Davies, R. W.; Lempicki, A.; Miniscalco, W. J.; Nettel, S. J. *Phys Rev Lett* **1983**, *50*, 1803.

(26)   Anglin, C.; Takas, N.; Callejas, J.; Poudeu, P. F. P. *J Solid State Chem* **2010**, *183*, 1529.

(27)   Djieutedjeu, H.; Poudeu, P. F. P.; Takas, N. J.; Makongo, J. P. A.; Rotaru, A.; Ranmohotti, K. G. S.; Anglin, C. J.; Spinu, L.; Wiley, J. B. *Angew Chem Int Edit* **2010**, *49*, 9977.

(28)   Djieutedjeu, H.; Makongo, J. P. A.; Rotaru, A.; Palasyuk, A.; Takas, N. J.; Zhou, X. Y.; Ranmohotti, K. G. S.; Spinu, L.; Uher, C.; Poudeu, P. F. P. *Eur J Inorg Chem* **2011**, 3969.

(29)   Matsushita, Y.; Ueda, Y. *Inorg Chem* **2003**, *42*, 7830.

(30)   Mrotzek, A.; Kanatzidis, M. G. *Acc Chem Res* **2003**, *36*, 111.

(31)   Poudeu, P. F. P.; Takas, N.; Anglin, C.; Eastwood, J.; Rivera, A. *J Am Chem Soc* **2010**, *132*, 5751.

(32)   Poudeu, P. F. P.; Djieutedjeu, H.; Sahoo, P. *Z Anorg Allg Chem* **2012**, *638*, 2549.

(33)   Ranmohotti, K. G. S.; Djieutedjeu, H.; Poudeu, P. F. P. *J Am Chem Soc* **2012**, *134*, 14033.

(34)   Makongo, J. P. A.; Misra, D. K.; Zhou, X. Y.; Pant, A.; Shabetai, M. R.; Su, X. L.; Uher, C.; Stokes, K. L.; Poudeu, P. F. P. *J Am Chem Soc* **2011**, *133*, 18843.

(35)   Makongo, J. P. A.; Misra, D. K.; Salvador, J. R.; Takas, N. J.; Wang, G. Y.; Shabetai, M. R.; Pant, A.; Paudel, P.; Uher, C.; Stokes, K. L.; Poudeu, P. F. P. *J Solid State Chem* **2011**, *184*, 2948.

(36)   Misra, D. K.; Makongo, J. P. A.; Sahoo, P.; Shabetai, M. R.; Paudel, P.; Stokes, K. L.; Poudeu, P. F. P. *Sci Adv Mater* **2011**, *3*, 607.

(37)   SHELTXL, v6.12 (Bruker Analytical X-ray Instruments, Inc., Madison, WI., 2000).

(38)   DIAMOND. Version 3.1a. (Crystal Impact GbR, Bonn, Germany, 2005).

(39)   Shannon, R. D. *Acta Crystallogr A* **1976**, *32*, 751.

(40)   Kanamori, J. *J Phys Chem Solids* **1959**, *10*, 87.

(41)   Goodenough, J. B. *J Phys Chem Solids* **1958**, *6*, 287.

(42)   Goodenough, J. B. *Phys Rev* **1955**, *100*, 564.

(43)   Wolff, P. A.; Bhatt, R. N.; Durst, A. C. *J Appl Phys* **1996**, *79*, 5196.

(44)   Kaminski, A.; Das Sarma, S. *Phys Rev Lett* **2002**, *88*.

(45)   Sze, S. M. *Physics of Semiconductors Devices* 2nd Edition ed.; Wiley, 1981.

Tables

Table 3. 1 Selected crystallographic data and details of structure determinations for $FeBi_2Se_4$ at 100 K, 300 K and
400 K

Formula sum	$FeBi_2Se_4$ (100 K | 300 K | 400 K)
Crystal system	Monoclinic
space group	$C2/m$ (#12)
Formula weight (g/mol)	789.65
Density (ρ_{cal}) (g/ cm^3)	7.05 | 6.99 | 6.96
Lattice parameters/Å	
$a =$	13.297(2) | 13.353(2) | 13.372(2)
$b =$	4.1037(3) | 4.1171(3) | 4.1277(4)
$c =$	15.038(3) | 15.069(3) | 15.072(2)
$\beta(°) =$	114.93(1) | 115.04(1) | 115.05(1)
Volume (Å^3); Z	744.1(2) | 750.6(2) | 753.7(2); 4
Crystal size (mm)	$0.05 \times 0.06 \times 0.15$
Crystal shape, color	Needle, Black
Diffractometer; Radiation/ Å	IPDS-2T (Stoe); λ(Mo-K_α) = 0.71073
ω range; $\Delta\omega°$; $2\theta_{max}$	180; 1; 58.5°
index range	$-18 \leq h \leq 18; -5 \leq k \leq 5; -20 \leq l \leq 20$
Measured reflections	6609 | 4131 | 4341
Unique reflections	1140| 1147 | 1149
R_{int}	0.078 | 0.120 | 0.1153

R_σ	0.040 | 0.093 | 0.078
μ/ cm^{-1}	685 | 680 | 676
No. of parameters	49
Extinction correction x =	0.00141(1) | 0.00166(1) | 0.00195(1)
Difference electron density (e/ $Å^3$)	+2.18 to −2.51| +2.96 to −1.71| +2.30 to −2.14
$R_1(Fo>4\sigma(Fo))^a$	0.027 | 0.038 | 0.037
wR_2 (all)[b]	0.064 | 0.086 | 0.077
GooF	1.070 | 1.061| 1.112

[a] $R_1 = \sum \left\| F_0 \right| - \left| F_c \right\| / \sum \left| F_0 \right|$, [b] $wR2 = \left[\sum w(F_0^2 - F_c^2)^2 / \sum w(F_0^2)^2 \right]^{1/2}$

Table 3. 2 Wyckoff positions, site occupancy factors (k), atomic coordinates, and equivalent isotropic displacement parameters (U_{eq}/pm^2) for all atoms in the asymmetric unit of FeBi$_2$Se$_4$ at 400 K | 300 K | 100 K. Estimated standard deviations corresponding to the last digits are indicated in parentheses.

Atom	Wyck.	k	x	y	z	U_{eq}
Bi1	4i	0.85(1)	0.2177(1) 0.2177(1) 0.2174(1)	0	0.3625(1) 0.3626(1) 0.3623(1)	376 240 130
Fe1	4i	0.15(1)	0.2177(1) 0.2177(1) 0.2174(1)	0	0.3625(1) 0.3626(1) 0.3623(1)	376 240 130
Bi2	4i	0.85(1)	0.3494(1) 0.3494(1) 0.3494(1)	½	0.1374(1) 0.1371(1) 0.1367(1)	315 199 115
Fe2	4i	0.15(1)	0.3494(1) 0.3494(1) 0.3494(1)	½	0.1374(1) 0.1371(1) 0.1367(1)	315 199 115
Fe3	2c		½	½	½	385 216 98
Bi4	2b	0.60(1)	½	0	0	257 138 67

45

Atom	Wyckoff	Occupancy	x	y	z	U_{eq}
						257
Fe4	2b	0.40(1)	½	0	0	138
						67
			0.5091(2)		0.1930(2)	257
Se1	4i		0.5091(2)	0	0.1929(2)	245
			0.5094(2)		0.1930(2)	168
			0.1138(2)		0.4559(1)	329
Se2	4i		0.1136(2)	½	0.4564(2)	199
			0.1132(2)		0.4565(2)	130
			0.3466(2)		0.3299(2)	328
Se3	4i		0.3469(2)	½	0.3298(2)	215
			0.3462(2)		0.3295(2)	141
			0.1635(2)		0.0670(1)	322
Se4	4i		0.1638(2)	0	0.0665(2)	211
			0.1635(2)		0.0663(2)	133

U_{eq} is defined as one-third of the trace of the orthogonalized U_{ij} tensor

Table 3. 3 Selected interatomic distances (Å) in $FeBi_2Se_4$. Standard deviations corresponding to the last digits are indicated in parentheses.

Bonds	400K	300K	100K	% contraction
Bi1|Fe1—Se2^i	2.710(3)	2.704(3)	2.706(2)	**+0.07**
Bi1|Fe1—Se(3, 3^{ii})	2.862(2)	2.860(2)	2.846(2)	−0.50
Bi1|Fe1—Se(2, 2^{ii})	3.134(2)	3.135(2)	3.129(2)	−0.19
Bi2|Fe2—Se(1, 1^v)	2.830(2)	2.823(2)	2.817(2)	−0.21
Bi2|Fe2—Se3	2.917(3)	2.917(3)	2.918(2)	**+0.03**
Bi2|Fe2—Se4^{vi}	3.013(3)	2.998(3)	2.983(2)	−050
Bi2|Fe2—Se(4, 4^v)	3.055(2)	3.047(2)	3.039(2)	−0.26
Fe3—Se(3, 3^{vii})	2.516(3)	2.514(3)	2.518(2)	**+0.16**
Fe3—Se2$^{(i, viii, ix, x)}$	2.806(2)	2.796(2)	2.781(2)	−0.54
ν_1	0.90	0.90	0.91	
Bi4|Fe4—Se(1, 1^{xii})	2.859(3)	2.857(3)	2.851(2)	−0.21
Bi4|Fe4—Se(4$^{xi, viii, vi, ix}$)	2.862(2)	2.858(2)	2.847(2)	−0.38
ν_2	0.99	1.00	1.00	

ν = (apical bond length) / (equatorial bond length)

 Operators for generating equivalent atoms:

(i) ½–x, ½–y, 1–z; (ii) x, −1+y, z; (iii) −½+x, −½+y, z; (iv) −½+x, ½+y, z; (v) x, 1+y, z; (vi) ½–x, ½–y, −z; (vii) 1–x, 1–y, 1–z; (viii) ½+x, ½+y, z; (ix) ½+x, −½+y, z; (x) ½–x, 3/2–y, 1–z; (xi) ½–x, −½–y, −z; (xii) 1–x, −y, −z.

Chapter 4

Engineering Magnetic Transistions in Fe$_{1-x}$Sn$_x$Bi$_2$Se$_4$ n-type Ferromagnetic Semiconductors through Manipulation of Spatial Seperation between Magnetic Centers

4.1 Introduction

The prospect of integrating a spin degree of freedom into current semiconducting platforms promises to improve the state of conventional electronics[1-3]. The materials needed to make this next generation of devices are magnetic semiconductors. The most widely studied class of materials is the dilute magnetic semiconductors (DMS's) based on III-V [4-6] and II-VI [7,8] semiconductors. The collective literature on these systems is large and is a result of the philosophical approach taken in designing these material systems. A top down approach is taken, in which non-magnetic semiconductors are doped with magnetic atoms to introduce a magnetic exchange interaction.[9,10] This approach has been useful in developing prototype systems in which these mechanisms can be studied. However, this strategy cannot be readily extended to the development of n-type analogues, since the p-type nature of most DMS is a result of doping associated with the introduction of the magnetic constituents into the crystal lattice. This can be seen by the overwhelming amount of literature reporting on p-type systems compared to the available studies on n-type analogues. The initial rush to synthesize p-type systems was inspired by calculations predicting p-type magnetic semiconductors with T$_c$ above room temperatures in wide band gap wurtzite systems, such as (Ga,Mn)N,[11] and (Zn,Mn)O,[12] which were subsequently

synthesized and shown to have high T_c. The origin of this robust magnetism remains disputed as it has been demonstrated that a form of crystallographic phase separation, spinodal decomposition, may occur in such systems.[13] Such spinodal decomposition is not a constrained occurrence, as it also occurs in (Zn,Cr)Te,[14] (Ga,Cr)N, Al(Cr)N[15] and even in the most prototypical DMS, (Ga,Mn)As.[16] There remains a difficulty in growing reliably high T_c magnetic semiconductors because of the competition between two functionalities (magnetic ion concentration and carrier concentration) on one cation site and the stability of binaries and defects. Significant focus has been placed on growing pristine thin films to achieve optimal effective magnetic ion concentrations and carrier concentrations. As a consequence, the bulk of magnetic semiconductor research has been reduced to a thermodynamic problem, in which emphasis has been placed on the integration of a metastable phase with random magnetic ion distributions while avoiding the formation of the more stable binary compounds and defect structures. Great strides have been made in the epitaxy of magnetic semiconductors with high nominal magnetic ion concentrations; however, the unrelenting focus on growth kinetics has overshadowed some of the nuances responsible for T_c and anisotropy. Idrobo *et al*.[17] has shown through density functional theory (DFT) that the ground magnetic state of Mn in a nonmagnetic crystal is dependent upon the inter-ionic distance between the Mn atoms. The ground state is strongly anti-ferromagnetic (AFM) for short inter-ionic distances (corroborated by the AFM coupling of Mn interstitials with Mn substitutes) and transitions to sequentially weaker AFM interactions as the distance increases, becoming more and more ferromagnetic (FM). This was further supported in our previous work on $Mn_{1-x}Sn_xBi_2Se_4$,[18] in which it was demonstrated that increasing the average Mn interatomic distance by substituting Mn^{2+} by Sn^{2+}, resulted in an AFM to FM transition. Further substitution resulted in a paramagnetic phase. Another important parameter for achieving high T_c in a magnetic

49

semiconductor is the magnetic ion distribution itself. Zunger *et al.*[19] showed through a first principles combinatory technique applied to supercell designs of Mn in GaAs that T_c in (Ga,Mn)As superlattices could be increased to as high as 350 K, while the T_c of a random alloy ($x_{Mn} = 8\%$) meets a limit of ~230 K. The study of atomic arrangements and the effect of these atomic arrangements on the ground magnetic state have been somewhat overlooked. When designing a magnetic semiconductor, one would want to: 1) avoid the interdependence of the magnetic ion concentration and the carrier concentration, 2) achieve atomic arrangements which favor high T_c, and 3) ensure that the magnetic ground state/phase is FM. In our previous work, we have designed and developed a new type of magnetic semiconductor with the general formula MPn_2Se_4 (M = Mn, Fe ; Pn = Sb, Bi) and have demonstrated an independent control over the magnetic ordering and carrier concentrations within the materials.[18,20-25] This is an example of a modular magnetic semiconductor, in which the functionalities present can be easily switched through chemical manipulation. We have shown that $FeSb_2Se_4$ is a p-type FM semiconductor with T_c ~ 450 K.[22] Replacing Sb by Bi to form $FeBi_2Se_4$ has resulted in the formation of an n-type FM semiconductor with T_c ~ 450 K.[25] Substitution of Fe with Mn results in $MnSb_2Se_4$,[20] a p-type AFM semiconductor and in $MnBi_2Se_4$,[18] an n-type AFM semiconductor. We have also shown a drastic change in the concentration of magnetic atoms through partial substitution of non-magnetic atoms at the magnetic site, while keeping the carrier concentration effectively constant.[21] Moreover, we have also demonstrated that the carrier concentration can be altered through doping at the Pn site while keeping the concentration of magnetic atoms essentially constant.[24] This flexibility in the manipulation of both carrier density and concentration of magnetic atoms derives from the separation within the crystal structure of the two substructures controlling the magnetic and semiconducting functionalities. In this work, we investigate the effect of partial substitution of Fe

by Sn on the redistribution of magnetic atoms within the crystal structure of $Fe_{1-x}Sn_xBi_2Se_4$ and the impact of such atomic rearrangements on the magnetic and electronic properties of the resulting
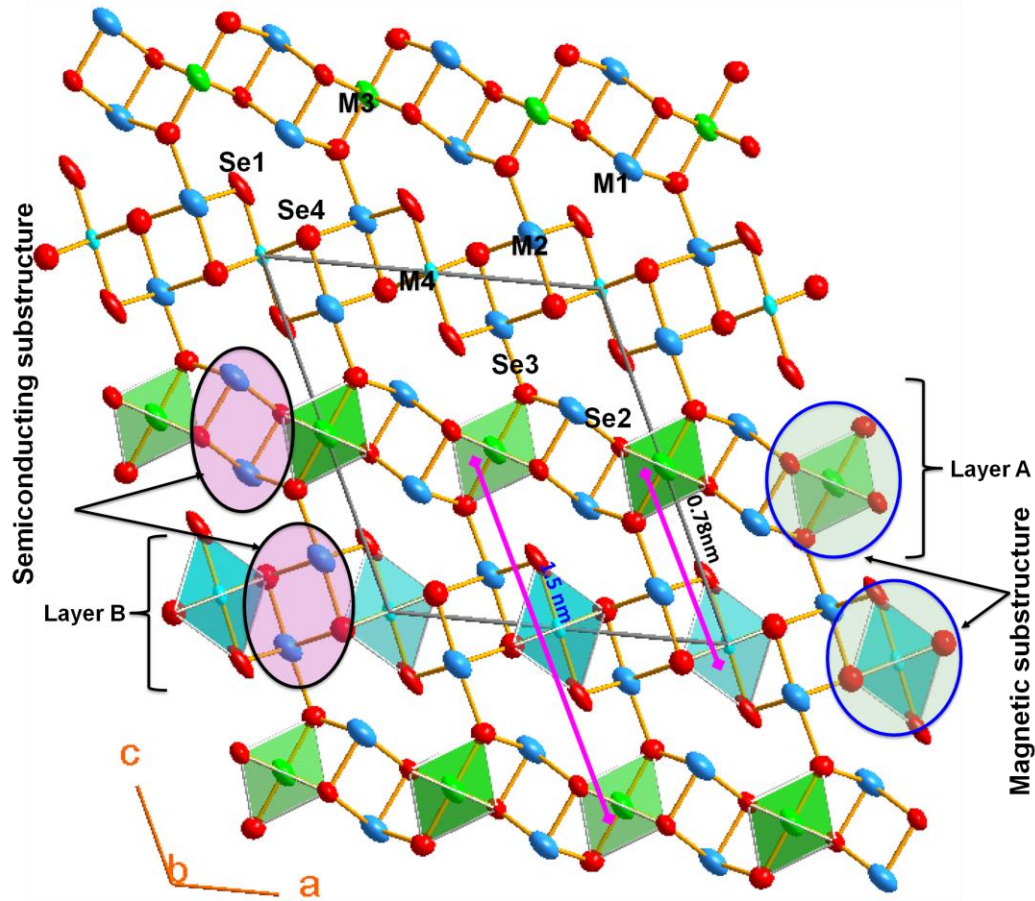
Figure 4. 1 Schematic representation of the crystal structure of $Fe_{1-x}Sn_xBi_2Se_4$ highlighting the main building blocks, layer-A and layer-B, as well as the two substructures controlling the electronic and magnetic properties.

phases. Our results show that all $Fe_{1-x}Sn_xBi_2Se_4$ samples are isostructural with the parent compound $FeBi_2Se_4$. The substitution of Fe by Sn leads to a preferential incorporation of Sn atoms at the M4(2b) site and an increased ordering of Bi atoms within the M1(4i) and M2(4i) sites (**Figure 4.1** and **4.2**). This results in increase separation between magnetic centers within the crystal lattice leading to a fully ordered structure for the composition $Fe_{0.5}Sn_{0.5}Bi_2Se_4$ (x = 0.5) (**Figure 4.1**). All samples maintain the *n*-type semiconducting behavior and the ferromagnetic-like character in the measured temperature range from 2 K to 300 K. Interestingly, low temperature

carrier density data reveal a surprising electronic transition from semiconducting to metallic behavior for the samples with x > 0.15 upon cooling below 150 K. In addition, high temperatures magnetic susceptibility data indicate a sharp drop in the magnitude of the Curie transition temperature, T_c, from 450 K for samples with x ≤ 0.15 to 325 K for the samples with x > 0.15. The observed changes in the electronic and magnetic properties of $Fe_{1-x}Sn_xBi_2Se_4$ samples are rationalized within the framework of the formation of bound magnetic polarons (BMPs) through partial localization of charge carriers by the magnetic atoms, and the alteration of magnetic interactions between BMPs arising from the increased separation between magnetic centers in the crystal structure.

4.2 Results and Discussion

4.2.1 Structure

X-ray diffraction on polycrystalline powders of the synthesized $Fe_{1-x}Sn_xBi_2Se_4$ samples confirmed the formation of single phase as can be judged by the excellent agreement between the experimental XRD pattern and the theoretical pattern simulated from the single crystal data of the parent compound , $FeBi_2Se_4$ (Figure 2A and S1). The phase purity of the synthesized materials was confirmed further by differential scanning calorimetry (DSC) measurements (**Figure 4.3A** and **4.3B**), which showed a single endothermic peak of melting on the heating curves (**Figure 4.3A**) and a single exothermic peak of crystallization on the cooling curves (**Figure 4.3B**). This also suggests the chemical and structural stability of the synthesized $Fe_{1-x}Sn_xBi_2Se_4$ samples upon melting. A careful examination of the melting and crystallization peaks for various compositions indicates a marginal drop in the melting and crystallization temperatures upon increasing Sn

content from 937 K and 915 K for the sample with x = 0.10 to 931 K and 905 K for the sample

with x = 0.5. To better understand the effect of partial substitution of Fe by Sn on the functional

properties,   it   is   imperative
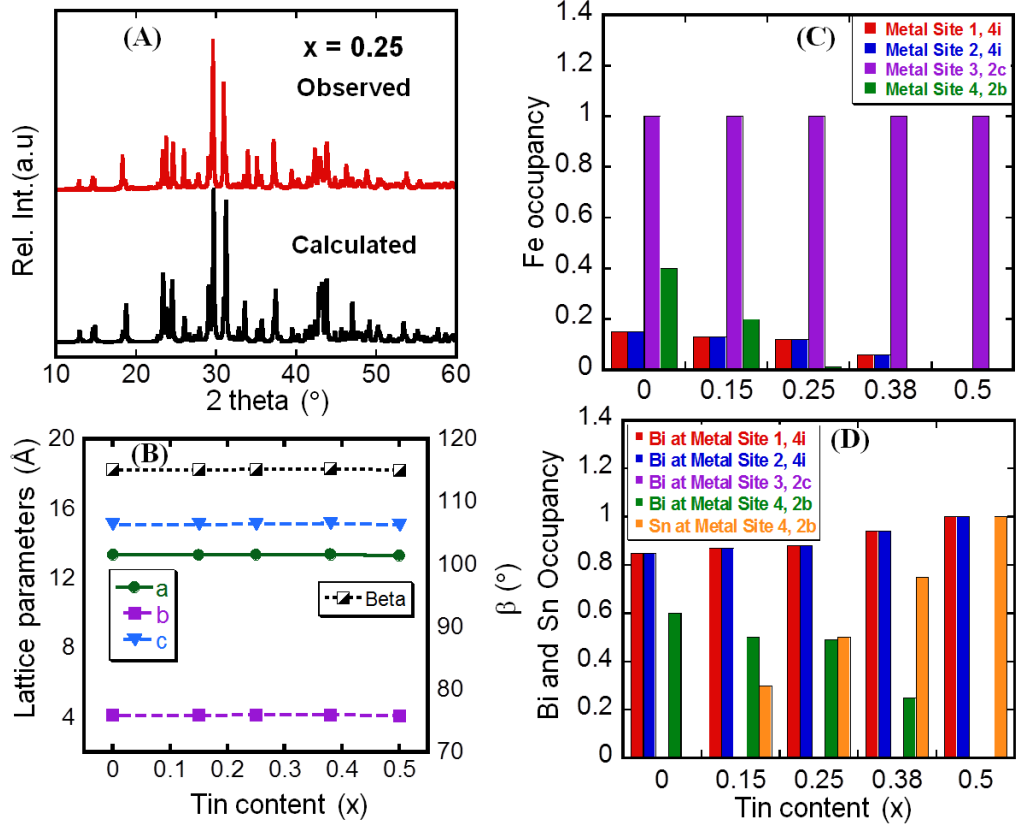
Figure 4. 2 Structural characterization of selected $Fe_{1-x}Sn_xBi_2Se_4$ compositions ($0 < x < 0.35$). (**A**) X-ray powder diffraction pattern of the sample with x = 0.25 compared to the theoretical pattern calculated using single crystal data from the parent compound (x = 0). (**B**) Variation of the lattice parameters as a function of Sn content obtained through refinement of single crystal X-ray diffraction data. Distribution of Fe (**C**) as well as Bi and Sn (**D**) at various metal positions M1, M2, M3 and M4 obtained from the refinement of single crystal X-ray diffraction data of samples with increasing Sn content (x values). For compositions with x ≤ 0.15, all four metal positions within the crystal structure contain various amounts of the magnetic atom, Fe. For compositions with 0.15 < x ≤ 0.38, no magnetic atom is found at the M4 site, increasing the distance between the magnetic subunits by two fold.

to fully characterize the distribution of metal atoms (Fe, Bi and Sn) at the four metal positions (M1(4i), M2(4i), M3(2c) and M4(2b)) within the monoclinic crystal lattice formed by the Se atoms. Therefore, single crystals of selected $Fe_{1-x}Sn_xBi_2Se_4$ compositions were grown by annealing the synthesized single phase powders at 913 K for 120 hours. The refinement of the single crystal diffraction data indicates a marginal alteration of the lattice parameters with increasing Sn content (**Figure 4.2B** and Table 4.1). This result is quite surprising given the large difference ($\Delta R/R = 68.5\%$) in the effective ionic radii of Fe^{2+} (70 pm) and Sn^{2+} (118 pm) in octahedral coordination.[29] The incorporation of Sn as Sn^{2+} in the crystal lattice of $Fe_{1-x}Sn_xBi_2Se_4$ phases was confirmed by X-ray photoelectron spectroscopy (XPS) analysis of selected compositions (**Figure 4.3C** and **4.3D**).

The XPS spectra for Sn_3d shell electrons for the compositions with x = 0.1 and 0.15 indicate Sn_3d$_{5/2}$ peak at binding energy ~ 486.4 eV, which is associated with Sn^{2+} in SnSe.[30] The intensity of the Sn_3d$_{5/2}$ peak increases with Sn content (Figure 3C), confirming an effective incorporation of Sn atoms within the $Fe_{1-x}Sn_xBi_2Se_4$ crystal lattice with a 2+ oxidation state. Likewise, the XPS spectra for both samples (x= 0.1 and 0.15) indicate the presence of Fe_2p$_{3/2}$ peak at binding energy of 711.3 eV, which is consistent with the binding energy associated with Fe^{2+} in FeO.[31-33] This implies that Fe maintains its 2+ oxidation state in $Fe_{1-x}Sn_xBi_2Se_4$ samples.

Remarkably, the refinement results also point to a rather interesting redistribution of metal atoms within the crystal structure. Except of the M3(2c) site, which is exclusively occupied by Fe atom in both the parent structure and the substituted compositions, the content of the remaining three metal positions is drastically altered by the partial substitution of Fe by Sn (Table 4.2 and **Figure 4.2C** and **4.2D**). In the parent compound ($FeBi_2Se_4$), mixed occupancy of Fe and Bi were

found at M1(85%Bi + 15%Fe), M2(85%Bi + 15%Fe) and M4(60%Bi + 40%Fe) sites. Upon substituting Fe by Sn, a preferential incorporation of Sn atoms at the M4 site was observed from the structure refinement leading to a significant change in the distribution of the Bi and the remaining Fe atoms within the M1, M2 an M4 sites. For instance, it was found that the substitution of 15% Fe by Sn
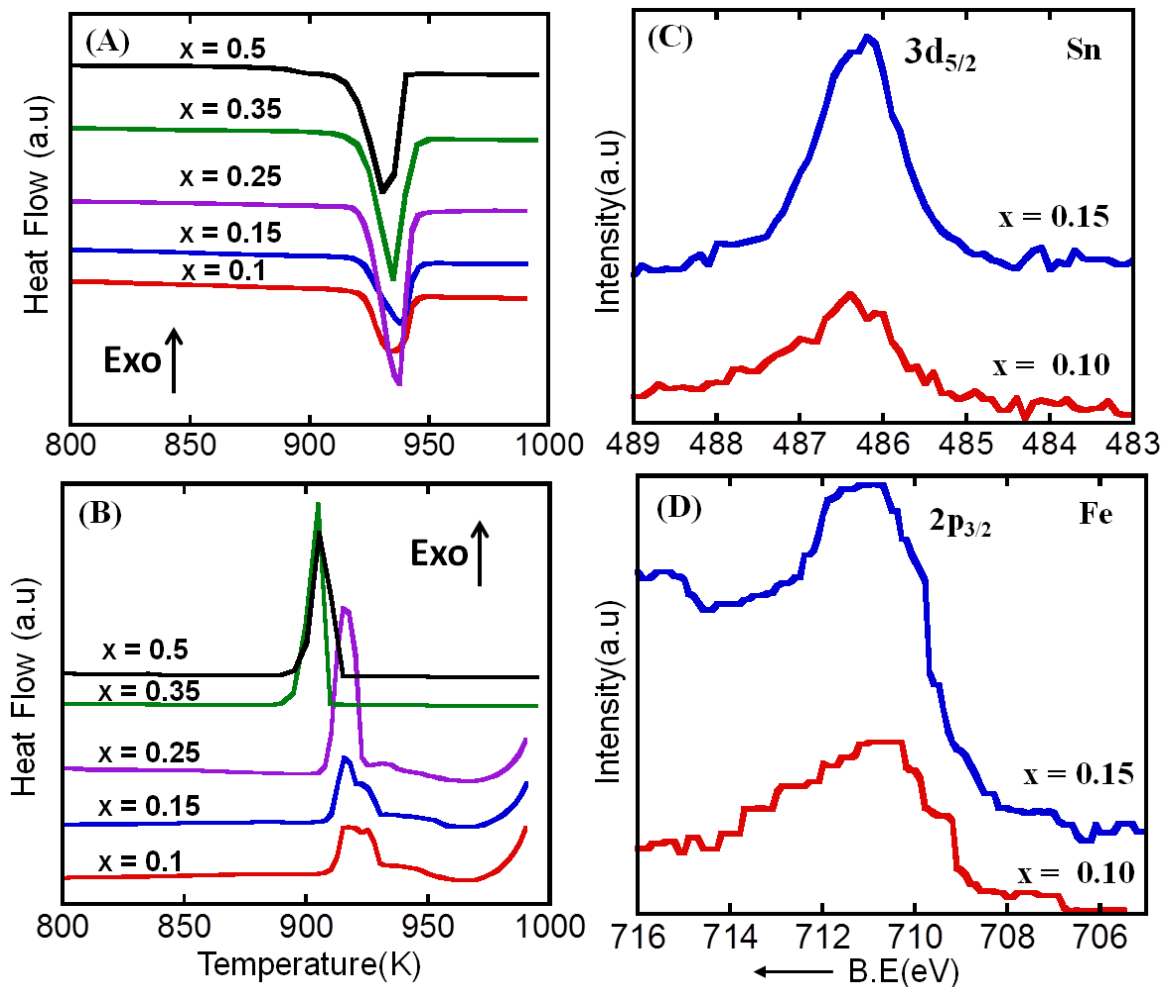
Figure 4. 3 (**A**) and (**B**) Thermal analysis of selected $Fe_{1-x}Sn_xBi_2Se_4$ samples using differential scanning calorimetric (DSC). The heating curves (**A**) reveal a single peak of melting between 937 K and the cooling curves (**B**) showed a crystallization peak at 915 K. (**C**) and (**D**) X-ray photoelectron spectroscopy spectra of Sn_5d (**C**) Fe_2p (**D**) shell electrons for selected $Fe_{1-x}Sn_xBi_2Se_4$ compositions.

(x = 0.15) leads to 30% occupancy of the M4 site by Sn. This changes the composition of the M1, M2 and M4 sites to M1(87%Bi + 13%Fe), M2(87%Bi + 13%Fe) and M4(50%Bi + 20%Fe+ 30%Sn). Increasing the Sn content to 25% (x = 0.25) leads to 50% occupancy of the M4 site by Sn. The composition of the M1, M2 and M4 sites changes to M1(88%Bi + 12%Fe), M2(88%Bi + 12%Fe) and M4(49%Bi + 1%Fe+ 50%Sn). At this point, the M4 site is nearly Fe-free, which significantly increases the separation between magnetic subunits from ~7.8 Å to ~ 15 Å (Figure 1). Further increasing the Sn content to x = 0.375 leads to the occupancy of 75% of the M4 site by Sn with the remaining 25% occupied by Bi atoms. Finally, substituting 50% of Fe by Sn (x = 0.5) leads to a fully ordered structure in which the M1 and M2 sites are fully occupied by Bi, whereas the M4 site is fully occupied by Sn (Table 4.2, **Figure 4.2C** and **4.2D**). This constant alteration of the chemical content of M1, M2 and M4 sites leads to various degrees of distortion of their coordination polyhedra (see Table 3 bond distances) in order to accommodate the large difference in the ionic radii of Fe^{2+} and Sn^{2+}. This explains the observed rather marginal alteration of the lattice parameters with the increasing Sn content. This alteration in the chemical composition and the distribution of the magnetic atom (Fe) and the non magnetic atoms (Bi and Sn) within the crystal structure of various compositions of the $Fe_{1-x}Sn_xBi_2Se_4$ series is anticipated to significantly change both their electronic and magnetic properties.

4.2.2 Electronic Properties

To probe the effect of partial substitution of Fe by Sn as well as the subsequent redistribution of metal atoms within the crystal structure on the electronic properties of the $Fe_{1-x}Sn_xBi_2Se_4$ series, Hall resistivity measurements were performed on selected samples in the temperature range from 2 K to 873 K (**Figure 4.4**). All samples showed negative Hall resistivity values (**Figure 4.4A** and

4.4C) in the whole measured temperature range, indicating that the *n*-type semiconducting character of the compound is maintained regardless of the degree of substitution. The temperature dependent carrier density at low temperatures (T ≤ 300 K) and at high temperatures (T ≥ 300 K) extracted from the Hall resistivity data showed some interesting trends. For instance, all samples showed a gradual decrease in the carrier density with temperature from 873 K down to ~100 K, below which a completely different behavior set in for various compositions. The observed gradual drop in the carrier density as the temperature decreases from 873 K down to 100 K, is consistent with the semiconducting behavior of the samples. However, a close examination of the temperature

dependent carrier density curves using Arrhenius equation $n \sim \exp(-E_a/k_B T)$, where k_B is the
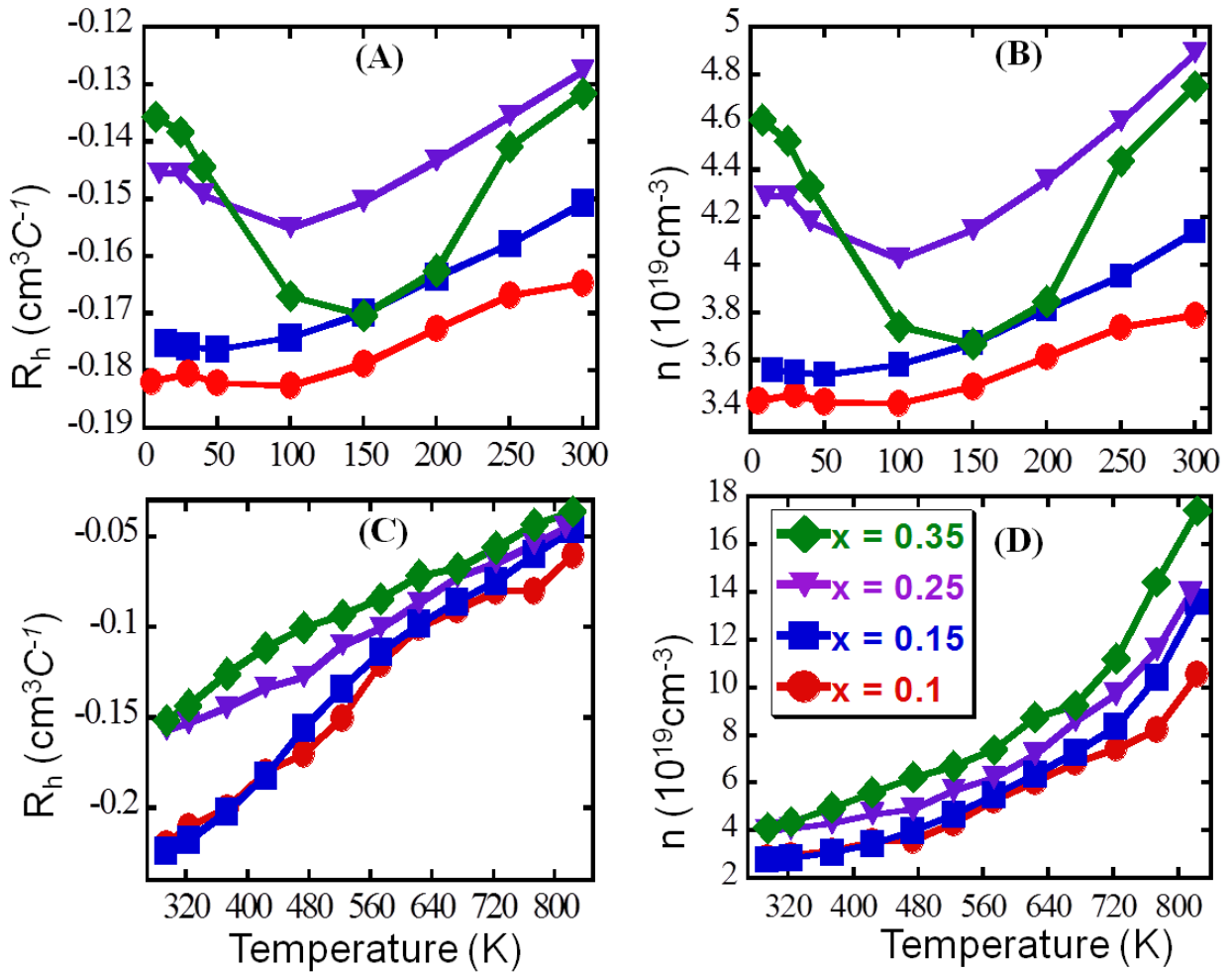
Figure 4. 4 Temperature dependence of the electronic properties of selected $Fe_{1-x}Sn_xBi_2Se_4$ samples. Low temperatures Hall coefficient (A) and carrier concentration (B) and high temperatures Hall coefficient (C) and carrier concentration (D). The samples with x = 0.25 and 0.35 showed an interesting upturn in the Hall coefficient and carrier concentration at ~ 87 K and 150 K, respectively.

Boltzmann constant, suggests significant variation in the activation energy, E_a, values for various compositions and temperature range.

In general, the temperature-dependent carrier density curves above 100 K can be divided into three portions with different values of the activation energy. The fitting of the portion of the data between 723 K and 823 K for various compositions leads to activation energy values ranging from $E_a \sim 0.25$ eV for compositions with $x \leq 0.15$ to $E_a \sim 0.2$ eV for the compositions with $0.25 \leq x \leq 0.35$. This portion of the curve is associated with the thermal activation of the. Therefore, we can conclude that the substitution of Fe by Sn forms various activation states and reduces various acceptor state from $E_g \sim 0.50$ eV (for compositions with $x \leq 0.15$) to $E_g \sim 0.4$ eV for the compositions with $0.25 \leq x \leq 0.35$. These small alterations in the electronic structure align with the increasing Sn content at a given temperature (**Figure 4.4B** and **4.4D**). The portion of the curve below 723 K within which extrinsic carriers dominate electrical conduction can be divided into two subsections with activation energy $E_a \sim 0.09$ eV (473 K $\leq$ T $\leq$ 723 K) and $E_a \sim 0.02$ eV (300 K $\leq$ T $\leq$ 473 K). This suggests the presence of impurities with various energy levels within the samples. The most interesting change in the electronic properties of $Fe_{1-x}Sn_xBi_2Se_4$ series of samples with increasing Sn content is observed for the portion of the curves below 100 K. For the sample with x = 0.1, the carrier density remains nearly constant in the temperature range from 100 K down to 2.8 K. Upon increasing the Sn content to x = 0.15, a weak increase in the carrier density is observed for temperatures below 50 K. The temperature of an upturn in the temperature-dependent carrier density increases to 100 K for the sample with x = 0.25 and finally to 150 K for the sample with x = 0.35 (**Figure 4.4B**). The observed drastic change (upturns) in the temperature dependent carrier density of $Fe_{1-x}Sn_xBi_2Se_4$ samples below 150 K is quite surprising and could be linked to alterations in the distribution of Fe and Sn at various metal positions within the crystal structure. As observed from the crystal structure refinement results (**Figure 4.2C** and **4.2D**), a mixed occupancy between the non magnetic atoms (Bi and Sn) and the magnetic atom (Fe) at the M4(2b) position is observed for compositions with $x \leq 0.15$. For compositions with higher Sn content ($x \geq 0.25$), no magnetic atom was found within the M4 site, which is exclusively occupied by the non magnetic Bi and Sn atoms. Such local change in the distribution of magnetic and non magnetic atoms within a given atomic lattice presumably leads to the alteration of the strength of

the exchange interaction between the spin of itinerant carriers and localized moment from the magnetic atom. For instance, the lack of intermixing at atomic level between itinerant carriers (Sn) and localized magnetic moment (Fe) for composition with x ≥ 0.25 weakens the localization of itinerant carriers in the vicinity of the magnetic transition due to the reduction in the magnetic coupling strength. This could explain the drastic change in the behavior of itinerant carriers observed in the vicinity of the magnetic transition, 83 K (Figure 6) for compositions with x ≥ 0.25 (**Figure 4.4B**).
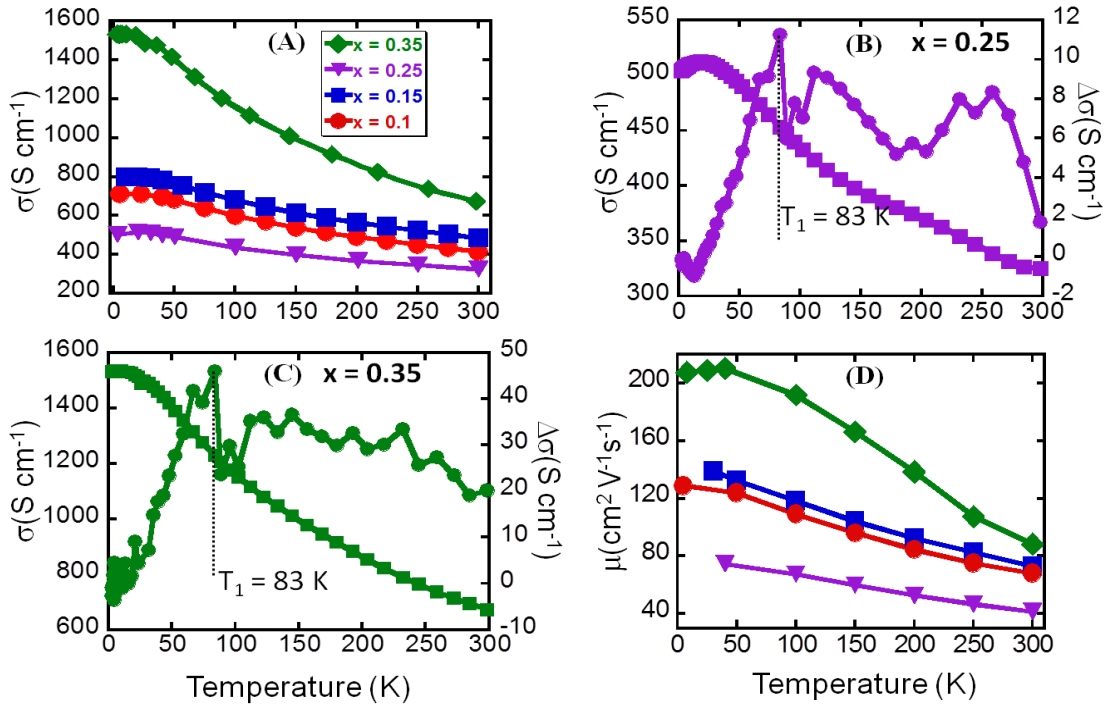
Figure 4. 5 Temperature dependent electrical conductivity (**A** to **C**) and carrier mobility (**D**) of selected $Fe_{1-x}Sn_xBi_2Se_4$ compositions. The discontinuity at 83 K on the $\Delta\sigma$ curves for x = 0.25 and x = 0.35 indicates a weakening of the temperature dependence electrical conductivity at lower temperatures.

To further explore the behavior of itinerant carriers in $Fe_{1-x}Sn_xBi_2Se_4$ samples at low temperatures, the electrical conductivity was measured in the temperature range from 300 K to 2.8 K (**Figure 4.5A**) and the temperature dependence of the carrier mobility (**Figure 4.5D**) was calculated using both the electrical conductivity and the carrier density data. Regardless of the composition, the electrical conductivity and the carrier mobility increase with decreasing

temperature (**Figure 4.5A**), which is consistent with a heavily doped semiconducting behavior. A close examination of the temperature-dependent electrical conductivity data for the samples with x = 0.25 (**Figure 4.5B**) and 0.35 (**Figure 4.5C**) showed a relatively fast increase in the electrical conductivity with decreasing temperature down to 83 K below which a slower increase in the electrical conductivity is observed with the further dropping temperature. The initial rapid increase in the electrical conductivity with decreasing temperature is consistent with the large increase in the carrier mobility (**Figure 4.5D**) arising from the reduced carrier density. However, the observed increase in the carrier density below 83 K for the samples with x = 0.25 and 0.35 leads to a slower increase in the carrier mobility, which explains the weaker temperature dependence of the electrical conductivity below 83 K. Regardless of the temperature, the electrical conductivity and carrier density of various of $Fe_{1-x}Sn_xBi_2Se_4$ samples initially remain nearly constant for compositions with x = 0.1 and 0.15, then suddenly drop upon increasing the Sn content to x = 0.25 and finally increase by over 50% with a yet further increase in the Sn content to x = 0.35. For example, the electrical conductivity and carrier mobility at 300 K is, respectively, ~400 S cm^{-1} and 60 cm^{2}V^{-1}s^{-1}, and rapidly increase to ~800 S cm^{-1} and 120 cm^{2}V^{-1}s^{-1} at 2 K for the samples with x = 0.1 and 0.15. Upon increasing the Sn content to x = 0.15, both the electrical conductivity and carrier mobility drop, respectively, to 300 S cm^{-1} and 40 cm^{2}V^{-1}s^{-1} at 300 K and to ~500 S cm^{-1} and 70 cm^{2}V^{-1}s^{-1} at 2 K. The observed large drop in the carrier mobility with the increasing content of Sn to x = 0.25 maybe due in part to the large increase (>100% increase) in the carrier concentration (Figure 4B), but also to the nearly equal intermixing at the M4 site of low mobility carriers from Bi atoms and higher mobility charge carriers from Sn atoms. Upon increasing the Sn content to x = 0.35, the largest fraction of the M4 site is occupied by Sn atoms, which leads to a large increase in the overall carrier mobility and electrical conductivity, respectively, to 90 cm^{2}V^{-}

^{1}s^{-1} and 700 S cm^{-1} and at 300 K, and to 200 cm^{2}V^{-1}s^{-1} and ~1500 S cm^{-1} and at 2 K. The above analysis strongly indicates that despite the isoelectronic nature of substitution of Fe^{2+} by Sn^{2+} in the structure of Fe$_{1-x}$Sn$_x$Bi$_2$Se$_4$, samples the overall electronic transport properties are strongly influenced by the subsequent distribution of non-magnetic (Bi, Sn) and magnetic (Fe) atoms at various metal positions within the crystal lattice.

4.2.3 Magnetic Properties

To probe the effects of the substitution of Fe by Sn on the magnetic behavior of Fe$_{1-x}$Sn$_x$Bi$_2$Se$_4$ samples, temperature-dependent magnetic susceptibility data at low temperatures (**Figure 4.6**) and at high temperatures (**Figure 4.7**) were collected on selected compositions using a SQUID magnetometer. Low temperature field-cooled (FC) and zero-field cooled (ZFC) magnetic susceptibility data were measured under 100 Oe applied magnetic field (**Figure 4.6**) in the temperature range from 2 K to 300 K. All samples show ferromagnetic behavior up to 300 K. The FC susceptibility of samples with x ≤ 0.25 slowly increases with the decreasing temperature down to ~ 110 K below which a sudden drop in the susceptibility is observed (**Figure 4.6A** and **4.6B**). Further cooling the samples (x ≤ 0.25) below the magnetic transition resulted in a marginal increase in the FC susceptibility. For example, the FC magnetic susceptibility for the sample with x = 0.1 is 0.012 μB F.U.$^{-1}$at 300 K and increases slowly to 0.016 μB F.U.$^{-1}$ at 110 K, then suddenly drops to 0.14 μB F.U.$^{-1}$ at 95 K and remains nearly constant down to 5 K. A similar trend was observed for samples with x = 0.15 and 0.25. The magnetic transition observed at 110 K is a typical behavior found in FePn$_2$Se$_4$-based (Pn = Sb or Bi) phases, and the sudden drop in the magnetic susceptibility is believed to be related to a local structural distortion within the magnetic sub-lattice

[FeSe$_6$] upon cooling , which leads to the spin redistribution within the d-orbitals of Fe atom.[21,22,24,25] It is interesting to note that the magnetic transition around 110 K completely vanishes from the FC susceptibility upon increasing the Sn content to x = 0.35 and x = 0.5 (**Figure 4.6A**). For these two samples, a monotonic increase in FC susceptibility upon cooling from 300 K to 5 K is observed, which is a typical behavior for materials with ferromagnetic-like character. The FC magnetic susceptibility increases from 0.009 µB F.U.$^{-1}$ and 0.003 µB F.U.$^{-1}$ at 300 K to 0.045 µB F.U.$^{-1}$ and 0.02 µB F.U.$^{-1}$ at 5 K

Figure 4. 6 Low temperature magnetic susceptibility curves of selected Fe$_{1-x}$Sn$_x$Bi$_2$Se$_4$ samples under field-cooled (FC) (**A** and **B**) and zero-field-cooled (ZFC) (**C** and **D**) conditions using an external applied field of 100 Oe. For the composition with x = 0.5, the magnetic transition near 110 K vanishes from both FC and ZFC curves.

for the samples with x = 0.35 and x = 0.5, respectively. Regardless of the temperature, the magnitude of the FC susceptibility initially drops upon increasing the Sn content from x = 0.1 to x = 0.15, then increases with a further increase in Sn content, reaching maximum values for the composition with x = 0.35. Further increasing the Sn content to x = 0.5 led to a large drop in the FC susceptibility. A similar trend was observed for the temperature-dependent ZFC susceptibility of $Fe_{1-x}Sn_xBi_2Se_4$ samples. Regardless of the temperature, the ZFC susceptibility value decreases with the increasing Sn content for the compositions with x ≤ 0.15, then increases with the increasing Sn content for composition with 0.25 ≤ x ≤ 0.35, and finally decreases again for the composition with x = 0.5. In addition, the magnetic transition within the temperature range from 110 K to 83 K is also observed on the temperature-dependent ZFC susceptibility of various samples, except the composition with x = 0.5, which shows a maximum ZFC susceptibility at 240 K followed by a gradual decrease in the ZFC susceptibility upon further cooling (Figure 6 C and 6D).

The observed non-monotonic variation in the magnitude of FC and ZFC susceptibility upon increasing Sn content as well as the disappearance of the magnetic transition at 100 K for compositions with x > 0.35 suggests that the magnetic behavior of $Fe_{1-x}Sn_xBi_2Se_4$ samples is strongly linked to the separation between the magnetic centers (Fe atom) within the crystal structure. As shown in Figure 2C, the distribution of Fe atoms at various metal sites is drastically altered by the degree of substitution of Fe by Sn atoms.

For compositions with x ≤ 0.15, Fe atoms are found at all metal positions and the distance between magnetic centers is essentially constant. Therefore, the drop in the magnetic susceptibility with increasing Sn content (x ≤ 0.15) can be attributed to an increase in the overall magnetic

moment within the layer-B. This is due to the fact that the incorporation of Sn atom within the M4
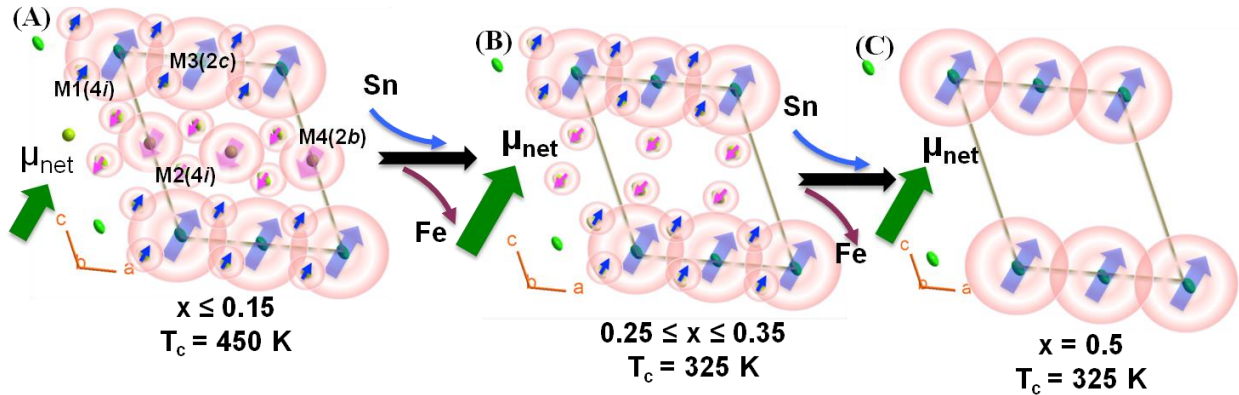
Figure 4. 7 Schematic illustration of the alteration of magnetic exchange interactions in $Fe_{1-x}Sn_xBi_2Se_4$ samples with increasing Sn content. (**A**) For compositions with $x \leq 0.15$, the largest fraction of Fe atoms is located at M3 and M4 sites with a small fraction of Fe at M1 and M2 sites. Bound magnetic polarons (BMPs) centered on M3 site (layer-A) and M4 site (layer-B) are antiferromagnetically coupled. Increasing Sn content within the M4 site strengthened the BMPs within layer-B leading to a decrease in the overall magnetic moment. (**B**) and (**C**) For compositions with $x \geq 0.25$, the M4 site is Fe-free and the concentration of Fe at M1 and M2 sites decreases with increasing Sn content. This leads to an increase in the overall moment and decrease in T_c due to increase separation between magnetic centers.

site increases the concentration of delocalized carriers leading to the formation of larger magnetic polarons through exchange interaction with the magnetic atom at the M4 site. Since magnetic moments within layer–B are coupled anti-ferromagnetically to moments within layer-A,[24] the overall moment of the compound will decrease as the moment within layer-B increases (**Figure 4.7A**). It should be noted that the concentration of Fe within the M4(2b) site also decreases with the increasing Sn content. This leads to a complete substitution of Fe at the M4 site for compositions with $x \geq 0$ .25 (**Figure 4.2C**). Therefore, the only magnetic centers within the structure having compositions with $0.25 \leq x \leq 0.35$ are the M1(4i), M2(4i) and M3(2c) sites (**Figure 4.7B**). Within this composition range, the substitution of Fe by Sn increases the fraction

of delocalized free-carriers, which leads to a enhanced overlap of bound magnetic polarons (BMPs) within layer-A. This explains the observed increase in the overall susceptibility for compositions $0.25 \leq x \leq 0.35$, despite the decrease in the Fe content and a gradual removal of Fe atoms from the M1 and M2 sites. For the composition with $x = 0.5$, $Fe_{0.5}Sn_{0.5}Bi_2Se_4$, the only magnetic center in the crystal structure is the M3(2c) site within layer-A (**Figure 4.7C**). This significantly increases the distance between adjacent magnetic layers (layer-A) to ~ 15 Å. Therefore, the drop in both the FC and ZFC magnetic susceptibly values observed for this composition ($x = 0.5$), compared to the sample with $x = 0.35$, can be associated with the lack of overlap between magnetic polarons on adjacent layer-A.

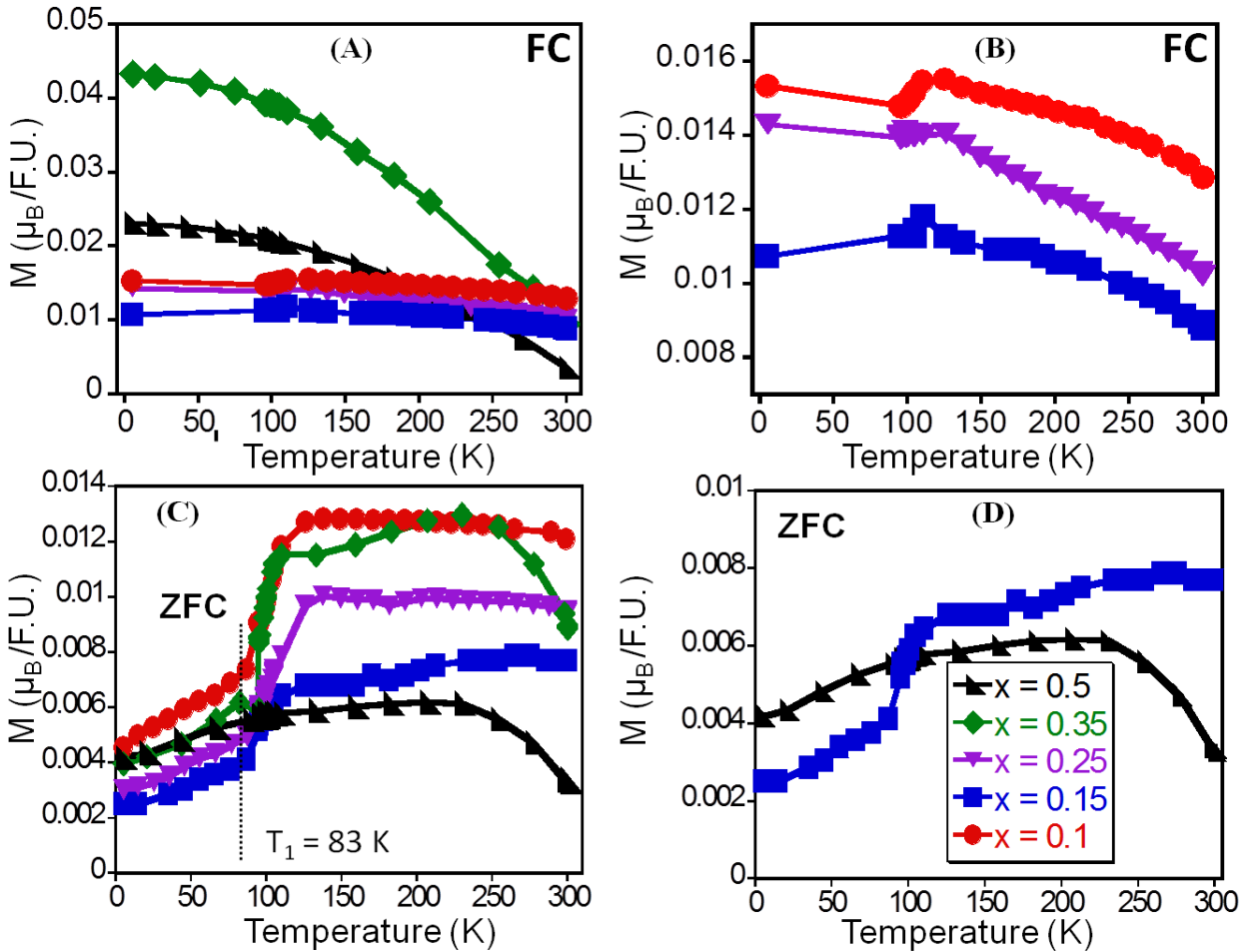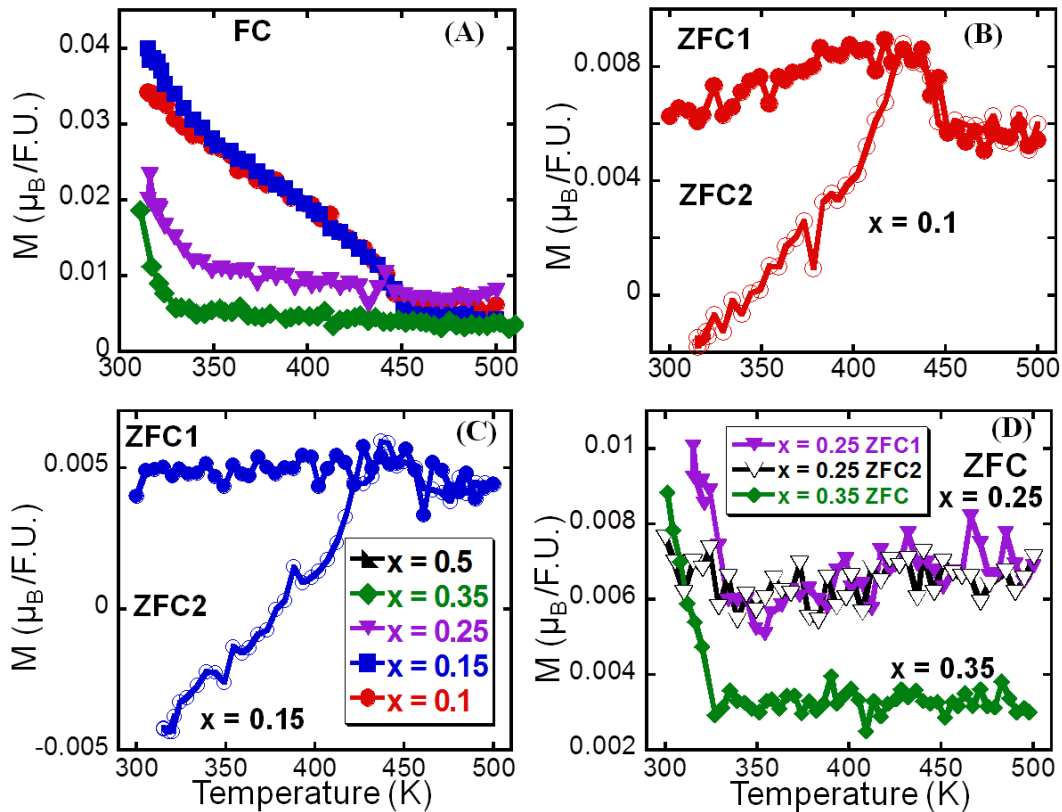**Figure 4. 8** High temperature magnetic susceptibility curves of selected $Fe_{1-x}Sn_xBi_2Se_4$ samples under field-cooled (FC) (**A**) and zero-field-cooled (ZFC) (**B** to **D**) using an external applied field of 100 Oe. A drastic drop in T_c from 450 K to 325 K is observed upon increasing Sn content above 25% ($x \geq 0.25$). Samples with highest Tc ($x \leq 0.15$) showed negative magnetization on the second ZFC curves (ZFC2).

To further probe the effect of the substitution of Fe by Sn and the resulting redistribution of atoms with the crystal lattice, on the Curie temperature, T_c, high temperature FC and ZFC magnetic susceptibilities were measured in the temperature range from 300 K to 500 K (**Figure 4.8**) under an applied external magnetic field of 100 Oe. ZFC susceptibility data (ZFC1) was measured upon warming the samples from 300 K to 500 K. The samples were subsequently cooled to 300 K while the applied magnetic field was still on and FC susceptibility data was collected by reheating the samples to 500 K. At this point, the external magnetic field was turned off and the samples were cooled to 300 K under zero-applied magnetic field. A second set of ZFC susceptibility data (ZFC2) was collected upon heating from 300 K to 500 K under an applied external magnetic field of 100 Oe. The first ZFC susceptibility curves (ZFC1) for samples with x ≤ 0.15 slightly increased with temperature up to ~ 450 K where an abrupt drop in the susceptibility was observed. The susceptibility remained nearly constant as the temperature increased further beyond 450 K. The slight increase in the magnitude of the ZFC susceptibility between 300 K and 450 K can be associated with an improved alignments of canted magnetic moments of bound magnetic polarons (BMPs) facilitated by thermal activation and the applied external magnetic field. The drop in the magnetic susceptibility beyond 450 K is attributed to the Curie transition into the superparamagnetic regime where long range magnetic coupling between BMPs is lost. During cooling under applied magnetic field, a larger fraction of moments from BMPs are aligned with respect to the applied field, which explains the larger values of the FC magnetic susceptibility for samples with x = 0.1 and 0.15. Surprisingly, the second ZFC curves (ZFC2) for both samples, measured after cooling the samples from 500 K to 300 K in the absence of external magnetic field, showed negative susceptibility values at 300 K (-0.002 μB F.U.$^{-1}$ for x = 0.1, and ~ -0.0045 μB

F.U.$^{-1}$ for x = 0.15). The susceptibility subsequently increased rapidly with the rising temperature, crossing into positive values at T_{cross} = 350 K and 377 K for the samples with x = 0.1 and 0.15, respectively, and continued increasing to temperatures around 420 K where both ZFC1 and ZFC2 curves merged (**Figure 4.8B** and **4.8C**). One possible origin of the negative susceptibility values observed for the samples with x = 0.1 and 0.15 is that the ordering of randomized moments upon cooling from 500 K to 300 K under zero-applied magnetic field leads to non-zero overall moment with the direction opposite to that of the external magnetic field. Such non-zero overall moment could be the result of AFM coupling between BMPs from layer-A and layer-B (**Figure 4.7A**). Upon increasing the Sn content to $0.25 \leq x \leq 0.5$, both ZFC1 and ZFC2 susceptibility curves show very similar trend and the Curie temperature drastically dropped to 325 K (**Figure 4.8A**, **4.8D**). The absence of negative magnetic susceptibility for the ZFC2 curve of the samples with $0.25 \leq x \leq 0.5$ could be associated with the absence of the AFM contribution from layer-B, whereas the drop in the T_c to 325 K is attributed to an increase in the average distance between adjacent magnetic centers (Figure 4.7B) due to the complete absence of Fe from the M4(2*b*) site.

One can observe from the above results that while the Curie temperature, T_c, of $Fe_{1-x}Sn_xBi_2Se_4$ samples decreases with the decreasing Fe content, this interdependence is not monotonic. Starting from the parent phase, $FeBi_2Se_4$,[25] which showed a T_c of 450 K, the substitution of Fe by the non magnetic Sn atoms up to x = 0.15 does not result is a drop in T_c. This is likely due to the similarity in the distribution of the remaining Fe atoms within various metal positions. Indeed, Fe atoms in the compositions with $0 \leq x \leq 0.15$ are found in all four metal positions, M1, M2, M3 and M4, although with various occupancy factors (**Figure 4.2C**). Therefore, the distance between magnetic centers (Fe atom) is relatively short and remains essentially the same in all these samples ($0 \leq x \leq 0.15$). This leads to a greater overlap between

neighboring BMPs, which mediates long-range ferromagnetism through the localized carrier clouds surrounding various magnetic centers (**Figure 4.7A**). This overlap between BMPs is likely the origin of the observed robust $T_c \sim 450$ K. As the Sn content reaches $x = 0.25$, the concentration of the Fe atoms at the M4 position is nearly zero. This increases the average distance between magnetic centers (Fe atoms) in the crystal (**Figure 4.7B**), leading to a weaker overlap between BMPs mediating long-range magnetism. As a result, a reduction in the T_c down to 325 K is observed for the sample with $x = 0.25$. Further increasing the concentration of Sn up to $x = 0.5$ did not lead to further drop in T_c. It can be concluded from the above analysis that large separation between magnetic centers rather than the decrease in the concentration of magnetic atoms (Fe) is responsible for the large drop in the T_c of $Fe_{1-x}Sn_xBi_2Se_4$ samples. This is a very important result, which settles the debate regarding the correlation between the concentration of magnetic atoms,

the separation between magnetic centers, and the T_c in diluted magnetic semiconductors (DMS).[2,34-38]
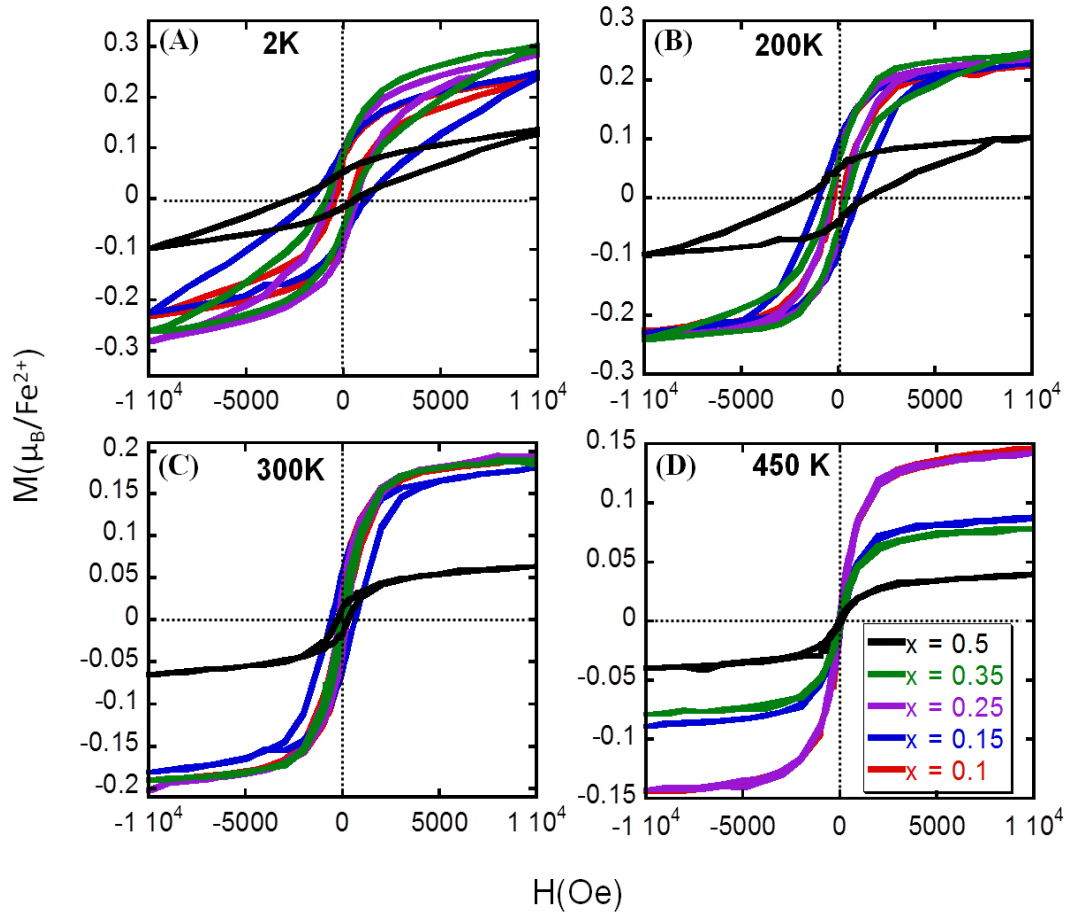
Figure 4. 9 Isothermal field dependent magnetization of selected of selected $Fe_{1-x}Sn_xBi_2Se_4$ samples collected at 2 K (**A**); 200 K (**B**); 300 K (**C**); and 450 K (**D**) showing large hysteresis up to 300 K.

The ferromagnetic-like character of various $Fe_{1-x}Sn_xBi_2Se_4$ samples was further confirmed by isothermal magnetization measurements at various temperatures between 2 K and 450 K under applied magnetic field sweeping from -10 kOe to + 10 kOe (**Figure 4.9**).The M-H curves for all samples display the characteristic S-shape hysteresis loop expected for ferromagnetic materials. At 2K, the saturation magnetization remains nearly constant at 0.3 μB Fe^{-1} for samples with x $\leq$

0.35 and drops to 0.15 μB Fe^{-1} for the sample with x = 0.5. This trend further indicates a large contribution from carrier spins to the overall magnetic moment, which helps to sustain strong ferromagnetism within the compounds even though the magnetic ion concentration is decreasing. The coercive field at 2K initially increases with the Fe content from ~ 450 Oe for the sample with x = 0.1 to 1650 Oe for the sample with x = 0.15. The Wasp-waisted-like hysteresis loop observed at 2K for the sample with x = 0.15 suggests the presence of competing AFM and FM alignments of net spins with the application of the external magnetic field. Interestingly, this Wasp-waisted hysteresis loop vanishes upon increasing the temperature to 200 K and 300 K. Further increase in the Sn content leads to a drop in the coercivity to ~830 Oe for the samples with x = 035. The largest coercivity field value, 2500 Oe, is obtained for the sample with x = 0.5 upon application of negative magnetic field. The saturation magnetization (M_s) and the coercive field (H_c) of various samples decrease with the increasing temperature up to the Curie temperature, T_c (**Figure 4.9B** and **4.9C**). Further increase in the temperature beyond T_c leads to superparamagnetic behavior, which is manifested by S-shape curves with little or no coercivity (Figure 9D).

4.3 Conclusion

We have systematically investigated the effect of isoelectronic substitution of the magnetic Fe atom by the non-magnetic Sn atoms on the magnetic behavior and electronic properties of the n-type ferromagnetic semiconductor with compositions $Fe_{1-x}Sn_xBi_2Se_4$ ($0 \leq x \leq 0.5$). We found that despite the large difference in the effective ionic radii of Fe^{2+} and Sn^{2+}, the lattice parameters remains essentially unaffected by the incorporation of Sn atom within the crystal lattice of $FeBi_2Se_4$. This surprising result is rationalized through careful analysis of the distribution of metal atoms (Fe, Sn, Bi) within various metal positions in the $FeBi_2Se_4$ structure. Unlike a true solid-

solution in which the substituting atom is anticipated to occupy the same atomic position left vacant by the substituted atom leading to a linear change in the lattice parameter with composition, the incorporation of Sn into the $FeBi_2Se_4$ structure triggers an interesting atomic re-arrangement, where the Sn atom preferentially enters the M4 site leading to a new distribution of Bi and the remaining Fe atoms within the M1, M2 and M3 sites. This change in the distribution of metal atoms within the lattice upon altering the Sn content leads to various degrees of distortions (compression or extension) of local bond distances and angles, which explains the overall marginal alteration in the lattice parameters. The new redistribution of the magnetic atoms (Fe atoms) within the structure for various amounts of Sn incorporated leads to very interesting magnetic behavior. While all samples display ferromagnetic behavior at temperature above 300 K, a large drop in the Curie temperature from 450 K to 325 K is observed for samples with $0 \leq x \leq 0.15$ and $0.25 \leq x \leq 0.5$, respectively. The non-monotonic change in the T_c with the increasing Sn content leads to the conclusion that the drop in T_c is due to the change in the separation between magnetic centers, rather than the decrease in the concentration of magnetic ions. All samples show *n*-type semiconducting behavior with a marginal increase in the carrier density as the Sn content increase. However, careful analysis of the temperature dependence of the carrier density reveals that the slight increase in the carrier density with Sn content at a given temperature is associated with a slight decrease in the bandgap, rather than an additional doping by Sn atoms. These results are signatures of a selective control over the magnetic properties in $Fe_{1-x}Sn_xBi_2Se_4$ samples with minimal effect on the semiconducting properties.

Table 4. 1 Selected crystallographic data for $Fe_{1-x}Sn_xBi_2Se_4$ compositions with x = 0.15, 0.25, 0.375, and 0.5.

Sn content (x)	x = 0.15	x = 0.25	x = 0.375	x = 0.50
CCDC number	1899030	1899029	1899028	1899027
Crystal system; space group; Z	Monoclinic; $C2/m$ (#12); 4			
Formula weight (g/mol)	799.08	805.36	813.21	821.07
Density Calc. (g/cm^3)	7.09(1)	7.12(1)	7.16(1)	7.32(1)
Lattice parameters (Å)				
a	13.320(2)	13.346(2)	13.368(2)	13.300(2)
b	4.1162(4)	4.1207(6)	4.1208(5)	4.1035(4)
c	15.061(2)	15.092(2)	15.134(2)	15.058(2)
β (°)	115.04(1)	115.10(1)	115.22(1)	115.00(1)
Volume (Å^3)	748.12(3)	751.56(4)	754.23(4)	744.79(3)
Diffractometer; Radiation	IPDS-2T(Stoe); $\lambda(MoK_a) = 0.71073$ Å			
μ (cm^{-1})	684	682	681.5	692
$2\theta_{max}$ (°); index range	65; $-20 \le h \le 20$, $-6 \le k \le 6$, $-22 \le l \le 22$	58; $-18 \le h \le 18$, $-5 \le k \le 5$, $-20 \le l \le 20$	66; $-20 \le h \le 17$; $-6 \le k \le 6$; $-23 \le l \le 23$	58; $-18 \le h \le 18$, $-5 \le k \le 5$, $-20 \le l \le 20$
Diff. elec. density [eÅ^{-3}]	+4.00 to -5.42	+3.35 to -1.70	+4.05 to -2.48	+4.18 to -3.28
R_1 ($F_o>4\sigma(F_o)$)[a]	0.048	0.037	0.048	0.057
wR_2 (all) [b]	0.120	0.070	0.124	0.144
GooF	1.04	1.14	1.08	1.11

[a] $R_1 = \Sigma||F_o|-|F_c||/\Sigma|F_o|$; [b] $wR_2 = [\Sigma w(F_o^2-F_c^2)^2/\Sigma w(F_o^2)^2]^{1/2}$

Table 4. 2 Wyckoff positions (W.P.), site occupancy factors (k), atomic coordinates, and equivalent isotropic displacement parameters ($U_{eq}/10^{-4}$ x Å^2) for all atoms in the asymmetric unit of $Fe_{1-x}Sn_xBi_2Se_4$ compositions. The first, second, third and fourth row corresponds to x = 0.15, 0.25, 0.38, and 0.5, respectively.

Atom	W.P.	k	x	y	z	U_{eq}
Bi1/Fe1	4i	0.87/0.13	0.2177(1)	0	0.3626(1)	295(2)
		0.88/0.12	0.2174(1)	0	0.3622(1)	233(2)
		0.94/0.06	0.2174(1)	0	0.3621(1)	393(2)
		1.0/0.0	0.2176(1)	0	0.3626(1)	277(4)
Bi2/Fe2	4i	0.87/0.13	0.3495(1)	1/2	0.1363(1)	259(2)
		0.88/0.12	0.3498(1)	1/2	0.1364(1)	178(2)
		0.94/0.06	0.3501(1)	1/2	0.1357(1)	338(2)
		1.0/0.0	0.3493(1)	1/2	0.1349(1)	257(4)
Fe3	2c	1.0	1/2	1/2	1/2	314(7)
		1.0	1/2	1/2	1/2	181(6)
		1.0	1/2	1/2	1/2	312(6)
		1.0	1/2	1/2	1/2	269(3)
Bi4/Fe4/Sn4	2b	0.5/0.2/0.3	1/2	0	0	235(3)
		0.49/0.01/0.5	1/2	0	0	167(3)
		0.25/0.0/0.75	1/2	0	0	257(3)
		0.0/0.0/1.0	1/2	0	0	106(4)
Se1	4i	1.0	0.5095(2)	0	0.1917(2)	316(4)
		1.0	0.5096(2)	0	0.1926(2)	231(4)

		1.0	0.5101(2)	0	0.1916(2)	370(4)
		1.0	0.5100(2)	0	0.1894(2)	282(6)
Se2	4i	1.0	0.1130(2)	1/2	0.4559(1)	243(3)
		1.0	0.1135(2)	1/2	0.4565(2)	176(3)
		1.0	0.1131(2)	1/2	0.4566(2)	308(4)
		1.0	0.1128(2)	1/2	0.4558(2)	192(5)
Se3	4i	1.0	0.3468(2)	1/2	0.3298(1)	249(3)
		1.0	0.3456(2)	1/2	0.3292(2)	189(3)
		1.0	0.3453(2)	1/2	0.3286(2)	320(3)
		1.0	0.3467(2)	1/2	0.3297(2)	196(5)
Se4	4i	1.0	0.1625(2)	0	0.0660(2)	265(3)
		1.0	0.1635(2)	0	0.0661(2)	186(3)
		1.0	0.1630(2)	0	0.0655(2)	322(4)
		1.0	0.1613(2)	0	0.0651(2)	229(5)

U_{eq} is defined as one-third of the trace of the orthogonalized U_{ij} tensor

Table 4. 3 Selected inter-atomic distances (Å) in Fe1-xSnxBiSe4 compositions with x = 0.15, 0.25, 0.38, and 0.5 [a]

Bond Type	x = 0.15	x = 0.25	x = 0.38	x = 0.5
Bi1|Fe1—Se2[i]	2.709(2)	2.710(2)	2.715(2)	2.711(2)
Bi1|Fe1—Se3	2.856(2)	2.854(2)	2.857(2)	2.850(2)
Bi1|Fe1—Se3[ii]	2.856(2)	2.854(2)	2.857(2)	2.850(2)
Bi1|Fe1—Se2	3.133(2)	3.141(2)	3.152(2)	3.127(2)
Bi1|Fe1—Se2[ii]	3.133(2)	3.142(2)	3.152(2)	3.127(2)

Bi1|Fe1—Se1^{iii}	3.537(2)	3.529(2)	3.534(2)	3.542(2)
Bi1|Fe1—Se1^{iv}	3.537(2)	3.533(2)	3.534(2)	3.542(2)
Bi2|Fe2—Se1^{v}	2.823(2)	2.823(2)	2.828(2)	2.823(2)
Bi2|Fe2—Se1	2.823(2)	2.825(2)	2.828(2)	2.823(2)
Bi2|Fe2—Se3	2.930(2)	2.934(2)	2.947(2)	2.949(2)
Bi2|Fe2—Se4^{vi}	2.983(2)	2.985(2)	2.975(2)	2.954(2)
Bi2|Fe2—Se4	3.055(2)	3.051(2)	3.061(2)	3.057(2)
Bi2|Fe2—Se4^{v}	3.055(2)	3.054(2)	3.061(2)	3.057(2)
Fe3—Se3^{vii}	2.512(2)	2.527(2)	2.537(2)	2.513(2)
Fe3—Se3	2.512(2)	2.527(2)	2.537(2)	2.513(2)
Fe3—Se2^{i}	2.791(2)	2.795(2)	2.794(2)	2.783(2)
Fe3—Se2^{viii}	2.791(2)	2.795(2)	2.794(2)	2.783(2)
Fe3—Se2^{ix}	2.791(2)	2.795(2)	2.794(2)	2.783(2)
Fe3—Se2^{x}	2.791(2)	2.795(2)	2.794(2)	2.783(2)
Bi4|Sn4|Fe4—Se1	2.836(2)	2.855(2)	2.845(2)	2.799(3)
Bi4|Sn4|Fe4—Se1^{xi}	2.836(2)	2.854(2)	2.845(2)	2.799(3)
Bi4|Sn4|Fe4—Se4^{xii}	2.844(2)	2.855(2)	2.852(1)	2.828(2)
Bi4|Sn4|Fe4—Se4^{ix}	2.844(2)	2.857(2)	2.852(1)	2.828(2)
Bi4|Sn4|Fe4—Se4^{vi}	2.844(2)	2.857(2)	2.852(1)	2.828(2)
Bi4|Sn4|Fe4—Se4^{x}	2.844(2)	2.854(2)	2.852(1)	2.828(2)

Operators for generating equivalent atoms: (i) $1/2-x$, $1/2-y$, $1-z$; (ii) x, $y-1$, z; (iii) $x-1/2$, $y-1/2$, z; (iv) $x-1/2$, $1/2+y$, z; (v) x, $1+y$, z; (vi) $1/2-x$, $1/2-y$, $-z$; (vii) $1-x$, $1-y$, $1-z$; (viii) $1/2+x$, $1/2+y$,

z; (ix) 1/2+*x*, *y*−1/2, *z*; (x) 1/2−*x*, 1/2−*y*, 1−*z*; (xi) 1−x, −*y*, −*z*; (xii) 1/2−*x*, −1/2−*y*, −*z*; (xiii) −*x*, −*y*, −*z*.

4.4 References

(1)   Dery, H.; Dalal, P.; Cywinski, L.; Sham, L. J. Spin-based logic in semiconductors for reconfigurable large-scale circuits *Nature* **2007**, *447*, 573.

(2)   Ando, K. Seeking room-temperature ferromagnetic semiconductors *Science* **2006**, *312*, 1883.

(3)   Wolf, S. A.; Awschalom, D. D.; Buhrman, R. A.; Daughton, J. M.; von Molnar, S.; Roukes, M. L.; Chtchelkanova, A. Y.; Treger, D. M. Spintronics: A spin-based electronics vision for the future *Science* **2001**, *294*, 1488.

(4)   Ohno, H.; Munekata, H.; Penney, T.; Vonmolnar, S.; Chang, L. L. Magnetotransport Properties of P-Type (in,Mn)as Diluted Magnetic Iii-V Semiconductors *Phys Rev Lett* **1992**, *68*, 2664.

(5)   Ohno, H.; Shen, A.; Matsukura, F.; Oiwa, A.; Endo, A.; Katsumoto, S.; Iye, Y. (Ga,Mn)As: A new diluted magnetic semiconductor based on GaAs *Appl Phys Lett* **1996**, *69*, 363.

(6)   VanEsch, A.; VanBockstal, L.; DeBoeck, J.; Verbanck, G.; vanSteenbergen, A. S.; Wellmann, P. J.; Grietens, B.; Bogaerts, R.; Herlach, F.; Borghs, G. Interplay between the magnetic and transport properties in the III-V diluted magnetic semiconductor Ga1-xMnxAs *Phys Rev B* **1997**, *56*, 13103.

(7)   Haury, A.; Wasiela, A.; Arnoult, A.; Cibert, J.; Tatarenko, S.; Dietl, T.; dAubigne, Y. M. Observation of a ferromagnetic transition induced by two-dimensional hole gas in modulation-doped CdMnTe quantum wells *Phys Rev Lett* **1997**, *79*, 511.

(8)   Ferrand, D.; Cibert, J.; Bourgognon, C.; Tatarenko, S.; Wasiela, A.; Fishman, G.; Bonanni, A.; Sitter, H.; Kolesnik, S.; Jaroszyski, J.; Barcz, A.; Dietl, T. Carrier-induced ferromagnetic interactions in p-doped Zn(1-x)MnxTe epilayers *J Cryst Growth* **2000**, *214*, 387.

(9)   Das Sarma, S.; Hwang, E. H.; Kaminski, A. How to make semiconductors ferromagnetic: a first course on spintronics *Solid State Commun* **2003**, *127*, 99.

(10) Ohno, H. Making nonmagnetic semiconductors ferromagnetic *Science* **1998**, *281*, 951.

(11) Sonoda, S.; Shimizu, S.; Sasaki, T.; Yamamoto, Y.; Hori, H. Molecular beam epitaxy of wurtzite (Ga,Mn)N films on sapphire(0001) showing the ferromagnetic behaviour at room temperature *J Cryst Growth* **2002**, *237*, 1358.

(12) Ueda, K.; Tabata, H.; Kawai, T. Magnetic and electric properties of transition-metal-doped ZnO films *Appl Phys Lett* **2001**, *79*, 988.

(13) Rovezzi, M.; D'Acapito, F.; Navarro-Quezada, A.; Faina, B.; Li, T.; Bonanni, A.; Filippone, F.; Bonapasta, A. A.; Dietl, T. Local structure of (Ga,Fe)N and (Ga,Fe)N:Si investigated by x-ray absorption fine structure spectroscopy *Phys Rev B* **2009**, *79*.

(14) Kuroda, S.; Nishizawa, N.; Takita, K.; Mitome, M.; Bando, Y.; Osuch, K.; Dietl, T. Origin and control of high-temperature ferromagnetism in semiconductors *Nat Mater* **2007**, *6*, 440.

(15) Gu, L.; Wu, S. Y.; Liu, H. X.; Singh, R. K.; Newman, N.; Smith, D. J. Characterization of Al(Cr)N and Ga(Cr)N dilute magnetic semiconductors *J Magn Magn Mater* **2005**, *290*, 1395.

(16) Moreno, M.; Trampert, A.; Jenichen, B.; Daweritz, L.; Ploog, K. H. Correlation of structure and magnetism in GaAs with embedded Mn(Ga)As magnetic nanoclusters *J Appl Phys* **2002**, *92*, 4672.

(17) Mishra, R.; Zhou, W.; Pennycook, S. J.; Pantelides, S. T.; Idrobo, J. C. Long-range ferromagnetic ordering in manganese-doped two-dimensional dichalcogenides *Phys Rev B* **2013**, *88*.

(18) Ranmohotti, K. G. S.; Djieutedjeu, H.; Poudeu, P. F. P. Chemical Manipulation of Magnetic Ordering in $Mn_{1-x}Sn_xBi_2Se_4$ Solid-Solutions *J Am Chem Soc* **2012**, *134*, 14033.

(19) Franceschetti, A.; Dudiy, S. V.; Barabash, S. V.; Zunger, A.; Xu, J.; van Schilfgaarde, M. First-principles combinatorial design of transition temperatures in multicomponent systems: The case of Mn in GaAs *Phys Rev Lett* **2006**, *97*.

(20) Djieutedjeu, H.; Makongo, J. P. A.; Rotaru, A.; Palasyuk, A.; Takas, N. J.; Zhou, X. Y.; Ranmohotti, K. G. S.; Spinu, L.; Uher, C.; Poudeu, P. F. P. Crystal Structure, Charge Transport, and Magnetic Properties of $MnSb_2Se_4$ *Eur J Inorg Chem* **2011**, 3969.

(21) Djieutedjeu, H.; Olvera, A.; Page, A.; Uher, C.; Poudeu, P. F. P. High-T-c Ferromagnetism and Electron Transport in p-Type $Fe_{1-x}Sn_xSb_2Se_4$ Semiconductors *Inorg Chem* **2015**, *54*, 10371.

(22) Djieutedjeu, H.; Poudeu, P. F. P.; Takas, N. J.; Makongo, J. P. A.; Rotaru, A.; Ranmohotti, K. G. S.; Anglin, C. J.; Spinu, L.; Wiley, J. B. Structural-Distortion-Driven Cooperative Magnetic and Semiconductor-to-Insulator Transitions in Ferromagnetic $FeSb_2Se_4$ *Angew Chem Int Edit* **2010**, *49*, 9977.

(23) Djieutedjeu, H.; Zhou, X. Y.; Chi, H.; Haldolaarachchige, N.; Ranmohotti, K. G. S.; Uher, C.; Young, D.; Poudeu, P. F. P. Donor and acceptor impurity-driven switching of magnetic ordering in $MnSb_{2-x}Sn_xSe_4$ *J Mater Chem C* **2014**, *2*, 6199.

(24) Moroz, N. A.; Lopez, J. S.; Djieutedjeu, H.; Ranmohotti, K. G. S.; Olvera, A.; Ren, P.; Page, A.; Takas, N. J.; Uher, C.; Poudeu, P. F. P. Indium Preferential Distribution Enables Electronic Engineering of Magnetism in $FeSb_{2-x}In_xSe_4$ p-Type High-Tc Ferromagnetic Semiconductors *Chem Mater* **2016**, *28*, 8570.

(25) Ranmohotti, K. G. S.; Djieutedjeu, H.; Lopez, J.; Page, A.; Haldolaarachchige, N.; Chi, H.; Sahoo, P.; Uher, C.; Young, D.; Poudeu, P. F. P. Coexistence of High-T-c Ferromagnetism and n-Type Electrical Conductivity in $FeBi_2Se_4$ *J Am Chem Soc* **2015**, *137*, 691.

(26) Sheldrick, G.; version 6.12 ed.; Bruker analytical X-ray instruments Inc.: Madison, WI, USA, 2000.

(27) Sheldrick, G. M. Crystal structure refinement with SHELXL *Acta Cryst C* **2015**, *71*, 3.

(28) Brandenburg, K.; Putz, H.; Version 3.0 c ed.; Crystal Impact GbR: Bonn, Germany, 2005.

(29) Shannon, R. Revised effective ionic radii and systematic studies of interatomic distances in halides and chalcogenides *Acta Cryst A* **1976**, *32*, 751.

(30) Zhang, W.; Yang, Z.; Liu, J.; Zhang, L.; Hui, Z.; Yu, W.; Qian, Y.; Chen, L.; Liu, X. Room temperature growth of nanocrystalline tin (II) selenide from aqueous solution *J Cryst Growth* **2000**, *217*, 157.

(31) Biesinger, M. C.; Payne, B. P.; Grosvenor, A. P.; Lau, L. W.; Gerson, A. R.; Smart, R. S. C. Resolving surface chemical states in XPS analysis of first row transition metals, oxides and hydroxides: Cr, Mn, Fe, Co and Ni *Appl Surf Sci* **2011**, *257*, 2717.

(32) Grosvenor, A.; Kobe, B.; Biesinger, M.; McIntyre, N. Investigation of multiplet splitting of Fe 2p XPS spectra and bonding in iron compounds *Surf Interface Anal* **2004**, *36*, 1564.

(33) Graat, P. C. J.; Somers, M. A. J. Simultaneous determination of composition and thickness of thin iron-oxide films from XPS Fe ^{2}p spectra *Appl Surf Sci* **1996**, *100*, 36.

(34) Blinowski, J.; Kacman, P. Spin interactions of interstitial Mn ions in ferromagnetic GaMnAs *Phys Rev B* **2003**, *67*, 121204.

(35) Awschalom, D. D.; Flatte, M. E. Challenges for semiconductor spintronics *Nat Phys* **2007**, *3*, 153.

(36) Dobrowolska, M.; Tivakornsasithorn, K.; Liu, X.; Furdyna, J. K.; Berciu, M.; Yu, K. M.; Walukiewicz, W. Controlling the Curie temperature in (Ga,Mn) As through location of the Fermi level within the impurity band *Nat Mater* **2012**, *11*, 444.

(37) Edmonds, K. W.; Boguslawski, P.; Wang, K. Y.; Campion, R. P.; Novikov, S. N.; Farley, N. R. S.; Gallagher, B. L.; Foxon, C. T.; Sawicki, M.; Dietl, T.; Nardelli, M. B.; Bernholc, J. Mn interstitial diffusion in (Ga,Mn)As *Phys Rev Lett* **2004**, *92*, 037201.

(38) Yu, K. M.; Walukiewicz, W.; Wojtowicz, T.; Kuryliszyn, I.; Liu, X.; Sasaki, Y.; Furdyna, J. K. Effect of the location of Mn sites in ferromagnetic $Ga_{1-x}Mn_xAs$ on its Curie temperature *Phys Rev B* **2002**, *65*, 201303.

Chapter 5

Decoupling Ruderman-Kittel-Kasuya-Yosida (RKKY) and Super-exchange Contributions in High Tc FeSb2-xBixSe4 Ferromagnetic Semiconductors

5.1 Introduction

In the previous section, we have shown the versatility of a different type of magnetic

semiconductor with the general formula MPn_2Se_4 (M = Mn, Fe ; Pn = Sb,Bi) and have shown

control over the magnetic ordering and carrier concentrations. This control has been the key to

directly observing the effect of reducing the magnetic ion concentration in $Fe_{1-x}Sn_xBi_2Se_4$. As

expected, replacing Fe^{2+} for Sn^{2+} in the structure can drastically reduce the T_c of $Fe_{1-x}Sn_xBi_2Se_4$,

while the electronic properties (carrier concentration) is not drastically affected. Next, we need to understand the role of Bi and Sb in the structure. In previous work, Bi and Sb have demonstrated control over the electronic properties, $FeBi_2Se_4$ being n-type and $FeSb_2Se_4$ being p-type. They both reside at the
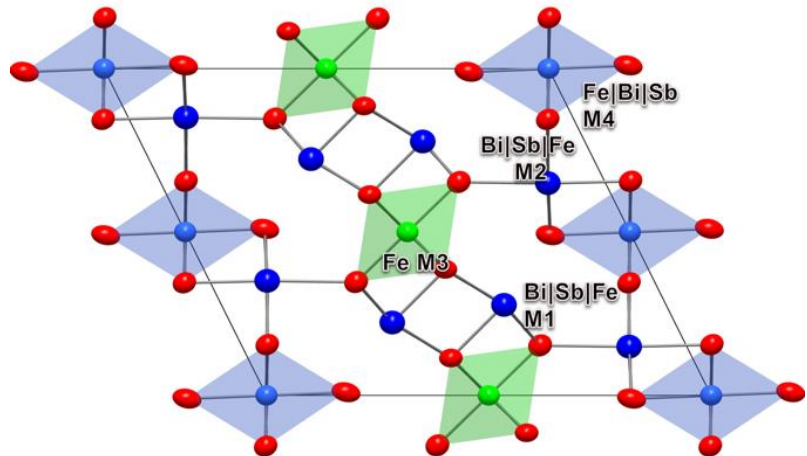

Figure 5. 1 Crystal Structure of FeSb2-xBixSe4. M1 and M2 site is occupied Bi, Sb, and Fe. M4 site is expected to be occupied by Fe, Bi, and Sb This has not been experimentally confirmed. M3 site is

M1 and M2 sites of $FePn_2Se_4$ (Pn = Sb,Bi), of the respective parent structures. They both have different occupation factors within the parent structures, Bi at the M1 site $f^{M1}(Bi) = 84\%$ while Sb at the M1 site $f^{M1}(Sb) = 95.8\%$. The M2 sites also exhibit similar occupancies, Bi at the M2 site $f^{M2}(Bi) = 85.5\%$ while at the M2 site Sb $f^{M2}(Sb) = 96.4\%$. They both dominate their respective sites sharing the rest of the site with Fe. Despite this difference, the T_c in both parent compounds remains constant at 723 K. Carrier concentration has a significant role in the determination of the corresponding phase, which is supported by all our other work on MPn_2Se_4. $FeBi_2Se_4$ and $FeSb_2Se_4$ share the same crystal structure, and their lattice constants are not drastically different. $FeBi_2Se_4$ has lattice constants; *a = 13.3533(17), b = 4.1171(3), c = 15.0687(18), β = 115.037(9)*. $FeSb_2Se_4$ has lattice constants; *a = 13.069(3), b = 3.9671(8), c = 15.192(3), β = 114.99(3)*. The difference in their lattice constants (*Δa = 2.2%, Δb = 3.8%, Δc = -0.8%,* and *Δ β =0.04%*) are small enough that a solid solution between the two (Bi and Sb) is possible. The crystal structure of $FeSb_{2-x}Bi_xSe_4$ can be observed in **Figure 5.1**. Since $FeBi_2Se_4$ is n-type and $FeSb_2Se_4$ is p-type, a solid solution between the two should have one of two possibilities: either 1) the Fermi energy will gradually shift with increasing Bi from the top of the valence band to the bottom of the conduction band, creating a semi-insulating magnetic semiconductor or 2) The n-type nature of Bi will gradually annihilate the p-type nature of Sb, creating an insulating ceramic and possibly eliminate the stability of the ferromagnetic phase in the sample due to the low carrier concentration and the lack of bound magnetic polaron overlap. In either scenario 1 or 2, the carrier concentration should move below the percolation limit necessary for bound magnetic poltroon overlap. The solid solution can also be achieved without changing the Fe concentration in the crystal. As a result, we should be able to drastically alter the carrier concentration and correlate its effect to any change in the magnetic phase. Keeping the Fe

concentration constant will allow for the direct observation of a metal-insulator transition and its effect on the resulting magnetic phase. This should elucidate the role of itinerant carriers in the magnetic coupling and bring to light the presence of any other magnetic coupling mechanisms. The BMP model is theorized to be the dominant magnetic coupling mechanism. So, a drastic reduction in carrier concentration should have an effect on the magnetic properties if this were the case. In the event $FeSb_{2-x}Bi_xSe_4$ remains ferromagnetic, then the presence of superexchange coupling arising the presence of Fe at the M1 and M2 sites would be confirmed.

5.2 Results and Discussion

5.2.1 Structure

X-ray diffraction on polycrystalline powders of the synthesized $FeSb_{2-x}Bi_xSe_4$ samples confirmed the formation of single phase as can be observed by the agreement between experimental XRD Pattern and the theoretical pattern simulated from the single crystal data for the parent structure $FeSb_2Se_4$. A select XRD pattern for composition x = 0.2 is shown in **Figure 5.2a**, alongside the lattice parameters extracted from the diffractograms through Rietveld analysis and single crystal refinement data for select compositions. The solid solution was successful throughout the whole substitution values going from $0.2 \leq x \leq 1.4$. This is further shown by the fact that the full solution is isostructural with the $FeSb_2Se_4$ parent compound that was the starting point for this study.
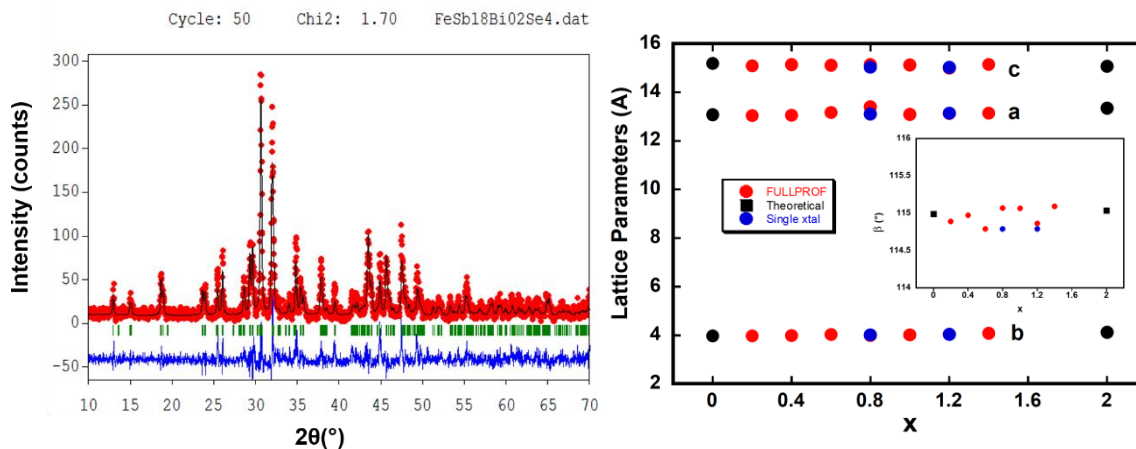
Figure 5. 2 a) Fitted experimental XRD pattern for full $FeSb_{1.8}Bi_{0.2}Se_4$ compound showing excellent agreement between the x = 0.2 compound and parent structure FeSb2Se4, highlighting the successful incorporation of Bi into the compound. Solid solution was successful from x = 0.2 to x = 1.4. For x = 1.6 - 1.8, the mixture is mostly comprised of binary B2Se3. **b**) Extracted lattice parameters for the solid solution series using Rietveld Refinement analysis. Lattice parameters a,b,c, and β all exhibit monotonic increases

The x = 1.6 and x = 1.8 compositions were unsuccessful are they were isostructural with Rhombohedral Bi_2Se_3, implicating the reaction did not fully transition from Fe doped Bi_2Se_3 binary into the desired ternary structure. These were not successful and other reaction pathways are being explored to improve the crystallinity and purity of the x = 0.6, x = 1.6, and x = 1.8 compounds.

DSC scans from room temperature to 1300K were also performed to confirm phase purity. The endothermic melting peaks for the $FeSb_{2-x}Bi_xSe_4$ series are shown in **Figure 5.3a**. Despite the presence of an incongruent melting transition, the onset temperatures

Show a regular trend. The onset temperature of melting increases with increasing Bi in the crystal (**Figure 5.3b**). Careful analysis of the onset temperature of the melting peaks for the
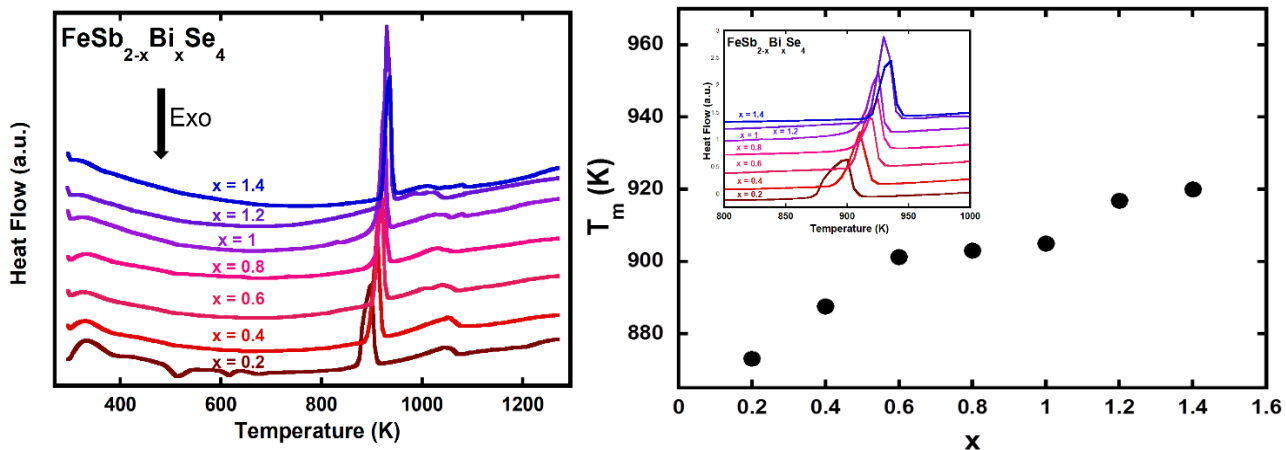
Figure 5. 3 a) Endothermic melting peaks measured using DSC for $FeSb_{2-x}Bi_xSe_4$ series. **b)** Extracted onset melting temperatures and plotted as a function of Bi content (x) highlighting the positive correlation between melting and bismuth content.

series shows a significant increase in melting temperature upon increasing Bi content. The observation of this increase in melting temperature with increasing Bi content is another indication that the solid solution was successful. The onset of melting begins at $T_m = 873$ K for x $= 0.2$ and increases to 915K for x = 1.4.

To further understand the effect of partial substitution of Sb by Bi on the functional properties, we need to understand how Bi substitutes for Sb, namely the distribution of metal atoms at all metal positions (M1(4i), M2(4i), M3(2c) and M4(2b)) within the crystal lattice. The x = 0.8 and x = 1.2 bulk powders yielded sizable and good quality single crystals which were experimentally probed for structure and atomic occupation using single crystal diffraction. The x = 0.8 bulk

produced the x = 0.79 single crystal and the x = 1.2 bulk produced the x = 1.16 single crystal.
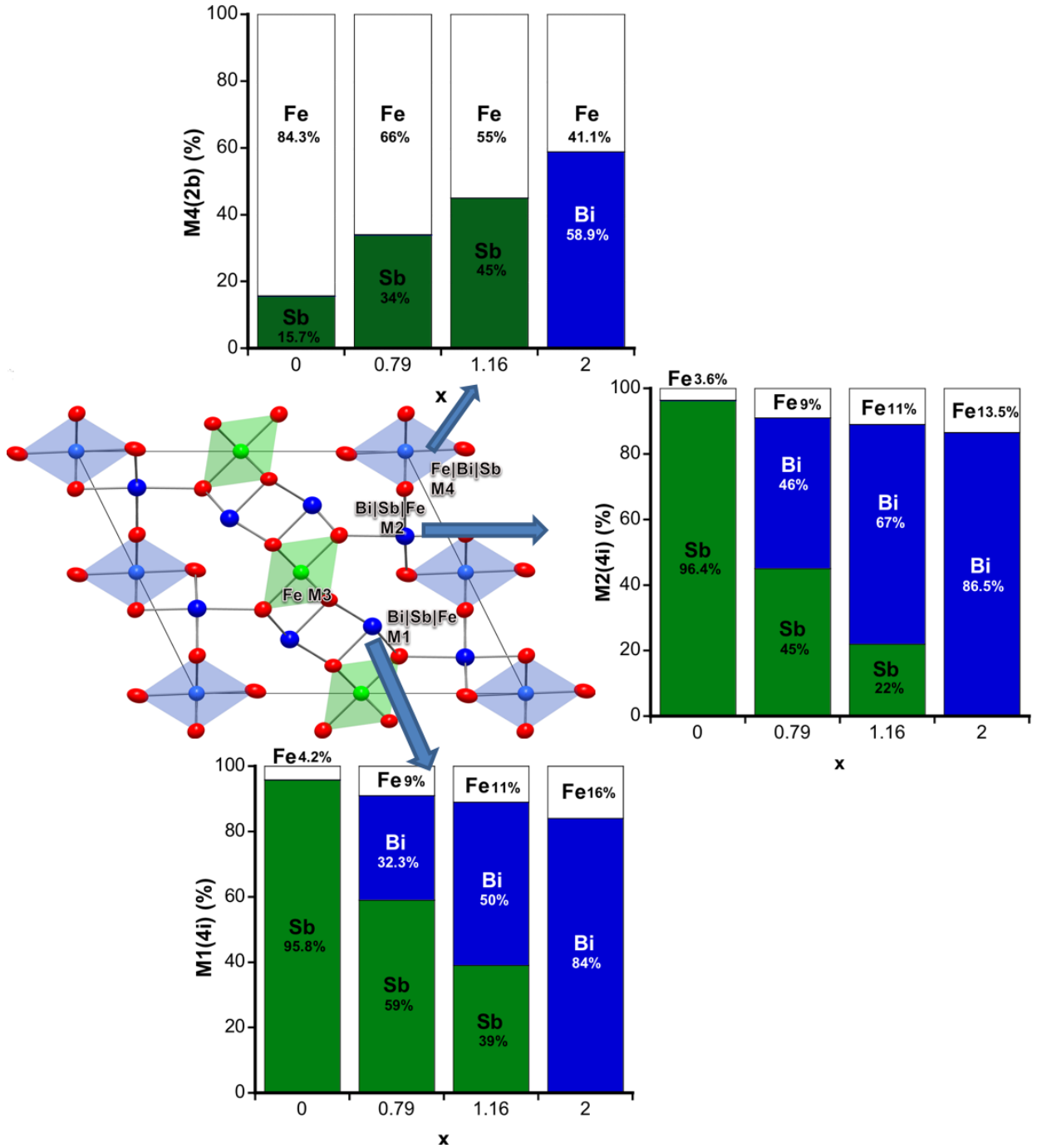
Figure 5. 4 FeSb$_{2-x}$Bi$_x$Se$_4$ crystal occupancy diagram detailing occupancy as a function of Bi composition (x).

Figure 5.4 details the occupation of the M1, M2, and M4 sites and compares them across the x = 0, x = 0.8, x = 1.16, and x = 2 compositions.

The M1 and M2 sites are dominated by Pn (Pn = Sb, Bi) members. So, Increasing the x value from x = 0 to x = 0.8 is expected to decrease the percentage of Sb and increase the percentage of Bi at these sites. That is exactly what we observe; the M1 site exhibits a reduction in Sb
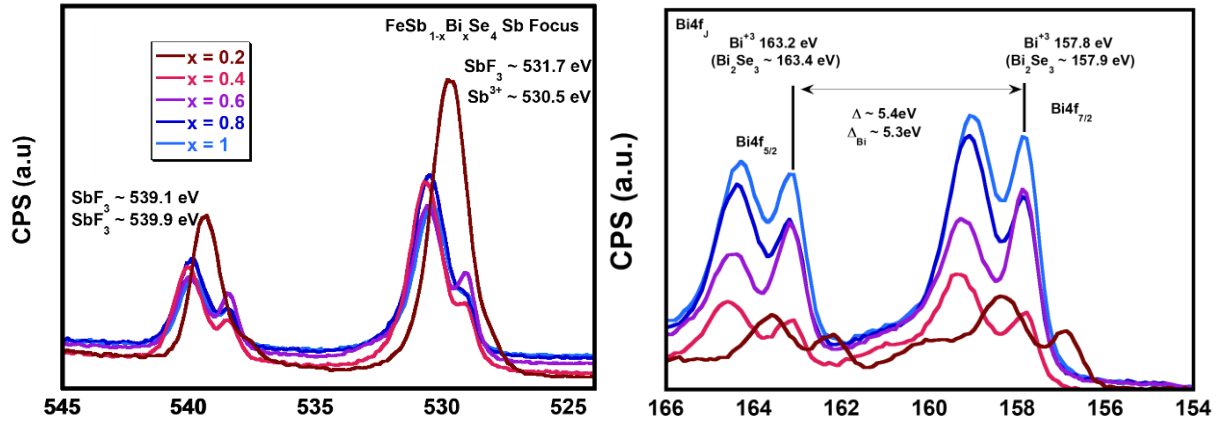
Figure 5. 5 a) and **b**) X-ray photoelectron spectroscopy spectra of Sb_3d$_{5/2}$ and Bi_4f$_{7/2}$ shell electronc for selected FeSb$_{2-x}$Bi$_x$Se$_4$ compositions.

occupancy. The M1 site decreases from *f^{M1}(Sb) = 95.8% for x = 0 to f^{M1}(Sb) = 59% for x = 0.8. It is reduced even further f^{M1}(Sb) = 39% for x = 1.2. Meanwhile the Bi occupancy for x = 0.8 is f^{M1}(Bi) = 32.3% and increases to f^{M1}(Bi) = 50% for x = 1.2.* The M2 site experiences the same trend, but the change in occupancies are larger in magnitude. The M4 site shows different atomic ordering behavior. When Bi replaces Sb in the crystal, It also displaces Sb from the M1 and M2 sites and moves some of it to the M4 site. As can be seen in **Figure 5.4**, *f^{M4}(Sb)* increases with increasing x value. Even though Bi is coming in, the M4 site prefers Sb. In order to balance the change in atomic arrangement, Fe is displaced from the M4 site and shared between the M1 and M2 sites. This increases the conformational entropy of Fe within the crystal. This has an effect on the magnetism which will be discussed in detail later.

The incorporation of Bi into the crystal structure was further confirmed by X-ray Photoelectron Spectroscopy (XPS) of selected compositions. The XPS spectra for Sb_3d$_{5/2}$ peak at binding energy ~530.5 eV which is associated with Sb^{3+} in Sb$_2$Se$_3$. The intensity of the of Sb_3d$_{5/2}$ scales negatively with Bi content (Figure 5b) indicating that Bi is successfully incorporating into the crystal. This further confirms effective incorporation of Bi ions with the FeSb$_{2-x}$Bi$_x$Se$_4$ crystal in a 3+ oxidation state. This can be seen by observing the satellite peaks and their excitation energy. A Bi^{3+} 4f$_{7/2}$ peak is observed at 157.8 eV, which is expected for Bi^{3+} coordinated by Se^{2-} (157.9 eV). The Bi^{3+}4f$_{5/2}$ peak is also observed at 163.2 eV, confirming the oxidation state as 3+ when compared to Bi2Se3 (163.4 eV).

5.2.2 Electronic Transport

PXRD, DSC, XPS, and single crystal diffraction all confirm the successful incorporation of Bi^{3+} into the FeSb$_{2-x}$Bi$_x$Se$_4$ crystal. As mentioned before, the purpose of this study was to probe the interplay of carrier concentration on the stabilizing magnetic phases. Creating solid solutions between FeSb$_2$Se$_4$ (p-type) and FeBi$_2$Se$_4$ (n-type) is expected to reduce the effective carrier concentration by promoting a second electron carrier channel in the mostly p-type bulk sample. As more Bi gets incorporated into the FeSb$_{2-x}$Bi$_x$Se$_4$ crystal, the bulk is driven towards n-type conduction carriers. As the electron concentration increases with increasing Bi, the effective carrier concentration is reduced due to the carrier recombination. Hall effect measurements are the scientific standard when trying to measure carrier concentration because it probes the effective carrier concentration directly using perpendicular magnetic field and probe current. Hall Effect measurements were performed for the full FeSb$_{2-x}$Bi$_x$Se$_4$,

but a stable hall voltage was difficult to measure. The hall signal had significant noise and would
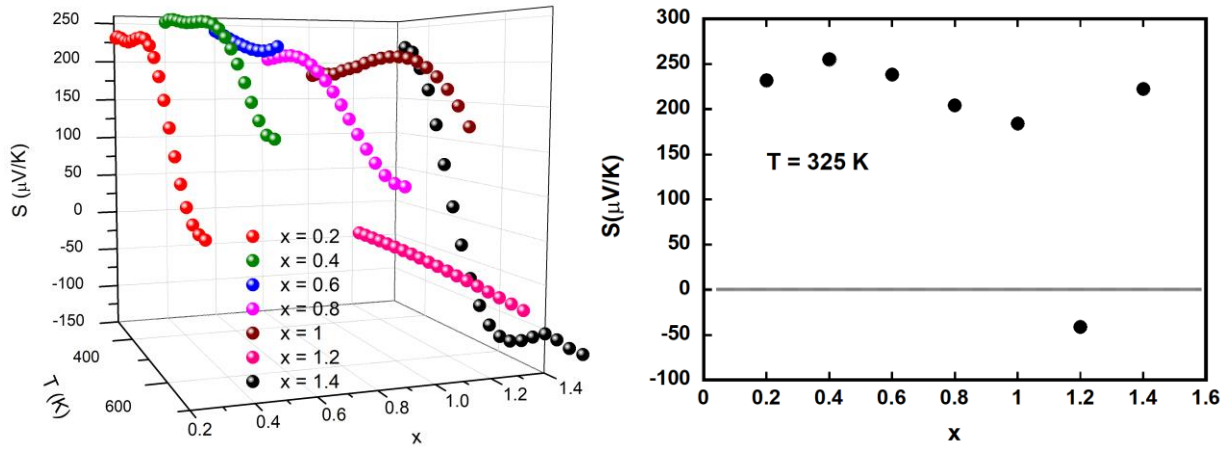
Figure 5. 6 a) 3D Plot of Seebeck coefficient, Temperature (300-700K), and Bi content, x. Thermopower scales inversely with carrier concentration, and is an alternative method for determining conduction type. **b**) Isothermal cross section (325 K) of the S,T, and x phase space highlighting the trend between Seebeck and Bi content, x.

thermalize indefinitely. In the absence of a hall coefficient, another proxy for carrier concentration had to be considered. Seebeck coefficient has a well-established inverse dependence on carrier concentration. This can be observed in the Mott-Boltzmann Formalism which relates Seebeck, **S,** to temperature , **T**, effective mass , **m***, and carrier concentration, **n,** according to the following relation;

$$S = \frac{8\pi^2 k_B^2 T}{3eh^2} m^* \left(\frac{\pi}{3n}\right)^{2/3}$$

The Mott-Boltzmann formalism applies to metals and degenerate semiconductors with parabolic band and approximates energy independent charge carrier scattering as being proportional to the carrier concentration. Making the assumption that the **m*** doesn't change significantly with Bi content, i.e. no significant band distortions as a function of Bi incorporation, then it is reasonable to use the S coefficient as a proxy for observing the dependence of n on Bi content (**x**).

Given that S generally decreases when the concentration of mobile carriers increases, one would

hypothesize that increasing Bi would reduce the mobile charge carriers as a result of carrier

recombination. To probe the effect of Bi incorporation on the effective carrier concentration,

high temperature (300 K – 700 K) Seebeck measurements were performed for the $FeSb_{2-x}Bi_xSe_4$

series. In order to better visualize the data, a 3D plot was constructed for the full S,T, and x

phase space as shown in **Figure 5.6a** and **5.6b**. This trend is initially observed going from the S

~ 230 µV/K at x = 0.2 to S ~ 255 µV/K at x = 0.4. Further incorporation x ≥ 0.4 results in a

reduction of Seebeck going from S ~ 255 µV/K at x = 0.4 to S ~ 183 µV/K at x = 1. This is

counter-intuitive to what was hypothesized, this can be explained through the effect Bi has on the

conduction channels. As Bi incorporates into the $FeSb_{2-x}Bi_xSe_4$ crystal, a second electron

conduction channel is created. As these mobile electrons shuttle across the band states they

remain itenerant. A competing effect to this phenomenon is the recombination of itinerant holes

and electrons. As electrons overtake the hole concentration, the effective mobile carrier

concentration is significantly increased, but they are competing against a temperature gradient

for voltage generation. As a result, despite the increase in effective carrier concentration, Bi

incorporation past x = 0.4 results in gradual suppression of the thermopower. This effect

becomes discernable for the x = 1.2 concentration as the sign of S flips to negative thermopower.

The Seebeck changes sign to S ~ -41µV/K, indicating that the electron concentration has

completely overtaken the hole concentration as a result of Bi incorporation. Even more intriguing

is the temperature independence of the S coefficient for the x = 1.2 composition. This is a rare

phenomenon in which the carrier mobility, rather than the carrier concentration, was thermally

activated and contributed to the thermopower. Further increasing Bi content to x = 1.4, results in

a tell tale signature of bipolar conduction with a cross-over temperature of T_X ~ 483K. The

thermopower for x = 1.4 (S(x=1.4)) has a similar sign and magnitude to its lower Bi content counterparts.

Looking at the Low Temperature (LT) phase space, a similar trend can be observed as a function of Bi content. Looking at **Figure 5.7a** shows that thermopower has a inverse relation to Bi content. This can be generally observed upon inspecting the 3D S,T, and x phase space. This is most obvious, **Figure 5.7b**, going from the S(x = 0.2, 100 K) = 378 μV/K to S(x =1, 100K) = 1 μV/K. Increasing Bi content further results in a complete sign switch, S(x = 1.2, 100K = -13 μV/K. This gradual flip at cryogenic temperatures across x is indicative of the carrier concentration dependence on Bi content. This further validates the role Bi has in determining the
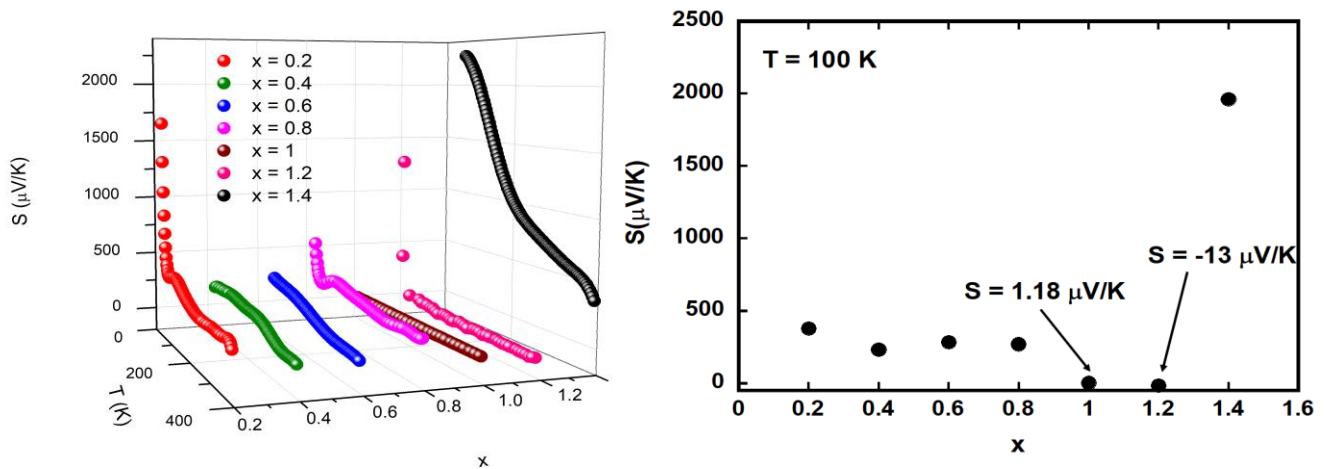
Figure 5. 7 . **a**) Low Temperature 3D Plot of Seebeck coefficient, Temperature (2-300K), and Bi content, x, in FeSb$_{2-}$$_xBi_xSe_4$. Representation is plotted with Bi content being the transverse panel to highlight the dependence **b**) Isothermal cross section (100 K) of the S,T, and x phase space highlighting the trend between Seebeck and Bi content, x. Thermopower exhibits negative correlation to Bi content, with carrier type cross over past x =1.

conduction type of the resulting phase. Further Bi incorporation enhances the S from S(x= 1.4, 325 K) = 222 μV/K up to S(x = 1.4, 100 K) = 1962 μV/K.

Both the LT and HT 3D (S, T, x) data sets are testaments to the degree of control attainable through Bi substitution over the carrier concentration in $FeSb_{2-x}Bi_xSe_4$.

S measurements have qualitatively confirmed the tunability of the conduction type achievable through Bi substitution. This tunability should be observable in the electronic transport measurements. LT resistivity, ρ, measurements were performed in order to observe the carrier dependence on Bi content. The LT ρ has a direct dependence on carrier concentration and can detect the effect Bi has on the carrier concentration, as the thermopower is implicating. A 2D and 3D plot of (S, T, x) is plotted in **Figure 5.8a** and **Figure 5.8b** exhibiting the ρ dependence as a function of temperature (2K – 400K) and Bi content, x. Analyzing the Bi dependence shows a clear a monotonic increase in ρ going from ρ(x=0.2) to ρ(x=1). This is observable in the resistance onset temperatures, as well as the magnitude of the cutoff temperatures. Further Bi incorporation actually results in a very

Figure 5. 8 a) 2D and **b**) 3D representation highlighting the resistance dependence on Bi content of the full S, T, and x phase space.

interesting electronic phenomena. The x = 1.2 sample exhibits a sharp maximum at T_{max} ~ 19K, after which ρ drops off significantly towards p = 0, but never fully reaches ρ = 0. This anomaly is accompanied by a change in conduction type at can be seen in **Figure 5.7a** for the x = 1.2

composition. This anomaly is a Lifshitz transition, normally associated with changes in the Fermi Surface (FS) topology of the material. The Lifshitz transition is a rare quantum critical point that is normally only achievable in quantum critical materials where there is significant control over various solid state material properties. Further evidence of the tenability achievable over the electronic transport properties. Increasing Bi content further to x = 1.4 results in the most resistive sample in the FeSb$_{2-x}$Bi$_x$Se$_4$ series. This yet another indication of the bipolar conduction mechanism reducing the number of itinerant carriers.

The trend we observe if LT ρ continues in the HT ρ measurements as shown in **Figure 5.9a**. Increasing the Bi content results in the expected increase in the ρ measured. In order to better
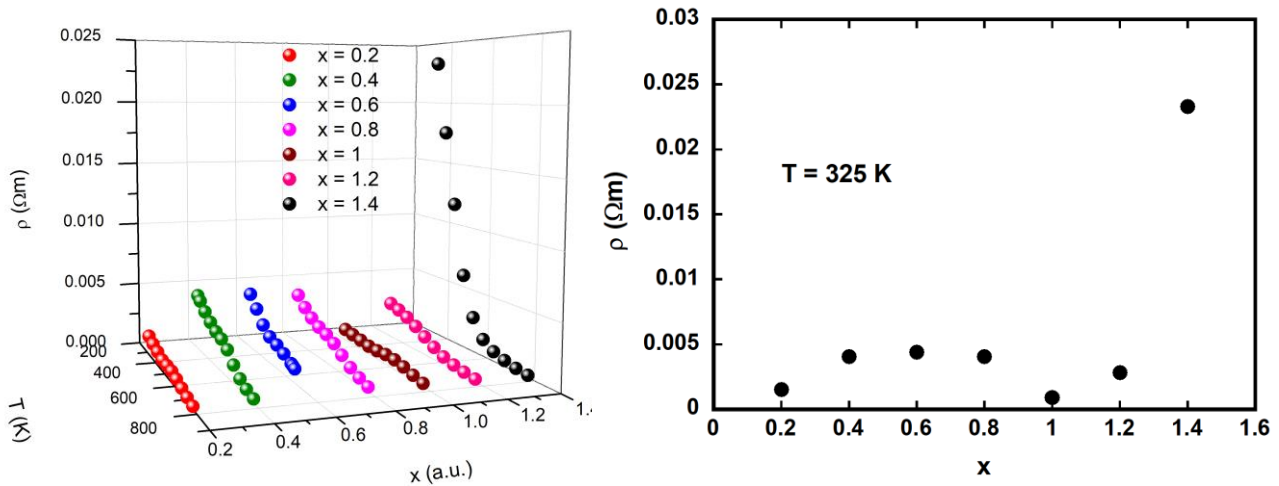
Figure 5. 9 a) 3D Plot of the S, T, and x phase space for the full FeSb2-xBixSe4 series. **b**) Isothermal Cross section of the phase space at T = 325 K exhibiting the dependence of ρ on Bi content, x. Initially, ρ increases and then decreases near the cross over concentration and shoots back up near the end of the series at x = 1.4.

demonstrate the ρ dependence on Bi content, x, and isothermal cross section of the 3D phase space is taken at T = 325 K, plotted in **Figure 5.9b**. HT ρ measurements show the same dependence on the Bi content as the LT ρ measurements. This corroborates the effect Bi content has on the effective carrier concentration and is affirmed by the LT and HT S measurements.

5.2.3 Magnetism

Seebeck measurements have qualitatively shown a carrier concentration modification with Bi substitution that was detectable in both the LT and HT resistance measurements. The next line of questioning would be the magnetic properties. The purpose of this study was to detangle the degree of correlation between the Curie temperature, T_c, and the stabilizing effect of itinerant magnetism. It follows that any change in the magnetic properties would be a result of Bi substitution in $FeSb_{2-x}Bi_xSe_4$. This is especially true since the Fe content present in the crystal across the $FeSb_{2-x}Bi_xSe_4$ remains constant.

To probe the effects of the substitution of Sb by Bi o the magnetic behavior of $FeSb_{2-x}Bi_xSe_4$ series, temperature-dependent moment data at LT (**Figure 5.10a**) and HT (**Figure 5.11a**) were measured using a SQUID magnetometer. Field-Cooled (FC) data measured under an applied external magnetic field of 100 Oe are presented in both plots. Is order to make the data more understandable, a 3D plot was constructed of the data plotted against temperature and Bi content, x. In the LT regime (2-300K) all samples exhibit a monotonic decrease in moment with increasing temperature, indicative of ferromagnetic-like behavior. They also never reach M = 0, and so they remain ferromagnetic-like up to 300K. They also exhibit the same magnetic transition at T = 110 K that has been observed in both parent compounds, $FeSb_2Se_4$ and $FeBi_2Se_4$. The transition is typical of the $FePn_2Se_4$ based (Pn = Sb or Bi) phases and is likely related to the magnetic spin re-orientation resulting from a local structural distortion within the magnetic sub-lattice $[FeSe_6]$ upon cooling. Looking beyond the ferromagnetic-like moment

behavior and looking past the magnetic transitions we have observed before, there is a distinct trend in the moment as more and more Bi accommodates into the structure. Again, the Fe content present in the sample remains constant, so the any magnetic phases stabilized as a result of superexchange between the $[FeSe_6]$ octahedral chains should remain fairly constant. There are other magnetic phases stabilized within the bulk as well, these are any magnetic interactions resulting from an RKKY interaction, the exchange interaction between the Fe^{2+} ions in the crystal and the itinerant carriers shuttling around the band structure interacting with these hybridized ions. Therefore, as Bi incorporates into the structure and increases the number of itinerant electrons, the number of localized holes coupling through the RKKY mechanism are going to be significantly affected. This is the effect that can be observed in **Figure 5.10a**, where the global maximum are at the limits of the $FeSb_{2-x}Bi_xSe_4$ series, and a minimum in moment is achieved for the x = 0.8 composition. In order to clarify this trend, **Figure 5.10b** shows a cross section of the 3D (M,T,x) phase space at T = 100K, exhibiting the effect Bi content has on weakening the RKKY interaction. This is most obvious going from $M(x=0.2,100K) \sim 1.44 \times 10^{-2}$ μ_B/F.U. down to $M(x=0.8,100K) \sim 8.47 \times 10^{-3}$ μ_B/F.U.. Increasing the Bi content further results in an enhancement of the moment up to $M(x=1.2,100K) \sim 1.55 \times 10^{-2}$ μ_B/F.U. and saturates thereafter at x = 1.4. Considering that SQUID measures bulk moment, and that the bulk moment is a result of many different contributions, $M_{Bulk} = M_{SupEx}$ (Super-Exchange) + M_{RKKY} (RKKY) + M_{DE} (Direct Exchange)+ M_{DM2} (Dzyaloshinsky-Moriya). Since the RKKY interaction is

dependent on the itinerant carrier concentration, it is rational that the signal would approach a minimum as a result of Bi incorporation, decreasing as the bulk becomes less p-type and increasing as it becomes more n-type. This is direct evidence that there is a reduction in percolative overlap in the RKKY stabilized BMP's present in the system. Especially considering the BMP's are more activated at cryogenic temperatures. The LT window is the ideal probe to observe the BMP's efficacy. Next, the effect on the critical temperature should observed. LT SQUID measurements are the best medium to determine the correlation between itenerant carriers and their magnetic enhancement, but both parent compounds, $FeSb_2Se_4$ and $FeBi_2Se_4$, have $T_c \sim 450$ K. Given that the magnetic properties are stabilized via two mechanisms, $M_{Bulk} =$

Figure 5. 10 a) 3D (M,T,x) of the $FeSb_{2-x}Bi_xSe_4$ series showing the effect Bi incorporation has on the RKKY interaction. **b**) An Isothermal cross section of the 3D (M,T,x) phase space at T = 100K.

$M_{SupEx} + M_{RKKY}$, it can finally be determined if the origin of the magnetic phase with $T_c \sim 450$ K is stabilized through the magnetic symmetry or through the itinerant carriers.

Analyzing the HT SQUID data in order to decouple the origin of magnetism, one may notice that

the $T_c \sim 450$ K actually remains constant throughout the entire series. The T_c is not affected to

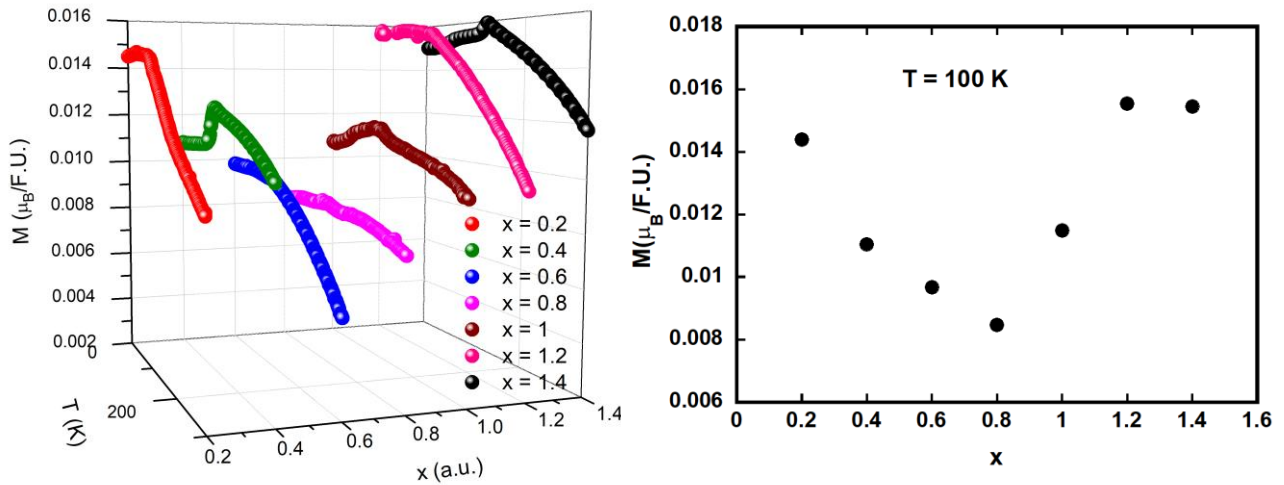any degree by the Bi incorporation. This implies that the magnetic phase stabilizing the high $T_c \sim$
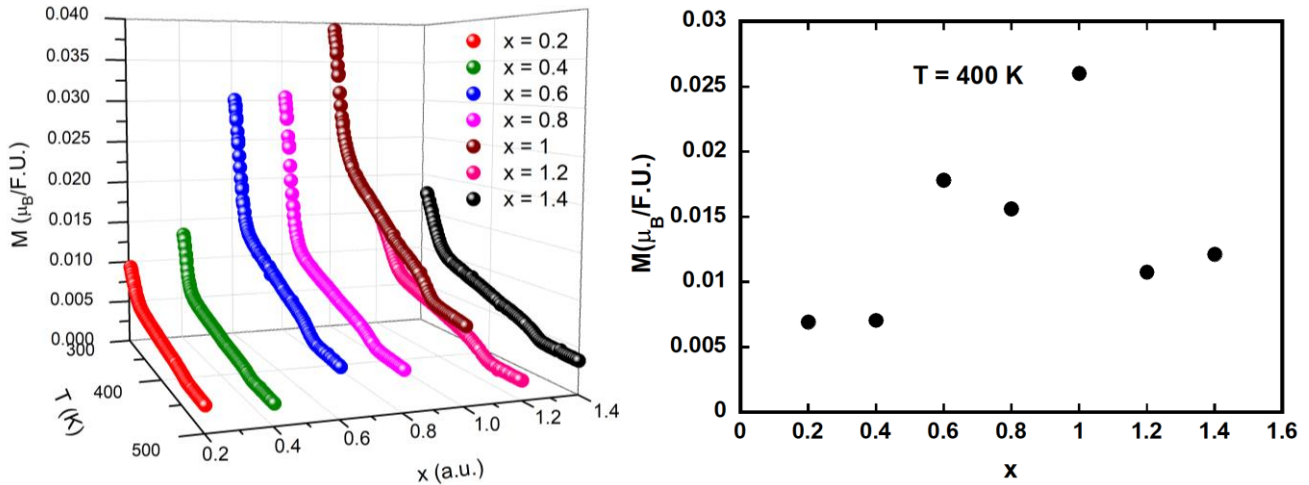
Figure 5. 11 a) 3D (M,T,x) of the $FeSb_{2-x}Bi_xSe_4$ series showing the effect Bi incorporation has on the RKKY

interaction. b) An Isothermal cross section of the 3D (M,T,x) phase space at T = 100K.

450 K is actually completely due to the symmetry and pairing interaction of the $[FeSe_6]$

octahedra. This result supports the presence of weak itinerant magnetism present in these

samples, as they couple and enhance the moments, but percolate at much lower temperatures. As

a result, the T_c remains the same throughout the entire series. What is observed is a similar

monotonic dependence, but in the opposite direction. There is an increase in the moment

measured with increasing Bi content. This trend is most observable by looking at cross section.

Figure 5.11b shows an isothermal cross section at T = 400 K of the 3D (M,T,x) phase space

showing the dependence the HT moment has on Bi content. The moments measured are actually

enhanced, in an opposite trend to the LT measurements. The contribution of the RKKY

stabilized magnetic phase is also negligible due to the high temperature and thermalized spins.

So, where does the enhancement come from? This enhancement likely comes from the

occupational cascading effect that results from incorporating Bi into the $FeSb_{2-x}Bi_xSe_4$ crystal. We have shown using single crystal diffraction that Bi selectively occupies the semiconducting sites, M1 and M2. As a result, some of the Sb occupying these sites are selectively "pushed" out by the large Bi ions to the magnetic, M4, site. In order to balance out the steric interactions, Fe is then "pushed" out from the M4 site back to the semiconducting sites, M1 and M2. A result, the number of anti-site defects increases significantly with increasing Bi content, which reduces the average Inter-Fe^{2+} distance in the crystal. The reduction in average ion distance would boost the super-exchange stabilized magnetic phase. While it does not boost the T_c, it is clear the Moment is enhanced with the increased Fe anti-site defects.

The effect of Bi incorporation, however, goes beyond the temperature dependent moment. Isothermal Magnetization measurements were performed on the full $FeSb_{2-x}Bi_xSe_4$ series, but only a single scan for the x = 0.6 composition is shown since they all exhibited similar field-dependent behavior (**Figure 5.12a**). A separate plot is shown which shows the Saturation Magnetization, M_S, dependence on Bi content, x (**Figure 5.12b**). While the temperature dependent moment is enhanced in the HT window, we see the effect that reducing the eeffective carrier concentrations has on the M_S. The trend actually reflects what is observed in the LT M(T) window. Increasing Bi content, x, results in a reduction of the M_S up to the x = 1.2 composition, at which there is a precipitous drop below the $M_S = 0.05$ μ_B/F.U. threshold. Increasing to x = 1.4 shows and increase in the M_S, likely due to the uptick in the electron concentration, despite the presence of increased bipolar conduction channels. Looking at the **Figure 5.12a**, one can observe clear
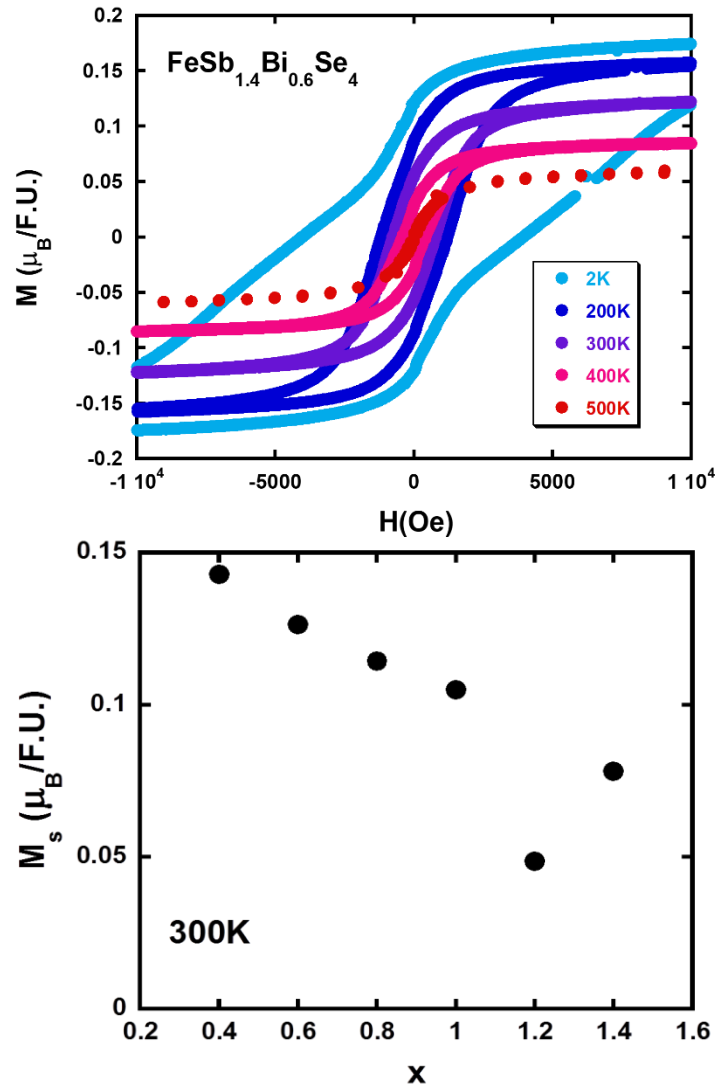
Figure 5. 12 a) Hysteresis measurement on x = 0.6, $FeSb_{1.4}Bi_{0.6}Se_4$ showing wasp-waisting, competing AFM and FM phases, and the large coercivity in the sample. **b**) Saturation magnetization dependence on Bi content, x.

coercivity down from T = 2K all the way to T = 400K. At 500K, the hysteresis loop has no

coercivity, but maintains the typical S-shaped curve of ferromagnetism. This is a signature of

super-paramagnetic behavior. Likely, the result of competing AFM and FM phases present in the

$FeSb_{1.4}Bi_{0.6}Se_4$ bulk as wasp-waisting occurs in lower temperature scans, and frustrated super-

paramagnetic phases result past the $T_c \sim 450$ K.

5.3 Conclusion

We have systematically investigated the effect of isoelectronic Bi incorporation on carrier

modifications, transport properties, and the magnetic behavior in $FeSb_{2-x}Bi_xSe_4$. Doing so has

demonstrated that the origin of the high T_c in the $FePn_2Se_4$ (Pn = Sb or Bi) is a result of super-

exchange (symmetry stabilized) interactions, and that weak itinerant magnetism is present and

enhances the FM-like phase through a pairing interaction that can be observed in the temperature

and field dependent measurements. Pn (Pn = Sb or Bi) substitution has a measurable impact on

the conduction type in the bulk, and can morph the fermi surface significantly enough to exhibit

a Lifshitz transition, $T_{max} \sim 19K$, a notable and difficult quantum critical point to engineer.

Lastly, these results are signatures of the selective control over the electronic properties through

isoelectronic substitution, and how we may engineer the magnetic interactions without changing

the magnetic ion concentration.

Chapter 6

Crystal Structure and Thermoelectric Properties of the 7,7 L Lillianite Homologue, $Pb_6Bi_2Se_9$

6.1 Introduction

Homologous structures have attracted considerable interests as a fertile playground for the search for promising thermoelectric materials.[1-5] Their structural and compositional flexibility offers the possibility of engineering the electronic band structure as well as the phonon vibration modes of various members of the homologous series in order to achieve compounds with high thermoelectric performance, e.i. high electrical conductivity (σ) and Seebeck coefficient (S) and ultra-low the thermal conductivity (κ). The performance of a thermoelectric material is described by the dimensionless figure of merit, $ZT = (S^2\sigma)T/\kappa$, where T is the temperature in Kelvin.[6] It is necessary to tune the electronic and thermal properties to maximize ZT.[7-11] This is a rather difficult task to achieve in a single-phase semiconductor due to the interdependence between various parameters (electrical conductivity, thermopower, and thermal) that enter in the calculation of ZT. Therefore, thermoelectric materials research over the past decade largely focused on the development of concepts and strategies, such as, solid solutions, nanostructuring,[12-18] band alignments[13,18] that resulted in large enhancements of the figure of merit of simple binary compounds such as Bi_2Te_3, PbTe, half-Heuslers, Cu_2Se,[19] $CoSb_3$ [20,21] etc. The enhancements in the figure of merit of these engineered materials arose either from a drastic reduction in the thermal conductivity due to

nanostructuring with minimal disruption of the power factor ($PF = S^2\sigma$), or an enhancement of the PF without increase in the total thermal conductivity. The concept of phase homology is gaining considerable attraction as an elegant alternative way to successfully engineer both the thermal and electrical properties of various members within a given homologous series. Several naturally occurring and synthetic mixed-metal chalcogenides homologous series have been reported. These include, $A_m[M_{1+l}Se_{2+l}]_{2m}[M_{2l+n}Se_{2+3l+n}]$ (A = K, Rb, Cs and M = Sn, Pb);[22,23] $[BiQX]_2[Ag_xBi_{1-x}Q_{2-2x}X_{2x-1}]_{N+1}$ (Q = S, Se; X = Cl, Br; $1/2 \leq x \leq 1$);[4,5] the pavonite, $M_{N+1}Bi_2S_{N+5}$ (M = Ag/Bi or Cu/Bi; $N \geq 2$);[24] and the lillianite, $Pb_{N-1-2x}Bi_{2+x}Ag_xS_{N+2}$;[25] $Pb_{N-1}Bi_2Se_{N+2}$[26,27] and homologous series. Among these homologous families of complex mixed-metal chalcogenides, compositions belonging to the pseudo binary $PbSe - Bi_2Se_3$ phase diagram, such as ternary compounds consisting of varying ratios of $(PbSe)_m(Bi_2Se_3)_n$ layers,[28-32] and $Pb_{N-1}Bi_2Se_{N+2}$[26] have been attracting considerable attention for thermoelectric application due to their moderately lower electrical resistivity compared to their sulfide analogues. For example, in-plane electrical conductivity of ~157 S/cm and out-of plane value of ~41 S/cm where reported for $Pb_5Bi_6Se_{14}$.[33] The out-of-plane electrical conductivity value is comparable to the electrical conductivity value of 57 S/cm measured for $Pb_7Bi_4Se_{13}$, the $^{(4,5)}L$ member of the lillianite $Pb_{N-1}Bi_2Se_{N+2}$ homologous series, which was recently studied as a potential thermoelectric material.[26] Lillianite homologues are characterized by the thickness (N1 and N2) of the two layered NaCl-type building units parallel to (001) that alternate along the *c*-axis in their crystal structure. Various lillianite homologous structures are therefore denoted $^{(N1,N2)}L$ where, N_1 and N_2 are the number of edge-sharing octahedron along the central diagonal of adjacent NaCl-type layers.[25,34] Examples of naturally occurring lillianite homologues are mineral sulfides such as lillianite, $Pb_3Bi_2S_6$ $(^{4,4}L)$,[35] heyrovskyite, $Pb_6Bi_2S_9$ $(^{7,7}L)$[36] galenobismutite, $PbBi_2S_4$ $(^{2,2}L)$,[36,37] and Cosalite $Pb_2Bi_2S_5$ $(^{2,3}L)$.[38]

Some know selenides members that were chemically synthesized and structurally characterized include $Pb_2Bi_2Se_5$ (^{3,3}L N = 3),[39] $PbBi_2Se_4$ (^{2,2}L),[40] and $Pb_3Bi_4Se_9 = Pb_{1.5}Bi_2Se_{4.5}$ (^{4,4}L N = 2.5).[40] Although a model structure was previously proposed for α- $Pb_6Bi_2Se_9$,[41] no careful crystal structure analysis has been reported to the best of our knowledge. Therefore, this work focuses on the synthesis, crystal structure determination using X-ray data on single- crystal and the thermoelectric behavior of polycrystalline single-phase powder of $Pb_6Bi_2Se_9$, a new member of the lillianite $Pb_{N-1}Bi_2Se_{N+2}$ homologous series with N1 = N2 = 7. Single crystal X-ray structure data revealed that the compound adopts the $^{(7,7)}$ L lillianite homologous structure. Differential scanning calorimetry (DSC) of polycrystalline single-phase powders of $Pb_6Bi_2Se_9$ indicates that the compounds melts congruently and crystallizes at 990°C. Thermal and electronic properties measurements show that $Pb_6Bi_2Se_9$ is a narrow band gap degenerate n-type semiconductor with low thermal conductivity (~1.1 W/m K) and a moderate figure of merit, ZT~ 0.25 at 650 K.

6.2 Results and Discussion

6.2.1 Structure

Pb$_6$Bi$_2$Se$_9$ crystallizes in the orthorhombic space group *Cmcm* (#63) with unit cell parameters: $a =$ 4.2567(9) Å, $b =$ 14.105(3) Å, $c =$ 32.412(7) Å, Z = 4 at 300 K and adopts the Heyrovskyite (Pb$_6$Bi$_2$S$_9$) structure type.[36] **Figure 6.1** shows a representation of the crystal structure of Pb$_6$Bi$_2$Se$_9$ projected along the *a*-axis. The structure can be divided into two layers, A and B, with equal thickness, $N_1 = N_2 = 7$, where N is the number of octahedrally coordinated metal positions running
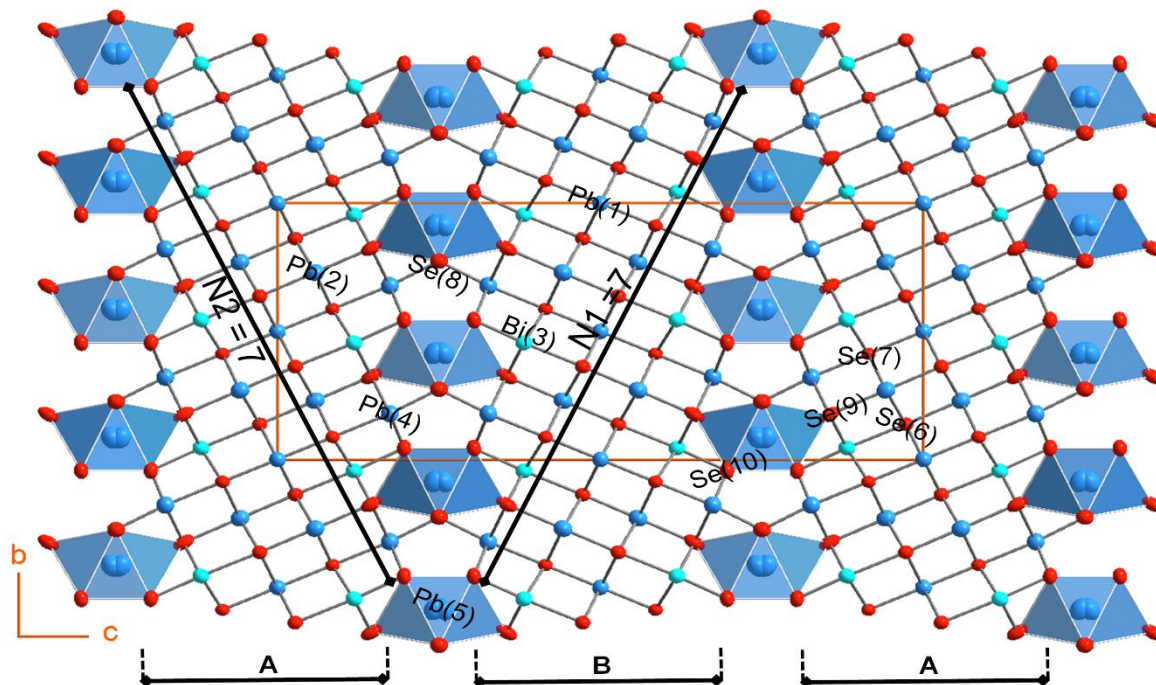
Figure 6. 1 Crystal structure of Pb$_6$Bi$_2$Se$_9$ projected along the *a*-axis highlighting the layered NaCl-type building units A and B of equal thickness (N1= N2 = 7) alternating along the *c*-axis.

across the central diagonal of individual layer, parallel to the *ab* plane and therefore can be classified as the $^{(7,7)}$L member of the Pb$_{N-1}$Bi$_2$Se$_{N+2}$ family of lillianite homologous series. Within each layer, Pb and Bi atoms occupy octahedral metal positions with various degrees of distortion

104

(**Figure 6.2**). For example, the Pb(1) site located at the center of the layer displays a Jahn Teller[46] distorted octahedral geometry [4+2] with four short equatorial Pb – Se bonds at 3.014(2) Å and two slightly elongated axial Pb – Se bonds at 3.023(3) Å. The following metal sites, Pb(2), Bi(3), and Pb(4), which are located closer to the layer borders, show more distorted octahedral coordination. For example, the octahedral coordination around Pb(2) has a [2+2+1+1] geometry with Pb – Se bond distances ranging from 3.005(2) Å to 3.130(4) Å (Table 4). A [1+2+2+1] distorted octahedral geometry with Bi – Se bond length ranging from 2.807(3) Å to 3.224(3) Å and Pb – Se bonds ranging from 2.815(3) to 3.148(3) Å was found around Bi(3) and Pb(4) sites (**Figure 6.2**). This elongated Bi – Se bond (3.224(3) Å) observed is probably a result of the stereoactivity of the Bi lone pair electrons.[23,47] The octahedrally coordinated metal atoms Pb(1),

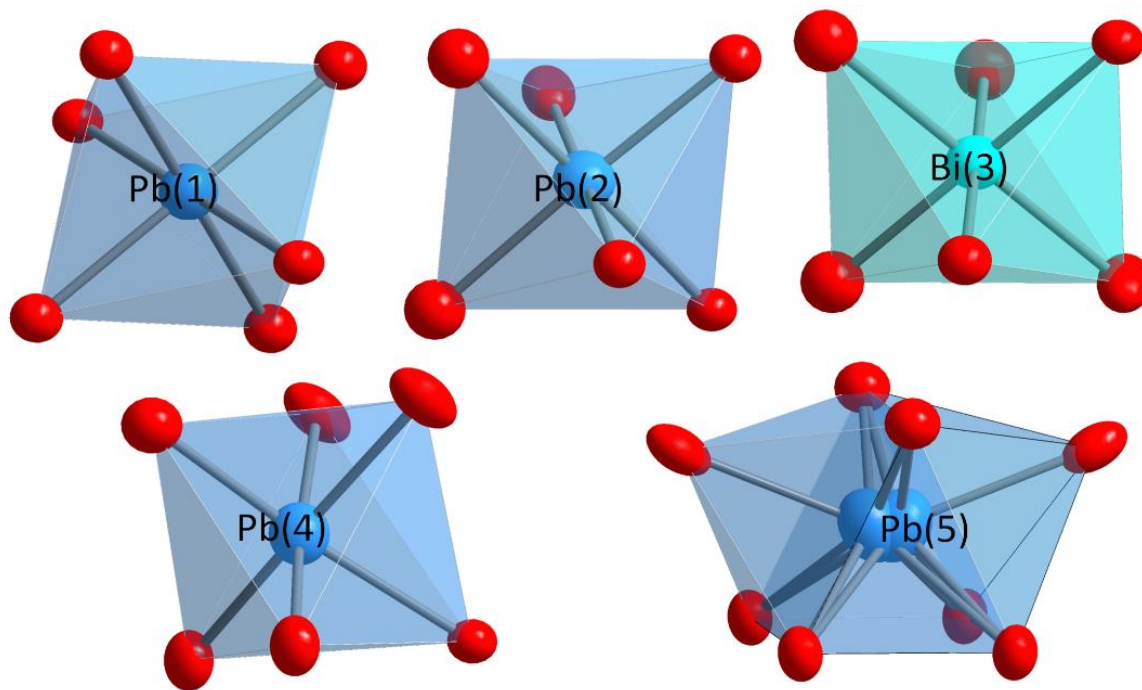**Figure 6. 2** Coordination polyhedral of Se atom around various metal atoms in the crystal structure of $Pb_6Bi_2Se_9$ showing various degrees of distortion.

Pb(2), Bi(3) and Pb(4) share edges to form a slab with orientation parallel to the (110) plane cut from the NaCl structure ($NaCl^{110}$). In the three-dimensional crystal structure of $Pb_6Bi_2Se_9$, equivalent atomic planes in adjacent NaCl-type layers A and B are stitched together along the *c*-axis by the Pb(5) atom, which is offset (z = ¼ + *w*) from the pseudomirror symmetry parallel to the *ab* plane. Attempts to refine the structure constraining Pb(5) atom at the ideal 4*c* site resulted in very poor agreement factor with the atomic displacement parameter about 10 times that of other Pb atoms. The current model, which assumes a slight off centering, *w = 0.007(2),* gives a better description of the diffraction data, although the atomic displacement parameter of Pb(5) is still about twice that other Pb atoms. This departure from the perfect *mmm* point group anticipated for orthorhombic lillianite (N1 = N2, space group: *Cmcm,* #63), where equivalent metal position is located on the mirror plane,[25,34] results in a severe distortion of the bicapped trigonal prismatic coordination (CN = 8) around Pb(5) atoms from the typical [2+2+2+2] geometry to a [2+2+1+2] geometry. The second capping Se atom lies at *3.828(7)* Å (Table 6.4), which is too far to be considered as bonding. This coordination geometry of Pb(5) atoms is reminiscent of the monocapped trigonal prismatic coordination (CN = 7) generally observed in lillianite structures with different thickness of layers A and B (N1 ≠ N2; space group *C2/m* (#12)).[34,48] Therefore, the true symmetry of the $Pb_6Bi_2Se_9$ crystal structure is at the border between orthorhombic and monoclinic symmetry. The complexity of the crystal structure of $Pb_6Bi_2Se_9$, which features pseudomirror symmetry and atomic-scale lattice incoherency between adjacent NaCl-type layers, is expected to decrease the thermal conductivity of the material by softening phonon modes.

6.2.2 Thermal Properties

In order to probe the electronic and thermal properties, polycrystalline powders of $Pb_6Bi_2Se_9$ were synthesized through solid-state reaction of the elements (lead, bismuth, and selenium) at 500°C for five days. **Figure 6.3a** shows the X-ray diffraction (XRD) pattern of the polycrystalline reaction product and the theoretical pattern calculated using single crystal structure data. The good matching of peak positions between both experimental and theoretical patterns suggests successful synthesis of the $Pb_6Bi_2Se_9$ phase. However, the mismatch in some peak intensities suggests poor crystallinity or local lattice strain of the as-synthesized material. The single-phase nature of the synthesized $Pb_6Bi_2Se_9$ polycrystalline powders was confirmed by differential scanning calorimetry (DSC). As can be observed from **Figure 6.3b**, the as-synthesized material melts congruently at 990°C and recrystallizes at 990°C upon cooling the melt to room temperature. The observed melting temperature of $Pb_6Bi_2Se_9$ is significantly larger than the ~ 560 °C melting point observed for $Pb_7Bi_4Se_{13}$,[48] which represents the $^{(4,5)}L$ member of the $Pb_{N-1}Bi_2Se_{N+2}$ homologous series. From a chemical composition viewpoint, the molecular formula of $Pb_6Bi_2Se_9$ can be written as $6(PbSe)\cdot(Bi_2Se_3)$, which denotes an atomic scale integration of two interesting thermoelectric materials. Therefore, the large difference in the melting temperature of $Pb_6Bi_2Se_9$ and $Pb_7Bi_4Se_{13}$, phases can be attributed to the large $PbSe/Bi_2Se_3$ ratio of 6/1 in $Pb_6Bi_2Se_9$ compared to 7/2 in $Pb_7Bi_4Se_{13}$.

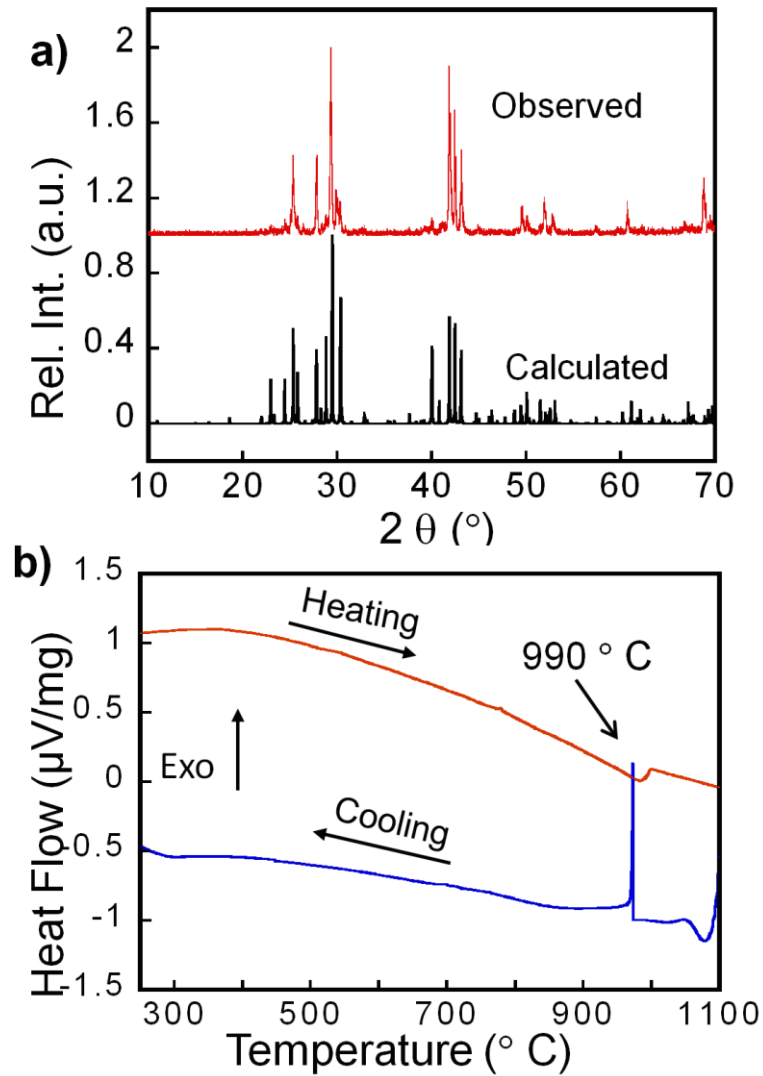**Figure 6. 3 a**) X-ray powder diffraction pattern of the synthesized polycrystalline powder of $Pb_6Bi_2Se_9$ compared with the theoretical pattern calculated using single crystal structure data. **b**) Differential scanning calorimetry (DSC) curves of the synthesized $Pb_6Bi_2Se_9$ powder showing congruent melting and recrystallization at 990°C upon heating and cooling.

6.2.3 Electronic Transport Properties

To probe the thermoelectric behavior of the synthesized materials, electrical conductivity, thermopower, thermal conductivity, and Hall effect data were collected in the temperature range from 300 K to 675 K using a hot pressed pellet of the synthesized material. The sample shows negative values of the thermopower in the whole measured temperature range indicating that that electrons are the majority charge carriers in $Pb_6Bi_2Se_9$ (n-type semiconductor) (**Figure 6.4a**). This is consistent with the negative thermopower observed for $Pb_7Bi_4Se_{13}$.[48] At 300 K, the thermopower of $Pb_6Bi_2Se_9$ is -53 $\mu V\ K^{-1}$ and increases in magnitude with rising temperature to a value of -193 $\mu V\ K^{-1}$ at 673K (**Figure 6.4a**). These values are significantly lower than the thermopower of -160 $\mu V\ K^{-1}$ and $-243\ \mu V\ K^{-1}$ measured for $Pb_7Bi_4Se_{13}$ at 300 K and 600 K, respectively. The nearly linear temperature dependence of the thermopower suggests that $Pb_6Bi_2Se_9$ is a degenerate n-type semiconductor, where extrinsic carriers dominate electronic transport in the temperature range studied. Within the temperature range from 300K to 650K, the carrier concentration is nearly constant as the onset of the thermal excitation of intrinsic carriers from the valence band into the conduction band appears at temperatures above 650K (**Figure 6.4a**). The electrical conductivity of $Pb_6Bi_2Se_9$ is 350 S/cm at 300K and gradually decreases with increasing temperature reaching a value of 100 S/cm at 675K (**Figure 6.4b**). Impurity-carrier scattering is considered to be negligible

compared to phonon-carrier scattering in this temperature regime. The drop in the electrical

conductivity can also be attributed to carrier scattering at the incoherent interfaces between the

NaCl-type layers and local strain from distorted bond lengths. This metallic-like behavior of the electrical conductivity indicates that $Pb_6Bi_2Se_9$ is a heavily doped n-type degenerate semiconductor.

Figure 6.5a shows the temperature dependence of the carrier concentration of $Pb_6Bi_2Se_9$. At 293K, the electron concentration is $67.83 \times 10^{19} cm^{-3}$ at 293K and fluctuates between a local maximum of $75.45 \times 10^{19} cm^{-3}$ at 650K and a minimum of $63.199 \times 10^{19} cm^{-3}$ at 323K. In this range, the carrier concentration fluctuates, but is nearly constant and indicates this range of temperature is below the threshold

Figure 6. 4 Temperature dependence of the electronic transport in hot-press pellet of the synthesized $Pb_6Bi_2Se_9$ showing n-type semiconducting behavior. **a**) Seebeck coefficient; **b**) Electrical conductivity

for thermal excitation into higher energy states. This is further supported by the electrical

conductivity and thermopower measurements (**Figure 6.4a** & **6.4b**), which follow a linear trend

across the temperature range of 300K – 650K. Above 650K, the carrier concentration drastically

increases in an exponential fashion. At 673K, the carrier concentration is $79.78 \times 10^{19} cm^{-3}$ and

increases to $152.04 \times 10^{19} cm^{-3}$ at 773K. This large increase is likely the result of thermal excitation

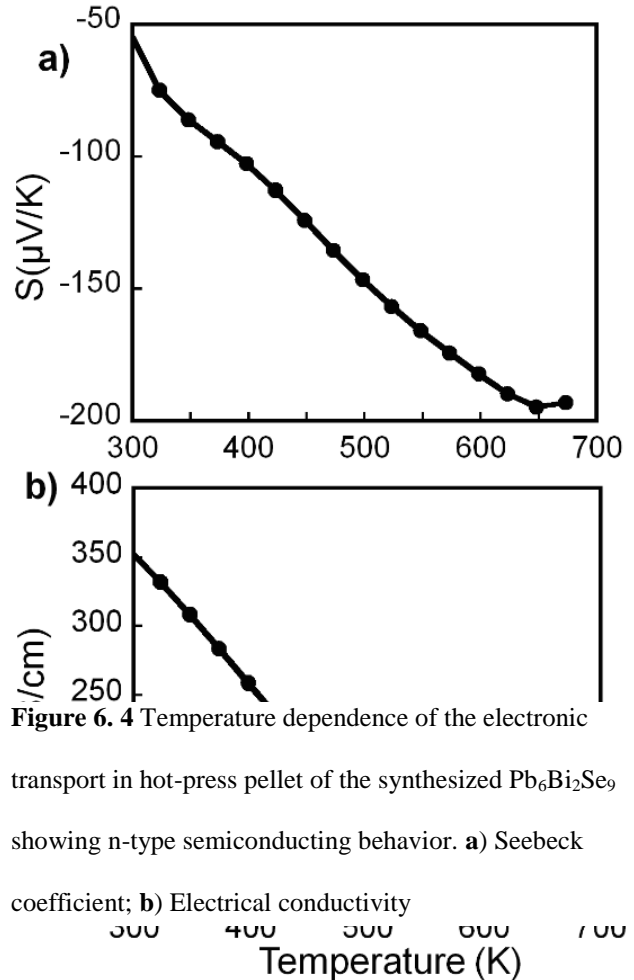of intrinsic carriers across the band gap.

Figure 6.5b shows the temperature dependence of the carrier mobility. The carrier mobility ($\mu = \sigma/ne$) was extracted using the carrier density and conductivity data. At 293K, the electron mobility is 3.291cm^{2}V^{-1}s^{-1} and decreases monotonically with increase temperature to 0.246cm^{2}V^{-1}s^{-1}. This is consistent with the increase in phonon concentration with increasing temperature. As phonon concentration increases with increasing temperature, phonon scattering increases leading to the reduction in carrier mobility. The carrier mobility is unusually low for an n-type narrow band gap material, suggesting that the band edges are mismatched and have a high degree of degeneracy. Theoretical calculations elucidate the nature of the band structure and

Figure 6. 5 Temperature dependence of the **a**) carrier concentration and **b**) carrier mobility of Pb$_6$Bi$_2$Se$_9$ hot-press pellet.

shed light on the low carrier mobility. The mobility curve, which decreases with increasing temperature, can be fit to the power law T^{-3}, which suggests the dominance of the electron-optical phonon coupling behavior. This corroborates with the thermal conductivity data presented in **Figure 6.6a**. The lattice thermal conductivity is greater than the electronic contribution due to the electron-phonon scattering. This results in the suppression of the electronic component and allows the lattice contribution to overtake the electronic contribution to thermal conductivity.
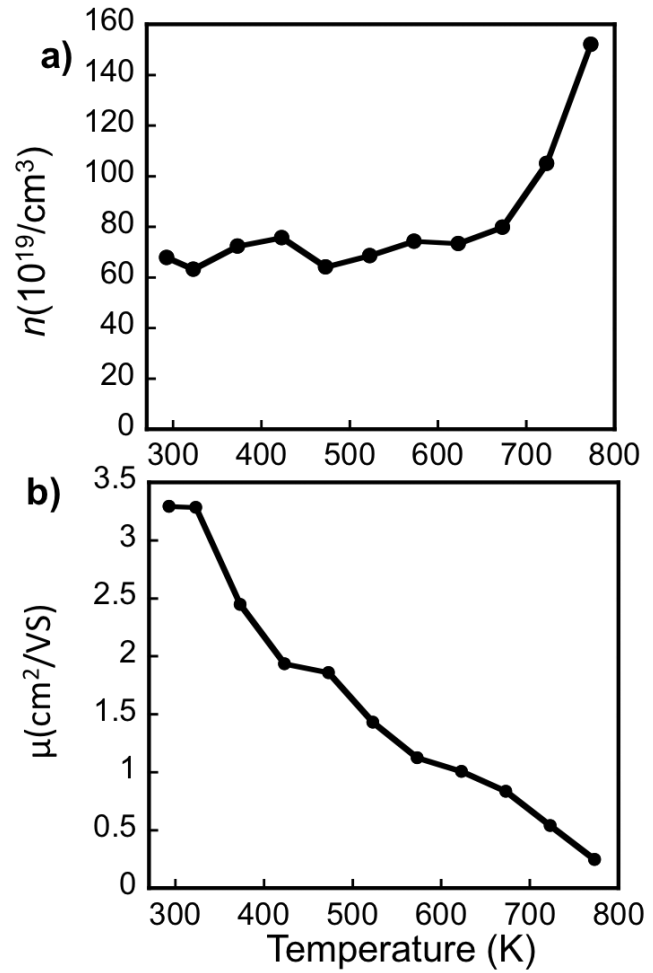
Nanostructuring will enable the tailoring of phonon and electron scattering surfaces, which should increase the ZT of $Pb_6Bi_2Se_9$.

Figure 6.6a shows the temperature dependence of the thermal conductivity of $Pb_6Bi_2Se_9$. At 300K the total thermal conductivity of $Pb_6Bi_2Se_9$ is 1.12 W/m K and remains relatively constant upon increasing the temperature to 673 K. The lattice contribution to the total thermal conductivity was estimated by subtracting the electronic contribution (κ_{el}) calculated using the Wiedemann-Franz law, $\kappa_{el} = L\sigma T$, where $L = 2.45 \times 10^{-8}$ W Ω K^{-2} is the assumed Lorenz number. As shown in **Figure 6.5a**, the lattice contribution to the thermal conductivity (κ_{ph}) ranged from 0.87 W/mK at 300 K to 0.94 W/mK at 673 K, whereas the electronic contribution to the thermal conductivity (κ_{el}) decreases from 0.26 W/m K at 300K to 0.18 W/m K at 673K. This indicates that the lattice contribution dominates thermal transport in $Pb_6Bi_2Se_9$.

Figure 6. 6 Temperature dependence of the **a**) thermal conductivity and **b**) figure of merit, ZT of $Pb_6Bi_2Se_9$ hot-press pellet.

Therefore, the total thermal conductivity in $Pb_6Bi_2Se_9$ could be significantly reduced through nanostructuring and/or solid solution alloying, which should improve the thermoelectric performance.
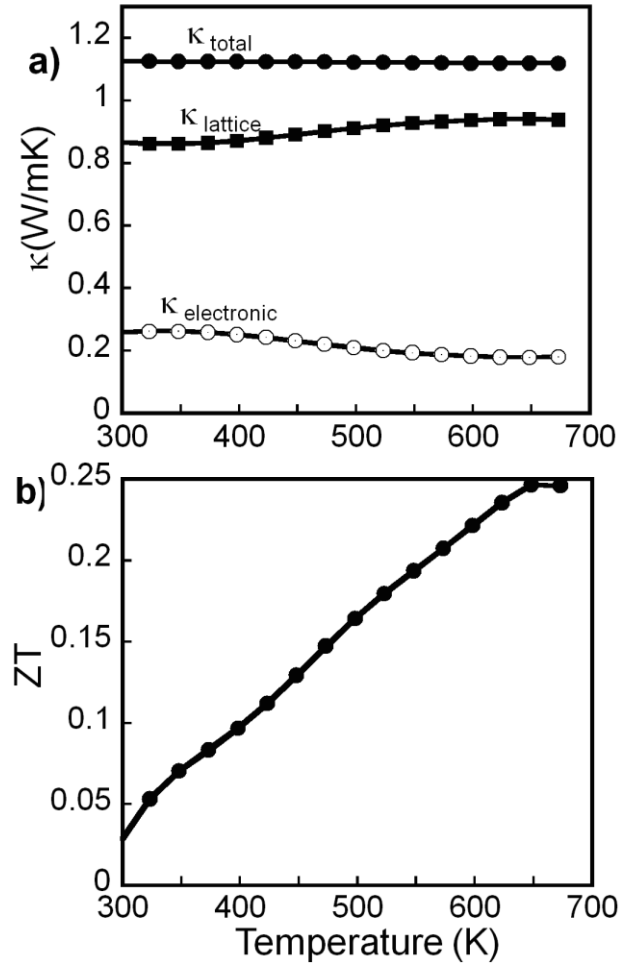
The observed total thermal conductivity of $Pb_6Bi_2Se_9$ (1.12 W/m K at 300K) is approximately four times the thermal conductivity of $Pb_7Bi_4Se_{13}$.[48] This large difference in the total thermal conductivity of $Pb_6Bi_2Se_9$ and $Pb_7Bi_4Se_{13}$ can be partly attributed to the difference in their electrical conductivity. However, since the lattice thermal conductivity dominates thermal transport in both compounds, we believe that the large difference in the total thermal conductivity mainly originates from the difference in the atomic structure. While the structure of both compounds contains two alternating NaCl-type layers (A and B), the thickness of the layers as well as their relative orientation in the crystal structure are sharply different. In the structure of $Pb_7Bi_4Se_{13}$, the NaCl-type layers (A and B) are of different thicknesses (N1 = 5, N2 = 4) and are weakly stitched together by isolated chains of face-sharing monocapped trigonal prism around Pb atoms. The difference in the thickness of adjacent layers A and B results in a severe misalignment of atomic lattice planes at their interfaces, which significantly reduces the propagation of thermal phonon along the c-axis. However, the NaCl-type layers A and B in the structure of $Pb_6Bi_2Se_9$ are of equal size (N1 = N2 = 7) and are thicker than the layers found in the structure of $Pb_7Bi_4Se_{13}$ (N1 = 5, N2 = 4).[48] This results in a more symmetrical arrangement of layers A and B with a pseudomirror plane at their interfaces. In addition, the linear density (along the c-axis) of interfaces (A/B) between adjacent layers is significantly lower in $Pb_6Bi_2Se_9$ compared to $Pb_7Bi_4Se_{13}$ given the thicker A and B layers. Therefore, a weaker phonon scattering in $Pb_6Bi_2Se_9$ compared to $Pb_7Bi_4Se_{13}$ can be anticipated due to the combination of higher degree of coherency between the layers and lower linear density of A/B interfaces, which implies longer phonon mean free path in $Pb_6Bi_2Se_9$.

Figure 6.6b shows the temperature dependence of the figure of merit, ZT, of $Pb_6Bi_2Se_9$. At 300 K, the ZT value is 0.03 and rapidly increases with temperature to a maximum of 0.25 at

650K. The observed sharp increase in the ZT values with temperature results from the strong temperature dependence of thermopower. Given, the large lattice thermal conductivity of $Pb_6Bi_2Se_9$ at high temperature, we anticipate further improvements in the ZT values of $Pb_6Bi_2Se_9$ through additional reduction of the thermal conductivity by applying the concepts of solid solutions alloying and nanostructuring.

6.3 Conclusion

In summary, the crystal structure of $Pb_6Bi_2Se_9$, the $(^{7,7}L)$ member of the lillianite homologous series $Pb_{N-1}Bi_2Se_{N+2}$ (N = 7) was elucidated using single-crystal X-ray diffraction data and its thermoelectric behavior was investigated using hot pressed pellets of polycrystalline powders synthesized via solid-state reaction of the elements. It was found that the as-synthesized material is a heavily doped n-type semiconductor with a moderate electrical conductivity (110 S cm^{-1}) and a large thermopower value (-200 μV/K) at 673K. However, the compound exhibits a slightly large thermal conductivity (1.12 W/m K) at high temperature, which results to a marginal ZT value of 0.25 at 650K. The large thermal conductivity of $Pb_6Bi_2Se_9$ when compared to the $Pb_7Bi_4Se_{13}$ (N1 = 5, N2 = 4)[48] homologue is attributed to the combination of higher degree of coherency between the layers (A and B) and the lower linear density of A/B interfaces (along the c-axis), which results in weaker phonon scattering in $Pb_6Bi_2Se_9$ compared to $Pb_7Bi_4Se_{13}$. However, the large lattice contribution to the total thermal conductivity of $Pb_6Bi_2Se_9$ suggests that significant reduction in the total thermal conductivity can be achieved through nanostructuring and/or solid-solution alloys. This should result in further improvement of the thermoelectric figure of merit of $Pb_6Bi_2Se_9$.

Tables

Table 6. 1 Bond valence sum (BVS) calculations for $Pb_6Bi_2Se_9$ at 300K

Atomic position	BVS	Atom type	Oxidation state
Pb1	2.25	Pb	2+
Pb2	2.14	Pb	2+
Bi3	3.01	Bi	3+
Pb4	2.30	Pb	2+
Pb5	1.90	Pb	2+

Table 6. 2 Selected crystallographic data for $Pb_6Bi_2Se_9$ at 300K

Crystal syst. space group	Orthorhombic, C*mcm* (#63)
Formula weight (g/mol)	2371.74
Calculated density (g/cm^3)	8.10
Lattice parameters (Å)	
$a =$	4.257(2)
$b =$	14.105(3)
$c =$	32.412(7)
V(Å^3); Z	1946.04(7); 4
Radiation (Å)	λ (MoKα) = 0.71073
μ (cm^{-1})	865
2θ range	$6° \leq 2\theta \leq 54°$
index range	$-5 \leq h \leq 5$
	$-18 \leq k \leq 18$
	$-39 \leq l \leq 39$
Transmission factors	0.05 - 0.17
Diff. elec. density [eÅ^{-3}]	+2.44 to −2.86
R_1 (F$_o$>4σ(F$_o$))[a]	0.041

wR_2 (all) [b]	0.092
GOF	1.210

[a] $R_1 = \Sigma||F_o|-|F_c||/\Sigma|F_o|$; [b] $wR_2 = [\Sigma w(F_o^2-F_c^2)^2/\Sigma w(F_o^2)^2]^{1/2}$

Table 6. 3 Wyckoff Positions (W.P.), Atomic Coordinates, equivalent isotropic thermal displacement parameters ($U_{eq}/10^{-4} \times Å^2$) for all atoms in the asymmetric unit of $Pb_6Bi_2Se_9$ at 300K

Atom	W.P.	x	y	z	U_{eq}
Pb1	4b	0	0.5	0.5	242(4)
Pb2	8f	1/2	0.2703(2)	0.5582(4)	286(4)
Bi3	8f	1/2	0.4552(2)	0.3815(3)	232(4)
Pb4	8f	0	0.6787(2)	0.3262(4)	275(4)
Pb5	4c	0	0.4149(2)	¼ + w	421(5)
Se6	8f	1/2	0.3626(2)	0.4725(2)	191(6)
Se7	8f	0	0.5873(2)	0.4148(2)	169(6)
Se8	4c	0	0.7743(3)	¼	260(6)
Se9	8f	1/2	0.1752(2)	0.6454(2)	268(7)
Se10	8f	1/2	0.5439(2)	0.3040(2)	228(7)

U_{eq} is defined as one-third of the trace of the orthogonalized U_{ij} tensor
w = 0.007(2)

Table 6. 4 Selected inter-atomic distances (Å) in $Pb_6Bi_2Se_9$ at 300K

Bond type	Distance [Å]	Bond type	Distance [Å]
Pb1—Se6, 6[i, ii, iii]	3.014(2)	Pb4—Se8	2.815(3)
Pb1—Se7, 7[iii]	3.023(3)	Pb4—Se10, 10[i]	2.942(2)
		Pb4—Se9[ii, iii]	3.102(2)
Pb2—Se6[iv, v]	3.005(2)	Pb4—Se7	3.148(3)
Pb2—Se7[ii, iii]	3.054(2)		
Pb2—Se6	3.066(3)	Pb5—Se8[viii, ix]	2.918(4)
Pb2—Se9	3.130(4)	Pb5—Se10, 10[i]	3.191(4)
		Pb5—Se9[iv]	3.415(7)
Bi3—Se10	2.807(3)	Pb5—Se10[vii, x]	3.425(4)
Bi3—Se9[iv, v]	2.945(2)	*Pb5----Se9*	*3.828(7)*
Bi3—Se7, 7[vi]	3.028(2)		
Bi3—Se6	3.224(3)		

[a] Operators for generating equivalent atoms: (i) −1+x, y, z; (ii) 1−x, 1−y, 1−z; (iii) −x, 1−y, 1−z; (iv) ½−x, ½−y, 1−z; (v) 3/2−x, ½−y, 1−z; (vi) 1+x, y, z; (vii) x, y, ½−z; (viii) −½+x, −½+y, z; (ix) ½+x, −½+y, z; (x) −1+x, y, ½−z; (xi) ½+x, ½+y, z; (xii) ½+x, ½+y, ½−z; (xiii) −½+x, ½+y, z; (xiv) −½+x, ½+y, ½−z; (xv) −x, 1−y, −½+z; (xvi) ½−x, ½−y, ½+z; (xvii) 1+x, y, ½−z

6.4 References

(1)   Mrotzek, A.; Iordanidis, L.; Kanatzidis, M. G. *Inorganic chemistry* **2001**, *40*, 6204.
(2)   Mrotzek, A.; Chung, D. Y.; Ghelani, N.; Hogan, T.; Kanatzidis, M. G. *Chemistry–A European Journal* **2001**, *7*, 1915.
(3)   Ohta, H.; Seo, W. S.; Koumoto, K. *Journal of the American Ceramic Society* **1996**, *79*, 2193.
(4)   Ruck, M.; Poudeu, P. F. P. *Zeitschrift Fur Anorganische Und Allgemeine Chemie* **2008**, *634*, 482.
(5)   Ruck, M.; Poudeu, P. F. P. *Zeitschrift Fur Anorganische Und Allgemeine Chemie* **2008**, *634*, 475.
(6)   Zheng, J.-c. *Frontiers of Physics in China* **2008**, *3*, 269.
(7)   Gascoin, F.; Ottensmann, S.; Stark, D.; Haïle, S. M.; Snyder, G. J. *Advanced Functional Materials* **2005**, *15*, 1860.
(8)   Hazan, E.; Madar, N.; Parag, M.; Casian, V.; Ben-Yehuda, O.; Gelbstein, Y. *Advanced Electronic Materials* **2015**, *1*.
(9)   Hedegaard, E. M. J.; Johnsen, S.; Bjerg, L.; Borup, K. A.; Iversen, B. B. *Chem Mater* **2014**, *26*, 4992.
(10)   Liu, Y.; Zhao, L. D.; Zhu, Y.; Liu, Y.; Li, F.; Yu, M.; Liu, D.-B.; Xu, W.; Lin, Y.-H.; Nan, C.-W. *Advanced Energy Materials* **2016**, *6*.
(11)   Yang, H.; Bahk, J.-H.; Day, T.; Mohammed, A. M.; Min, B.; Snyder, G. J.; Shakouri, A.; Wu, Y. *Nano letters* **2014**, *14*, 5398.
(12)   Biswas, K.; He, J. Q.; Blum, I. D.; Chun-Iwu; Hogan, T. P.; Seidman, D. N.; Dravid, V. P.; Kanatzidis, M. G. *Nature* **2012**, *490*.
(13)   Liu, Y. F.; Sahoo, P.; Makongo, J. P. A.; Zhou, X. Y.; Kim, S. J.; Chi, H.; Uher, C.; Pan, X. Q.; Poudeu, P. F. P. *J Am Chem Soc* **2013**, *135*, 7486.
(14)   Makongo, J. P. A.; Misra, D. K.; Salvador, J. R.; Takas, N. J.; Wang, G. Y.; Shabetai, M. R.; Pant, A.; Paudel, P.; Uher, C.; Stokes, K. L.; Poudeu, P. F. P. *J Solid State Chem* **2011**, *184*, 2948.
(15)   Makongo, J. P. A.; Misra, D. K.; Zhou, X. Y.; Pant, A.; Shabetai, M. R.; Su, X. L.; Uher, C.; Stokes, K. L.; Poudeu, P. F. P. *J Am Chem Soc* **2011**, *133*, 18843.
(16)   Poudeu, P. F. P.; D'Angelo, J.; Downey, A. D.; Short, J. L.; Hogan, T. P.; Kanatzidis, M. G. *Angew Chem Int Edit* **2006**, *45*, 3835.
(17)   Poudeu, P. F. P.; D'Angelo, J.; Kong, H. J.; Downey, A.; Short, J. L.; Pcionek, R.; Hogan, T. P.; Uher, C.; Kanatzidis, M. G. *J Am Chem Soc* **2006**, *128*, 14347.
(18)   Snyder, G. J.; Toberer, E. S. *Nat Mater* **2008**, *7*, 105.
(19)   Liu, H. L.; Shi, X.; Xu, F. F.; Zhang, L. L.; Zhang, W. Q.; Chen, L. D.; Li, Q.; Uher, C.; Day, T.; Snyder, G. J. *Nat Mater* **2012**, *11*, 422.
(20)   Sales, B. C.; Mandrus, D.; Williams, R. K. *Science* **1996**, *272*, 1325.

(21)   Uher, C. *Semiconduct Semimet* **2001**, *69*, 139.
(22)   Kanatzidis, M. G. *Accounts of Chemical Research* **2005**, *38*, 359.
(23)   Mrotzek, A.; Kanatzidis, M. G. *Accounts of chemical research* **2003**, *36*, 111.
(24)   Makovicky, B.; Mumme, W. C.; Watts, J. A. *Can Mineral* **1977**, *15*, 339.
(25)   Pring, A.; Jercher, M.; Makovicky, E. *Mineralogical Magazine* **1999**, *63*, 917.
(26)   Olvera, A.; Shi, G.; Djieutedjeu, H.; Page, A.; Uher, C.; Kioupakis, E.; Poudeu, P. F. *Inorganic chemistry* **2014**, *54*, 746.
(27)   Chatterjee, A.; Guin, S. N.; Biswas, K. *Phys Chem Chem Phys* **2014**, *16*, 14635.
(28)   Shelimova, L.; Karpinskii, O.; Konstantinov, P.; Avilov, E.; Kretova, M.; Lubman, G.; Nikhezina, I. Y.; Zemskov, V. *Inorganic Materials* **2010**, *46*, 120.
(29)   Shelimova, L.; Karpinskii, O.; Zemskov, V. *Inorganic Materials* **2008**, *44*, 927.
(30)   Shelimova, L.; Zemskov, V.; Avilov, E.; Kretova, M.; Nikhezina, I. Y.; Mikhailova, A. *Inorganic Materials: Applied Research* **2015**, *6*, 298.
(31)   Zemskov, V.; Shelimova, L.; Konstantinov, P.; Avilov, E.; Kretova, M.; Nikhezina, I. *Inorganic Materials: Applied Research* **2011**, *2*, 405.
(32)   Zhang, Y.; Wilkinson, A. P.; Lee, P. L.; Shastri, S. D.; Shu, D.; Chung, D.-Y.; Kanatzidis, M. G. *Journal of applied crystallography* **2005**, *38*, 433.
(33)   Ohta, M.; Chung, D. Y.; Kunii, M.; Kanatzidis, M. G. *J Mater Chem A* **2014**, *2*, 20048.
(34)   Topa, D.; Makovicky, E.; Schimper, H. J.; Dittrich, H. *The Canadian Mineralogist* **2010**, *48*, 1127.
(35)   Takagi, J.; Takeuchi, Y. *Acta Cryst.* **1972**, *B28*, 649
(36)   Takeuchi, Y.; Takagi, J. *P Jpn Acad* **1974**, *50*, 76.
(37)   Iitaka, Y.; Nowacki, W. *Acta Crystallogr* **1962**, *15*, 691.
(38)   Srikrishnan, T.; Nowacki, W. *Zeitschrift für Kristallographie* **1974**, *140*, 114
(39)   Agaev, K. A.; Talybov, A. G.; Semileto.Sa *Kristallografiya* **1966**, *11*, 736.
(40)   Agaev, K. A.; Semileto.Sa *Sov Phys Crystallogr* **1968**, *13*, 201.
(41)   Chung, D.-Y.; Lane, M. A.; Ireland, J. R.; Brazis, P. W.; Kannewurf, C. R.; Kanatzidis, M. G. *Materials Research Society Symposium* **2000**, *626*, Z7.4.1.
(42)   Misra, D. K.; Makongo, J. P. A.; Sahoo, P.; Shabetai, M. R.; Paudel, P.; Stokes, K. L.; Poudeu, P. F. P. *Sci Adv Mater* **2011**, *3*, 607.
(43)   Sheldrick, G.; SHELXTL, D. *Inc., Madison, WI, USA* **2000**.
(44)   Brese, N.; O'keeffe, M. *Acta Crystallographica Section B: Structural Science* 1991, 47, 192.
(45)   Brandenburg, K.; Putz, H. Crystal Impact GbR, Bonn, Germany 2005.
(46)   Köppel, H.; Yarkony, D. R.; Barentzen, H. The Jahn-Teller Effect: Fundamentals and Implications for Physics and Chemistry; Springer Science & Business Media, 2009; Vol. 97.
(47)   Fisher, G. A.; Norman, N. C. Advances in Inorganic Chemistry 1994, 41, 233.
(48)   Olvera, A.; Shi, G.; Djieutedjeu, H.; Page, A.; Uher, C.; Kioupakis, E.; Poudeu, P. F. Inorganic Chemistry 2015, 54, 746.

Chapter 7

General Conclusions and Future works

7.1 General Conclusions

$FeBi_2Se_4$ is a new High Tc Ferromagnet exhibiting n-type semiconducting behavior crystallizing in the monoclinic C2/m space group.The discovery of n-type ferromagnetic semiconductors (n-FMSs) exhibiting high electrical conductivity and Curie temperature (T_c) above 300 K would dramatically improve semiconductor spintronics and pave the way for the fabrication of spin-based semiconducting devices. However, the realization of high-T_c n-FMSs and p-FMSs in conventional high-symmetry semiconductors has proven extremely difficult due to the strongly coupled and interacting magnetic and semiconducting sublattices. We show that decoupling both functional sublattices in the low-symmetry semiconductor $FeBi_2Se_4$ enables unprecedented coexistence of high n-type electrical conduction and ferromagnetism with T_c~450 K. The structure of $FeBi_2Se_4$ consists of well-ordered magnetic sublattices built of $[Fe_nSe_{4n+2}]_\infty$ single-chain edge-sharing octahedra, coherently embedded within the three-dimensional Bi-rich semiconducting framework. Magnetotransport data reveal a negative magnetoresistance, indicating spin-polarization of itinerant conducting electrons. These findings demonstrate that decoupling magnetic and semiconducting sublattices allows access to high-T_c n-FMSs and p-FMSs as well as helps unveil the mechanism of carrier-mediated ferromagnetism in spintronic materials.

Using the $FeBi_2Se_4$ crystal as a template to understand the origin of the High Tc in this crystal by modifying the Fe distribution in the crystal. This was done without significantly altering the carrier concentration. Here, we report on the effect of partial substitution of Fe by Sn on the distribution of magnetic centers within the $Fe_{1-x}Sn_xBi_2Se_4$ crystal lattice and its impact of the electronic and magnetic properties. High temperature direct current (DC) magnetic susceptibility measurements reveal that all $Fe_{1-x}Sn_xBi_2Se_4$ samples remain ferromagnetic over a wide temperature range and the Curie transition temperature, T_c, decreases from ~ 450 K for compositions with $x \leq 0.15$ to 325 K for compositions with high Sn content. The observed drop in T_c is ascribed to an increased separation between the magnetic centers for compositions with $x > 0.15$. Hall effect measurements confirm the *n*-type semiconducting nature of all compounds. Interestingly, the carrier density of $Fe_{1-x}Sn_xBi_2Se_4$ samples gradually decreases with decreasing temperature down to 150 K below which a remarkable transition from semiconducting to metallic behavior is observed for compositions with $x \geq 0.25$.

Going further to understand degree of correlation in the $FeBi_2Se_4$ crystal, we create a solid solution between the p-type analogue, $FeSb_2Se_4$, and the n-type analogue, $FeBi_2Se_4$ in order to modify the carrier concentration without changing the Fe concentration in order to determine the effect itinerant carriers have on the magnetic phase present. This detailed study shows that the Tc is more dependent on the Fe distribution of the material rather than the itinerant carrier concentration, but unveils the dependence of measurable moment on carrier concentration. Seebeck measurements show a cross over from p-type to n-type conduction with increasing Bi content. The effect of carrier concentration is most evident in the saturation magnetization which observes a significant suppression with increasing carrier concentration.

$Pb_6Bi_2Se_9$ is a selenium analogue of heyrovsite crystallizing in the orthorhombic space group Cmcm at 300K. We have shown that this material system has a unique structure consisting of two NaCl-type layers, A and B. These layers have a similar thickness and share $(Pb/Bi)Se_6$ octahedra along the central diagonal. Electronic transport measurements indicate that the compound is a narrow band n-type semiconductor with thermpower of $53\mu V/K$ at room temperature. Due to the compounds low crystal symmetry, $Pb_6Bi_2Se_9$ exhibits moderately low temperature independent thermal conductivity ~1.1 W/mK as a result of strong phonon scattering along the shared $(Pb/Bi)Se_6$ diagonal. The ZT is 0.25 at 673, and can be further enhanced with selective thermoelectric doping and enhancement.

7.2 Future works

This work on ternary ferromagnetic semiconductors and thermoelectric materials has contributed significant insight into the fundamental mechanisms underlying the electronic, thermal, and magnetic properties of novel chalcogenides.

The natural progression for the ferromagnetic semiconductors is to conduct neutron diffraction studies in an effort to understand the magnetic lattice present within these interesting phases. This will enable a quantitative understanding of Fe distributions and their effect on the magnetic phases present. X-ray Magnetic Circular Dichroism experiments will also be imperative in order to understand the atomic contributions of Fe and other transition metals in the resulting magnetic phases. The combination of these experiments will enable significant